Kinetic Simulations of Dusty Plasmas

I n a u g u r a l d i s s e r t a t i o n

zur

Erlangung des akademischen Grades

doctor rerum naturalium (Dr. rer. nat.)

an der Mathematisch-Naturwissenschaftlichen Fakultät

der

Ernst-Moritz-Arndt-Universität Greifswald

vorgelegt von

Venkata Ramana Ikkurthi

geboren am **01.08.1976**

in **Chilakaluripet, Indien**

Greifswald, October 2009

Dekan: **Prof. Dr. Klaus Fesser**

....

1. Gutachter : **Prof. Dr. André Melzer**

....

2. Gutachter: **Dr. David Tskhakaya**

....

Tag der Promotion: **14 - 12 - 2009**

....

To

Lillu & Chikki

Der Weg ist das Ziel
(The path is the destination /the destination is not
important, but the path that leads there)

न चोरहार्यं, न च राजहार्यं, न भ्रातृभाज्यं न च भारकारि |
व्यये कृते वर्धत एव नित्यम विद्याधनं सर्वधनप्रधानं ||

(Knowledge cannot be stolen by thieves,
It cannot be forcibly snatched by kings,
It cannot be devided among brothers,
It does not cause a load on shoulders,
If spent or shared, it indeed always keeps on growing.
The wealth of knowledge... is the most superior wealth of all!)

Abstract

This thesis constitutes a computational study of charge and ion drag force on micron-sized dust particles immersed in rf discharges. Knowledge of dust parameters like dust charge, floating potential, shielding and ion drag force is very crucial for explaining complex laboratory dusty plasma phenomena, such as void formation in microgravity experiments and wakefield formation in the sheaths. Existing theoretical models assume standard distribution functions for plasma species and are applicable over a limited range of flow velocities and collisionality. Kinetic simulations are suitable tools for studying dust charging and drag force computation. The main aim of this thesis is to perform three dimensional simulations using a Particle-Particle-Particle-Mesh (P^3M) model to understand how the dust parameters vary for different positions of dust in rf discharges and how these parameters on a dust evolve in the presence of neighboring dust particles.

At first, rf discharges in argon have been modelled using a three-dimensional PIC-MCC code for the discharge conditions relevant to the dusty plasma experiments. All necessary elastic and inelastic collisions have been considered. The plasma background is found collisional, charge-exchange collisions between ions and neutrals being dominant. Electron and ion distributions are non-Maxwellian. The dominant heating mechanism is Ohmic.

Then, simulations have been done to compute the dust parameters for various sizes of dust located at different positions in the rf discharges. Dust charge and floating potential in the presheath are slightly larger than the values in the bulk due to the higher electron flux to the dust particle in the presheath. From presheath to the sheath the charge and floating potential values decrease due to the decrease of the electron current to the dust. A linear dependence of dust potential on dust size has been found, which results in a nonlinear dependence of the dust charge with the dust size when the particle is assumed to be a spherical capacitor. This has been verified by independently counting the charges collected by the dust. The computed dust parameters are also

compared with theoretical models. Simulated dust floating potentials are comparable
to values obtained from Allen-Boyd-Reynolds (ABR) [1] and Khrapak [2] models, but
much smaller than the values obtained from Orbit Motion Limited (OML) [3] model.
The dust potential distribution behaves Debye-Hückel-like. The shielding lengths are
in between ion and electron Debye lengths. Further, the orbital drag force is typically
larger than the collection drag force. The total drag force for the collisional case is
larger than for the collisionless case and it scales nonlinearly with the dust size. The
collection drag values and size-scaling agrees with Zobnin's model [4].

The charging and drag force computation is then extended to two and multiple
static dust particles in the rf discharge to study the influence of neighboring dust
particles on the dust parameters. Initially, the dust parameters on two dust particles
are computed for various interparticle separation distances and for dust particles placed
at different locations in the rf discharge. It is observed that for dust separations larger
than the shielding length the dust parameters for the two dust particles match with
the single dust particle values. As the dust separation is equal to or less than the
shielding length the ion drag force increases due to the buildup of a parallel drag
force component. However, the main dust properties like charge, potential, vertical
component of ion drag are not affected considerably. This is attributed to the smaller
collection impact parameter values compared to the dust separation.

Then the dust charges on multiple dust particles located at different positions in
the discharge and arranged along the discharge axis are also computed. It is found that
the charges of the multiple dust particles in the bulk or presheath do not differ much
from the single particle values at that location. But the dust charges of multiple dust
particles located in the sheath drastically differ from the single dust parameter values.
Due to ion focusing from dust particles in the upper layers, the ion current increases
to dust particles in the lower layers resulting in smaller charge values. This is as well
the case where dust particles are vertically aligned as in the standard experiments of
dusty plasmas.

In conclusion, this work used a fully kinetic (PIC and MD or P^3M) model to study
the physics of dust charging in rf plasmas. Our simulations revealed that the dust
parameters vary considerably from the bulk to the sheath. The CX collisions increase
flux to the dust thereby affecting the dust parameters and their scaling with dust
size. Also, a dust particle affects the charging dynamics of its neighbor only when their
separation is within the shielding length. In the plasma sheath, ion focussing can cause
great reduction in dust charges.

Table of Contents

Appendices

List of Figures

List of Tables

Chapter 1

Introduction

Plasma physics is an expanding and interesting field of physical sciences. "Plasma" is a state of matter and can be defined as partially or fully ionized matter which contains positive and negative particles and is on a macroscopic scale electrically neutral. More recently there is an arising interest in the study of dusty plasmas, a very fast growing branch of physics. As the name reveals, dusty plasmas are plasmas which also contain nanometer to millimeter-sized particles [5]. The field of dusty plasmas mainly deals with the study of dust charging, plasma-dust and dust-dust interaction, their collective effects as well as the formation of dust crystals. Dusty plasmas are encountered in many areas of physical sciences [6, 7]. They are found on a vast variety of scale lengths in nature, e.g. in astrophysical objects like interstellar clouds, rings of planets, comet tails [8–11]. Dusty plasmas are also encountered in laboratory, e.g. in fusion devices [12], and also in industrial plasmas (etching, deposition, ...) [13–21]. Thus, the study of dusty plasmas has relevance to many areas of science.

The study of charging mechanisms and forces on dust constitutes a fundamental and important part of dusty plasma physics. The dust particles are charged due to the inflow of the plasma species by various mechanisms [6, 7, 22], e.g. absorption of electrons, ions and secondary electron emission, etc. The charge and the floating potential of the dust are very crucial parameters that govern many important observed phenomena in dusty plasmas. The formation of dust structures [23–26], wake-field formation around dust in rf sheaths [27, 28] and the dust void formation in microgravity dusty plasma experiments [29–31] are examples of such phenomena. The ion drag force - the force exerted on dust grains by traversing ions around the dust due to collection and scattering- plays a crucial role in the above phenomena. Hence, to fully under-

stand and explain these phenomena, one has to have quantitative knowledge of the ion drag force and how dust particles interact with other dust particles. As the ions are deflected by the electric field of the dust, the ion drag force on the dust depends on the dust potential, dust charge and potential distribution around the dust. These dust parameters themselves depend on dust-plasma interaction [6] and plasma characteristics. Plasma species distribution, collisions among various plasma species govern the amounts of plasma particles flow to the dust thereby determining the dust charging and other important dust parameters. This means that the plasma background governs all these processes. A rf discharge plasma is commonly used as background plasma environment for dusty plasma experiments in the laboratory [32]. Since in rf discharges the plasma bulk and sheath have different properties (e.g. ion velocities), the dust charge and potential can vary for dust grains located at different positions in the rf discharge. Laboratory dusty plasma experiments are conducted with rf discharges at pressures up to a few hundred Pa and rf voltages up to a few hundred volts. For these conditions the background plasma is collisional and electrons are non-Maxwellian. Quantification of dust charge, floating potential, dust potential distribution, ion drag force on dust and study of dust-dust interaction over the entire range of collisionality and for all flow velocities is at the heart of the dusty plasma research.

Many analytical models are existing to compute dust charge and floating potentials [2, 3, 33–38] for a collisionless or very low collisionality plasma background, but they do not account for streaming plasma conditions. Recently, some analytical or computational works have been available [4, 39–44] which compute dust parameters over the entire range of collisionality and also account for the ion flow. But, these works assume electrons with a Maxwellian distribution, whereas the electrons and ions are shown to be non-Maxwellian in rf discharges [45, 46]. The problems are similar for the ion drag quantification [2, 40–43, 47–49]. Also, it is widely considered that the dust potential distribution is Debye-Hückel-like [6, 7] and that in the plasma bulk the dust potential is mainly shielded by ions and in the sheath region by electrons [6]. But, it is not yet clear how the flowing plasma and/or collisions affect the potential distribution and shielding lengths, though there was some focus on this issue recently [50], but only for the highly collisional limit. Hence, the limitation of the analytical models is the incomplete treatment of collisions and non-Maxwellian distributions. That is why, quantification of dust charge, floating potential, dust potential distribution, shielding lengths for realistic background plasma discharge conditions is still open.

It is believed that with the presence of many dust particles electron depletion takes

place and the charge on the dust decreases [6, 22]. However, the mechanism of how two dust particles interact or how charging dynamics of a dust particle get affected in the presence of other dust particles is yet to be studied at the kinetic level. It is usually believed that there is a certain separation between given dust particles ("interaction distance") within which the interaction of two neighboring dust particles must be taken into account. It is not clear whether this separation distance is the electron Debye length or the shielding length. Even without the issue of separation distance, the mechanism of how dust parameters evolve with the presence of neighboring dust particles is still open for further investigation.

In this thesis, some of the above issues are addressed using self-consistent three-dimensional kinetic simulations with a Particle-particle-particle-mesh (P^3M) code. With this computational tool, it is possible to resolve sheath regions around electrodes in rf discharges and to obtain realistic energy distributions of plasma species. The code also resolves close-range interactions of dust with the plasma. Hence, the main motivation of this thesis is to address the following issues:

- What is the effect of collisions among plasma species on discharge characteristics and thereby on charging dynamics and ion drag force?

- How do parameters like charge, floating potential, shielding length, and the ion drag force on dust vary for different positions of dust in rf discharges?

- How do values from various analytical models of dust charge and ion drag force compare with computational results for realistic discharge conditions?

- How do the dust charge, floating potential and ion drag force on the dust evolve in the presence of neighboring dust particles?

The thesis starts with an introduction to dusty plasmas and rf discharges. Charging mechanisms, theoretical and computational works on dust charging are discussed. Various forces acting on a dust particle suspended in rf discharges are presented. The analytical and computational models for quantification of the ion drag force on dust are also discussed. Experiments to confine and form various dust structures in laboratory and under microgravity are briefed.

The computational tool used is described in detail in chapter 3. Here, a general introduction to kinetic (Particle-in-Cell) simulations is provided. Then, the limitation of the conventional PIC method is described in resolving particle interaction closer

than the grid spacing. It is also explained how this problem can be overcome with the Particle-Particle-Particle-Mesh (P^3M) code.

Before attempting to study dust charging, the characteristics of rf discharges have to be studied carefully, as the behavior of plasma species in the discharge govern the charging processes. Hence, the characteristics of rf discharges, sheath dynamics and species distributions have been computed for typical laboratory conditions and are presented in chapter 4.

After the background plasma discharge characteristics are understood, dust particles of various sizes are introduced into the discharge at different positions and the dust charge, floating potential, shielding lengths are computed. These computed results are presented in chapter 5. The scaling of dust charge and floating potential with dust size is derived. The computed dust parameters are also compared to those calculated from theoretical models.

In chapter 6, computational results for the ion drag force acting on dust particles immersed in a rf discharge are presented. Effect of collisions on the ion drag force is discussed in detail along with the scaling with dust size.

This study of charging is extended to two and multiple dust particles. In chapter 7, computational results for charge and drag force on multiple static dust particles immersed in the rf discharge are presented. The case of two dust particles is treated in detail.

Chapter 2

Dusty plasmas: Basics

The background plasma properties govern the charging processes thereby determining the dust charge, dust floating potential, dust potential distribution and ion drag force on the dust. Hence, in this chapter basic properties of the plasmas, rf discharges and the theory of dusty plasmas are reviewed.

2.1 Plasma properties

A plasma is defined as quasineutral, partially or fully ionized gas that exhibits collective behavior [51]. It is considered to be the fourth state of matter and is the most prevalent state in the universe. The fundamental work in the field was done by, among others, Schottky, Child, Chen, and Langmuir [51–57]. Plasmas are typically characterized by a number of parameters. "Plasma density" usually refers to the "electron density"(n_e), that is, the number of free electrons per unit volume. The degree of ionization (α) of a plasma is the proportion of atoms which have lost (or gained) electrons. $\alpha = n_i/(n_i + n_n)$ where n_i is the number density of ions and n_n is the number density of neutral atoms. The electron density is obtained from the average charge state $< Z >$ of the ions through $n_e = < Z > n_i$.

Plasma temperature is a measure of the thermal kinetic energy per particle. If the electrons are close enough to thermal equilibrium and their distribution function is close to a Maxwellian, their temperature is well-defined. However, it could deviate from a Maxwellian distribution due to various reasons, e.g. by the presence of strong electric fields or inelastic collisions. In the case of species with non-Maxwellian distribution function, the mean kinetic energy of the particles is equated to "kT" to derive the

approximate temperature of the species. Because of the large difference in mass, the electrons come to thermodynamic equilibrium amongst themselves much faster than they equilibrate with the ions or neutral atoms. For this reason the "ion temperature" (T_i) may be very different from (usually lower than) the "electron temperature"(T_e) . This is especially common in weakly ionized technological plasmas, where the ions are often near the ambient temperature. "Thermal plasmas" have electrons and the heavy particles at the same temperature i.e. they are in thermal equilibrium with each other. "Non-thermal plasmas" have the ions and neutrals at a much lower temperature (normally room temperature), but electrons are much "hotter".

In a neutral plasma, if one displaces by a tiny amount all of the electrons with respect to the ions, the Coulomb force pulls back, acting as a restoring force. Because of the combined effect of inertia and the restoring force, the electrons oscillate around their mean position. These oscillations are called "electron plasma oscillations" and the oscillation frequency is the "electron plasma frequency" given by $\omega_{pe} = \sqrt{n_e e^2/m_e \epsilon_0}$ $[sec^{-1}]$, where m_e and n_e are electron mass and density. Similarly the "ion plasma frequency" is given by $\omega_{pi} = \sqrt{n_i e^2/m_i \epsilon_0}$ $[sec^{-1}]$, where m_i and n_i are ion mass and density. Since $m_e \ll m_i$, $\omega_{pi} \ll \omega_{pe}$ always holds.

2.2 RF discharges

Capacitively coupled radio-frequency discharges are normally used for dusty plasma experiments. Hence, before discussing dusty plasmas and dust charging, one should first understand the characteristics of rf discharges.

A schematic illustration of an rf discharge is shown in Fig. 2.1. One electrode is powered with an alternating voltage of 13.56 MHz via a blocking capacitor and the other one is grounded. The blocking capacitor prevents from direct currents between the electrode and the rf-generator. Plasma created between the electrodes will shield the electric field of the electrodes. Electrons are mobile and will respond to the instantaneous electric field. Ions will only respond to average fields, since $\omega_{pi} \ll \omega_{RF} \ll \omega_{pe}$ holds, where ω_{RF} is the applied rf source frequency. Due to their larger mobility electrons bombard the electrodes initially resulting in a negative net charge on them. These electrodes begin to repel electrons and attract ions until the ion and electron fluxes balance. The plasma must then have positive potential with respect to the wall. This potential cannot be distributed over the entire plasma, since Debye shielding will con-
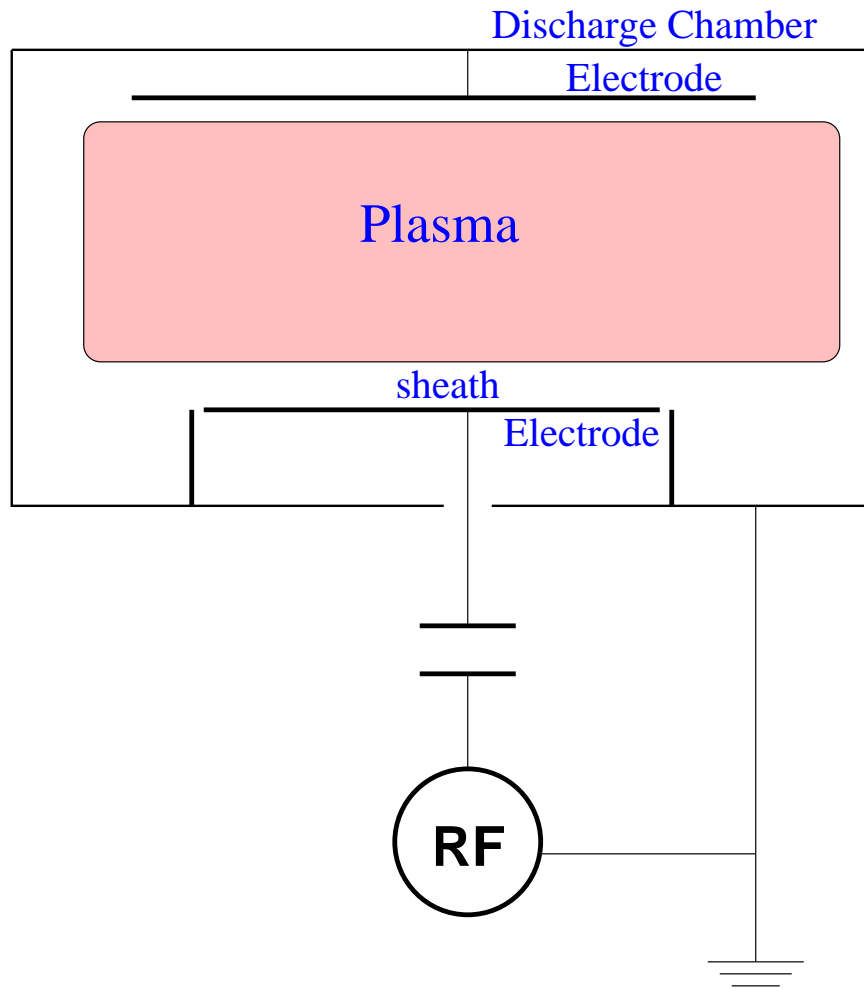
Figure 2.1: Schematic sketch of an rf discharge.

fine the potential variation to a layer of the order of several Debye lengths in thickness. In this region around the electrodes, the quasineutrality condition is broken, where the net ion density is greater than the electron density, i.e., $n_i \gg n_e$. This space charge region between the quasineutral plasma and the electrode is called "plasma sheath". In this region, strong electric fields develop. This leads to a constant ion flow to the electrodes. But, as the electrons respond to instantaneous field, they can not flow to electrodes all the times. In rf discharges as the applied field at the Electrodes varies with time, the sheath voltage also oscillates. At certain times, the sheath voltage drops or even electrodes become positive. At these times, electrons flow to electrodes in pulses.

Bohm [58] showed that in order to form this sheath, positive ions must possess a

certain minimum energy (Bohm criterion), where the ion speed should satisfy $v_{ion} \geq C_{Bohm} = \sqrt{kT_e/m_i}$ where C_{Bohm} is called the Bohm speed (sound speed of the ions). It has further been shown [1] that there exists a transition region (called also "presheath") where potentials on the order of the Bohm potential ($\phi_{Bohm} = kT_e/2e$) exist. In this region the ions are accelerated from thermal speeds to Bohm speed. Hence, the plasma sheath ranges from the boundary to the sheath entrance, where the ion speed becomes subsonic. The presheath connects the sheath boundary to the bulk (see Fig. 2.2). In collisional plasmas, the Bohm criterion is not met and subsonic ion flows exist [59–64]. This subject will be discussed later on.
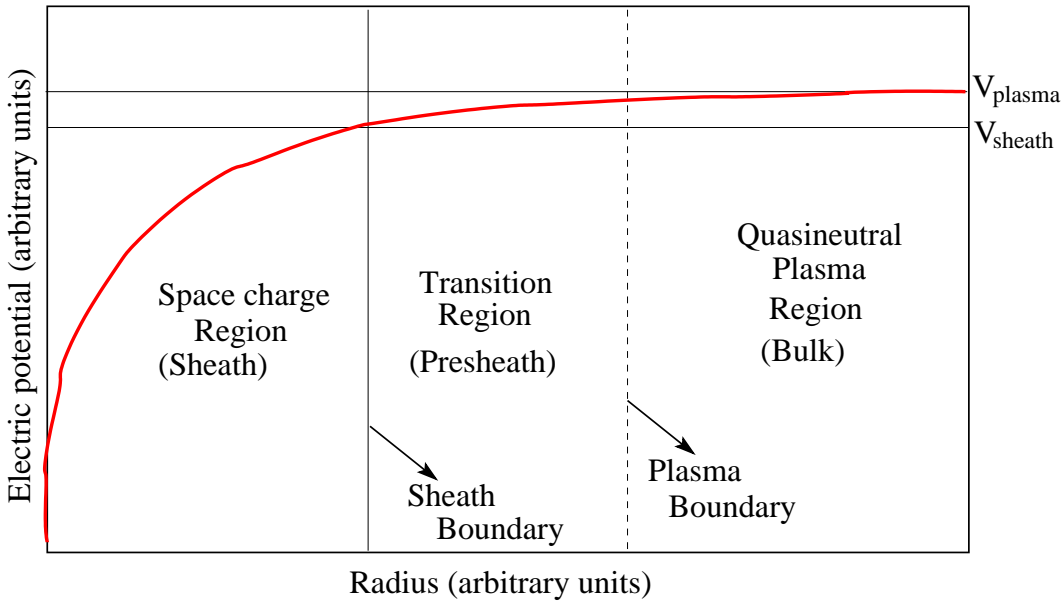
Figure 2.2: Schematic showing the regions present near a boundary of a collisionless plasma.

   The mechanism of electron heating is responsible for plasma sustenance. Ohmic heating, in which the electrons are accelerated in the strong electric field between successive elastic collisions with neutrals, can dominate at high pressures. In a low pressure regime (less than 10 Pa) electron-neutral collisions are rare, and the Ohmic heating ceases to be an effective mechanism of energy deposition into the plasma. In this case, the electron heating by time-varying fields can dominate. It occurs due to electron oscillatory motion in spatially inhomogeneous rf fields, even in the absence of collisions, leading to collisionless or stochastic heating. Generally, electrons are heated collisionlessly by repeated collisions with sheath edge, i.e. with fields that are localized within a sheath. For further reading on heating mechanism and rf discharges, one can

refer to [32, 65].

2.3 Dusty plasma

A dusty plasma is an ionized gas containing a suspension of solid particles. These particles are usually nanometer or micron-sized, and they are often called *dust*. *Dusty plasmas* are also called *colloidal*, or *fine particle plasmas*, and an alternatively used term is *complex plasmas* in analogy to *complex fluids*, which emphasizes many fundamental properties of this medium that distinguishes it from ordinary gas plasmas. Dust and dusty plasmas are ubiquitous in space. They are found in the ring systems of the giant planets, in comet tails, in the interplanetary medium, and in interstellar clouds as well as in mesospheric noctilucent clouds [10, 66, 67]. Dusty plasmas are found nearby artificial satellites and spacecrafts [67, 68], and in fusion devices with magnetic confinement [69, 70]. Additionally, dusty plasmas are being investigated very intensively in laboratories. Dust can be intentionally added to a plasma or it can be spontaneously generated as a result of various chemical processes leading to the growth of particles. From the industrial point of view dusty plasmas can have "good" and "bad" impacts on technology. The "bad" impact is due to dust contamination problems [71]. And a "good" impact is connected to the formation of new materials [72]. An interesting application of dusty plasmas was found in solar cell technology [73], where the formation of nanoparticles inside a solar cell has beneficial effect in lifetime and efficiency of the cell. Widespread occurrence of dusty plasma systems and a number of unique properties make dusty plasmas an extremely attracting and interesting object for investigations.

2.4 Dust charging

A dust particle in a plasma acquires a large electric charge by collecting electrons and ions from the plasma [10, 66]. Complex plasmas with nanometer-sized particles, to some extent, behave like negative ion-containing plasmas, where a part of the negative electron charge is bound to heavier particles. This affects the mobility and the contribution to shielding by negative charges. However, the properties of dusty plasmas are much richer than the properties of a usual multi-component plasma of electrons and various kinds of ions. Dust particles are the recombination centers for plasma electrons

and ions. Sometimes they can also serve as the sources of electrons via thermo-, photo-, and secondary electron emission processes. Thereby, a dust component can make an essential impact upon the ionization equilibrium. Unlike negative plasma ions, the dust microparticle charge is not fixed, but it becomes a dynamic variable, which is governed by the surrounding plasma, and can change both spatially and temporally. Moreover, the dust charge fluctuates even for constant plasma parameters due to the stochastic nature of charging [26, 74, 75].

The particle charge is the most fundamental parameter in a dusty plasma because it determines the interaction forces between individual dust particles. Some of the important theoretical, computational and experimental works to obtain dust charge are described below.

2.4.1   Analytical and computational models of dust charging

The problem of particle charging is closely related to probe theory, founded in 1920s by Mott-Smith and Langmuir [33]. Probe theories calculate the current to an electrostatic probe as a function of probe potential and probe shape. The floating potential is derived as the point where ion and electron currents balance. Later, probe theory has been applied to dust charging, where given the plasma densities the dust floating potential is derived.

OML Theory

First probe theories based on orbital motion, Orbit Motion Limited (OML) theory, was put forth by Mott-Smith and Langmuir [3, 33, 74]. Here, the angular momentum of the ions imposes a limit on the maximum ion current. A quasi-neutral, collisionless plasma with Maxwellian distributions of electrons and ions is assumed. The OML theory is often used as a "standard" model for the calculation of a particle charge. In this theory, a single particle is considered as an isolated, floating spherical probe and plasma parameters are assumed to be known. In this case, the ion current to the particle with the radius r_d is given by (at the particle potential $\phi_p < 0$)

$$I_i = \pi r_d^2 n_i e v_{th,i} \left(1 - \frac{e\phi_p}{kT_i} \right), \tag{2.1}$$

where the term $n_i e v_{th,i}$ is the ion flux to the particle at the mean thermal velocity of ions

$$v_{th,i} = \sqrt{\frac{8kT_i}{\pi m_i}}. \tag{2.2}$$

and the term

$$\sigma_c = \pi b_c^2 = \pi r_d^2 \left(1 - \frac{e\phi_p}{kT_i} \right) \tag{2.3}$$

is the effective collision cross-section of the particle with the ions, which have the typical ion energy of $E_i = kT_i$. This cross-section is larger than the geometrical cross-section of the particle due to the attractive particle potential. Correspondingly, the electron current to the particle is given by

$$I_e = -\pi r_d^2 n_e e v_{th,e} \exp \left(\frac{e\phi_p}{kT_e} \right), \tag{2.4}$$

where

$$v_{th,e} = \sqrt{\frac{8kT_e}{\pi m_e}} \tag{2.5}$$

is the electron thermal velocity. The exponential factor in Eq. (2.4) is the Boltzmann factor for electrons leading to the decrease of the electron density at the negative particle potential. Steady state is reached if electron and ion currents balance each other and the total current to the particle vanishes. For the equilibrium potential ϕ_p of a dust particle with a charge Q holds

$$\frac{dQ}{dt} = I_i(\phi_p) + I_e(\phi_p) = 0. \tag{2.6}$$

This so-called floating potential is typically negative relative to the ambient plasma, due to the much higher mobility of electrons compared to ions. Substituting Eq. (2.1) and Eq. (2.4) in Eq. (2.6) one obtains

$$1 - \frac{e\phi_p}{kT_i} = \sqrt{\frac{m_i T_e}{m_e T_i}} \frac{n_e}{n_i} \exp \left(\frac{e\phi_p}{kT_e} \right). \tag{2.7}$$

The numerical solution of this equation gives ϕ_p as a function of the given plasma parameters. Then, the dust charge can be derived from the floating potential assuming the particle as a spherical capacitor, using

$$Q = 4\pi\epsilon_0 r_d \left(1 + \frac{r_d}{\lambda_D} \right) \phi_p \tag{2.8}$$

The term in parenthesis is due to the plasma shielding effect and is discussed later.

Limitations: There have been many refinements to the OML theory. Limitations and applicability of these theories have been dealt previously by e.g. [1, 3, 34–38, 58, 76–78]. Here, we mention a few limitations. The OML model assumes collisionless ion trajectories. This condition is often violated in plasma discharges. It has been shown [34] that due to collisions near the probe, some of the charged plasma particles can be trapped in the potential well and this can play a very important role, e.g. affect shielding lengths. OML does not include the existence of an absorption radius around the dust and predicts a dust potential independent of dust size [34, 35, 76]. The other limitation is important for big particles ($r_d \geq \lambda_D$) and connected with the existence of an angular moment barrier.

OM Theory

More general Orbital Motion (OM) theory [34, 35] involves solving simultaneously for the surface potential, the potential distribution around the probe, and the distribution of ion trajectories. Here, the angular momentum of the plasma particle around the probe is treated as an effective radial potential energy [79] and is added to the probe's electrical potential and the trajectories of plasma particles are solved in the total radial potential as a function of particle's angular momentum. In the OM theory, the probe radius becomes an important factor in determining whether a particle of a given energy and angular momentum will contribute to the current towards the probe, i.e., the current is no longer a function of probe cross section as in OML theory. For zero angular momentum, i.e., for purely radial motion, all particles will eventually strike the probe, irrespective of the particle's initial energy and the probe radius. It also shows the existence of an absorption radius when the angular momentum is less than some critical value. All particles that pass the absorption radius will eventually reach the probe, i.e., the absorption radius determines the probe characteristics, not the probe radius. The main limitation of the OM theory is that the collisional effects between

charged plasma species and the background gas have not been considered.

ABR Theory

Radial Motion theory proposed by Allen, Boyd and Reynolds (ABR)[1, 36] includes
a pre-sheath transition region where quasi-neutrality is satisfied but potentials on the
order of the Bohm potential [58] are allowed to exist. ABR theory is the limiting case
of the OML for the limit of vanishing impact parameter (b → 0) and the limiting
case of the general OM theory for the limit of vanishing angular momentum (J → 0).
This work results in floating surface potentials as a function of probe radius as shown
in Fig. 2.3. This is used to compare with the simulation results of the dust surface
potential shown in chapter 5 of the thesis. A limitation of the ABR model is that it
predicts a single value for the dust potential for a given dust size and Debye length ratio,
irrespective of collisionality. The collisional effects between charged plasma species and
the background gas have not been considered.

Lampe et. al. [37, 38], Ratynskaia et. al. [80] and Khrapak et. al. [2] considered
charge-exchange collisions between ions and neutrals, as these collisions are particularly
effective in creating trapped ions. These models are reviewed below.
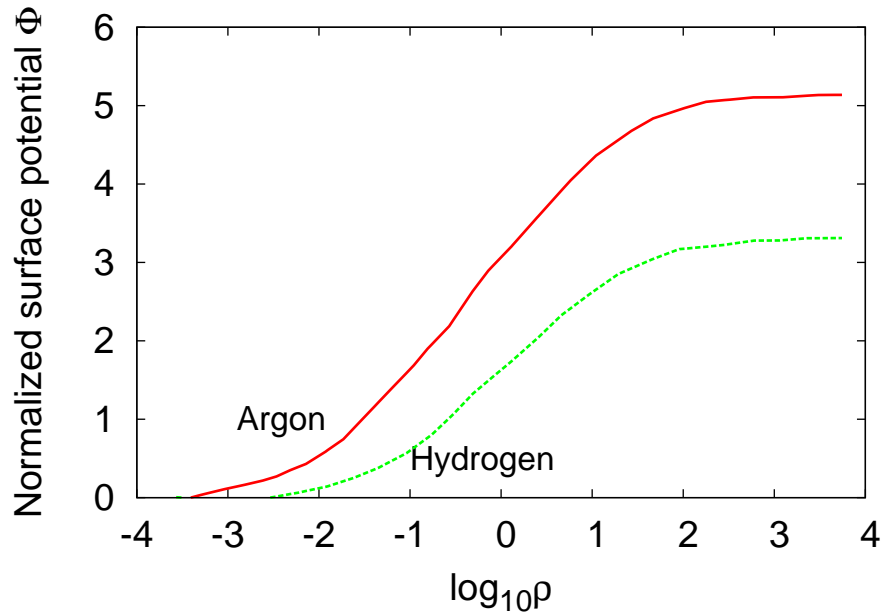
Figure 2.3: Probe floating potential $\Phi = -e\phi_p/kT_e$ as a function of probe radius $\rho = r_d/\lambda_D$ from the
ABR model (extracted from [36]).

Lampe Theory

Lampe et. al. [37, 38] considered charge-exchange (CX) collisions between ions and neutrals to compute the corrections to OML ion flux due to these collisions. Due to CX collisions, high energy ions are replaced by low energy ions, which might be absorbed by the dust grain or can be trapped. Trapped ions experiencing further collisions will fall onto the grain. Lampe's model considers these issues and computes the trapped ion density near the grain and then computes the collisional contribution to the ion current to the probe. This work delivers floating potentials as a function of collisionality index $\nu\lambda_D/v_{th}$, for the cases of collisionless plasmas and weak collisionality as shown in Fig. 2.4 (extracted from [38]). Here ν is the mean free path for CX collisions, λ_D is Debye length and v_{th} is ion thermal velocity.

The Lampe model assumes Maxwellian distributions for all plasma species in the ambient plasma and the dust grains are assumed to be small compared to the linearized Debye length (λ). Here $\lambda^{-2} = \lambda_{De}^{-2} + \lambda_{Di}^{-2}$ where λ_{De} and λ_{Di} are electron and ion Debye lengths respectively. The model is applicable for weakly collisional background. The model also assumes nonflowing plasma.
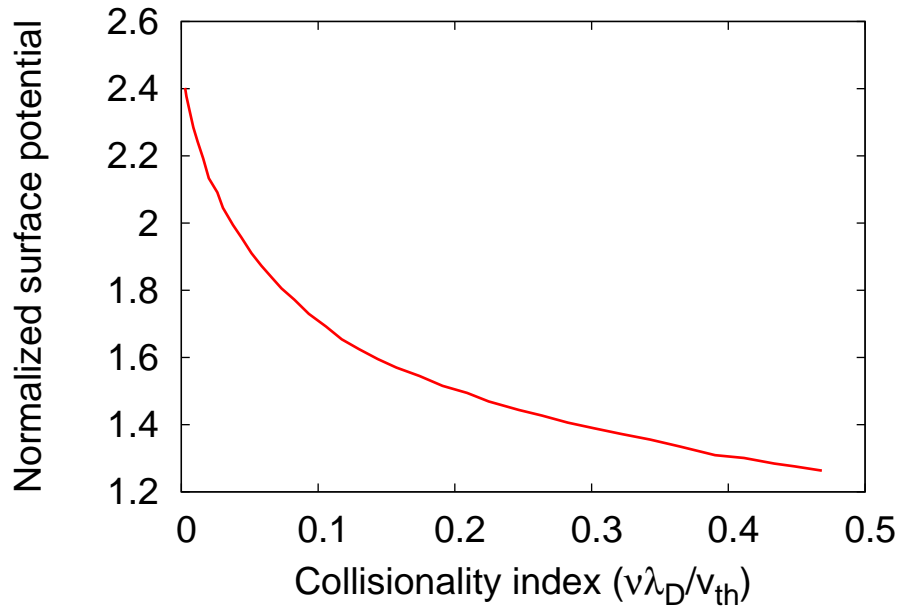
Figure 2.4: Probe floating potential $\Phi = -e\phi_p/kT_e$ as a function of collisionality index $\nu\lambda_D/v_{th}$ from the model of Lampe (extracted from [38]).

Khrapak Theory

Khrapak et. al. [2] also considered charge-exchange collisions between ions and neutrals, including collisions occurring in the sheath around the dust grain, to compute the additional collisional ion current to grain. It is a simplified form of the Lampe's equation and is given by

$$I_i = \sqrt{8\pi} \; r_d^2 \; n_i \; v_{Ti} \; \Phi \; \tau \; \left[1 + 0.1 \; \Phi \; \tau \left(\frac{\lambda}{l_i} \right) \right] \tag{2.9}$$

where l_i is the mean-free-path of CX collision, $\tau = T_e/T_i$ is electron-to-ion temperature ratio. The Khrapak model is applicable for weakly collisional and nonflowing plasmas.

Zobnin Theory

Both Lampe and Khrapak models provide approximations to ion currents to the grain at zero or small collisionality. For highly collisional cases, a continuum fluid approach is valid. However, the above models do not provide collisional ion current contributions at intermediate collisionality. Zobnin's work fills this gap.

The kinetic equation with a Bhatnagar-Gross-Krook collision term [4, 39] was solved to obtain the ion flux on a small attractive spherical dust and the electric potential distribution around the dust. It is shown that the ion current nonmonotonically depends on the ion-neutral collision frequency and exhibits a maximum when the mean free path length of ions is comparable to the effective absorption radius of the probe. An analytical fit was proposed to calculate the ion current for intermediate collisionality over a restricted range of probe sizes and probe potentials [4] where neither a collisionless theory nor a continuum fluid approach is valid. This approximation can also be used for the calculation of the floating potential and charge of the dust in an uniform plasma with known electron distribution function.

The above mentioned analytical fit is used in this thesis to compare with the results from our simulations. The Zobnin theory does not account for non-Maxwellian electrons and for flowing plasmas.

Hutchinson's work

Hutchinson et. al. [40–42, 44] performed kinetic simulations using the SCEPTIC PIC code to compute ion currents to a probe. Here, only ion trajectories are followed while electrons are treated as background with Boltzmann distribution. They computed

initially [40–42] ion currents to a probe for both stationary and flowing collisionless plasmas over a wide range of λ_D/r_d ratio and ion temperatures. From the computed ion currents and known electron density, the potential distribution around the grain was derived. The results show that for large values of λ_{De}/r_d, OML expression with a proper drifting ion distribution provides reasonable measure of the total ion flux to a floating sphere. The asymmetry in ion flux to the sphere surface was studied in detail for a wide range of Debye-lengths and found a reversal of the asymmetry of the collection flux at values of the Debye length of the same order of magnitude as the probe radius. The enhancement of collection on the downstream side was due to focusing of the ions by the shielded potential surrounding the probe.

Later, they extended their study by including CX ion-neutral collisions [44]. The work computes the ion flux to the dust grain over the full range of collisionality from zero to the continuum limit. It was shown that a low level of ion-neutral collisions enhances the ion collection to a sphere in a plasma with shielding length larger than its radius. The ion flux matches with OML values for collisionless case and with continuum fluid theories for highly collisional (continuum) case. Maximum flux enhancement observed was roughly equal to values predicted by ABR theory. All these computations assume Boltzmann electrons.

Kinetic simulations

The above analytical theories generally do not account for streaming ions leading to difficulties in determining the charge of dust located in the sheath. In the case of OML [3], streaming effects can be included in ion flux calculations. Maxwellian distributions for the electrons are assumed in nearly all cases, and a variety of distributions from monoenergetic to Maxwellian are typically assumed for the ion distributions [81–84]. However, for rf plasmas, electrons usually have non-Maxwellian and sometimes bi-Maxwellian energy distributions [45, 46]. Ions are also far from Maxwellian, as they become accelerated in sheaths acquiring a high streaming velocity.

Kinetic simulations are promising tools for computations of dust charge, potential and potential distribution around dust for realistic experimental conditions. The reason is that these models include nearly all types of possible collisions, they track the trajectories of the plasma species and also account for non-Maxwellian distributions of the plasma species.

2.4.2   Experiments for dust charge measurement

Here, we briefly mention main experimental techniques employed to derive the dust charge. These include

- **oscillations in the sheath** [26, 75, 85–88]: In this method, dust is driven and made to oscillate in the sheath either by inducing a time varying potential across the sheath or by using a laser. The dust particle trajectories are recorded and analysed. Harmonic resonance equations exploiting the force balance of electric field force and gravity are then solved to determine the charge.

- **collisions of dust particle pairs** [29, 89–91]: Here, collisions between dust particle pairs are employed to deduce the interaction potential of the collision and from this potential the dust charge is derived.

- **waves** [92, 93]: In this method, waves are excited in a dust system by the radiation pressure of a laser beam and the dispersion relation is measured. The measured dispersion relation is compared with that of a dust lattice wave to obtain the dust charge and shielding length.

- **direct measurement with Faraday-cup** [94, 95]: Here, dust is dropped into the plasma by a dropper at the top and the charge is measured by a Faraday cup below the plasma.

The experimentally determined charges are normally of the same order expected from the models. The experimental results support the existence of a harmonic sheath potential. The charge numbers obtained from experiments agree somewhat better with ABR theory. The experiments also deliver coupling parameters (see below) and shielding strengths. However, the following factors are some of the sources of inaccuracies in the charge numbers obtained from experiments. Assumptions about sheath potential, uncertainties in locating sheath boundary, inaccuracies involved in mapping of dust positions from recorded images.

2.4.3   Dust potential distribution

In plasmas, electrons and ions screen out electric fields so that the interparticle interaction potential decreases more rapidly with the distance than a Coulomb potential. This effect is taken into account through the so-called Debye-Hückel or Yukawa potential with the screening length λ_D. The shielded potential is expressed by

$$\phi(r) = \frac{Q}{4\pi\epsilon_0 \ r} \exp\left(-\frac{r}{\lambda_D}\right).$$ (2.10)

Considering the shielding effect the particle charge can be written as

$$Q = 4\pi\epsilon_0 r_d \left(1 + \frac{r_d}{\lambda_D}\right)\phi_p$$ (2.11)

which in the typical case of $r_d \ll \lambda_D$ reduces to the vacuum value $4\pi\epsilon_0 r_d\phi_p$.

2.4.4   Temporal evolution of the particle charge

In the previous discussions, the particle charge has been considered as static. However, the temporal evolution of the particle charge can have a strong influence on the dynamical properties of dusty plasmas [74, 96]. The time scale of ion charging can be written as [97]

$$\tau_i = 4\pi\epsilon_0 r_d \frac{kT_i}{e} \frac{1}{\pi r_d^2 e n_i v_{th,i}},$$ (2.12)

which can be understood as the charging time $\tau = RC$ of an RC system with the particle capacitance $C = 4\pi\epsilon_0 r_d$ and the resistance $R = U/I$. $U = kT_i/e$ is the usual electric potential of the particle and $I = \pi r_d^2 e n_i v_{th,i}$ is the typical OML ion current to the particle. The expression for the electron charging time is similar to Eq. (2.12). The difference is only that the ion quantities are replaced by those of electrons:

$$\tau_e = 4\pi\epsilon_0 r_d \frac{kT_e}{e} \frac{1}{\pi r_d^2 e n_e v_{th,e}}.$$ (2.13)

Usually, $\tau_e \ll \tau_i$ because the particle encounters with electrons are more frequent than with ions so that the charging time is dominated by the slower ions.

The typical particle charging time is of the order of micro-seconds. This is much less than the typical dynamical time scale of the particles, which is of the order of tens of milliseconds. It means that the particle charge should always be in equilibrium with the particle motion. However, as it was observed by Nunomura et. al [91], the finite charging time of particles can lead to a delay in charge variation with the local plasma conditions when particles move.

Another evolution mechanism of the charge of dust particles is due to the discreteness of the charge carries and their charges [96]. At floating potential the probabilities

of collecting a single ion or electron by the particle are equal, hence the particle charge fluctuates stochastically around its equilibrium position. The amplitude of this fluctuations are $\delta Z_{rms} = 0.5\sqrt{Z_{eq}}$, where Z_{eq} is the mean particle charge.

2.4.5   Charging with high dust densities
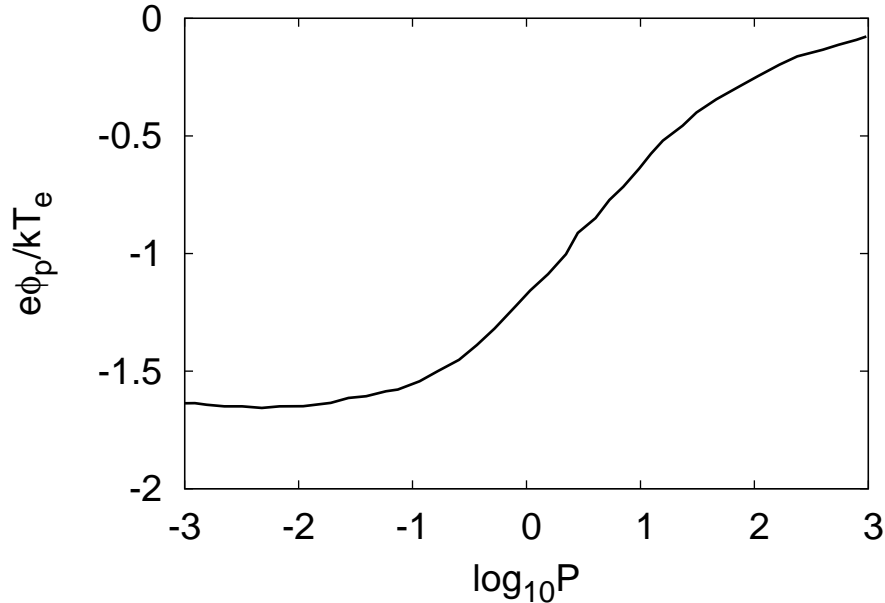
Figure 2.5: Particle floating potential as a function of the Havnes parameter P, for T_e/T_i=100 in Helium [98].

So far, it was assumed that the dust does not have an essential influence on an ambient plasma. At higher charge density, the dust charge density contribution $n_d Z_d e$ modifies the quasineutrality condition by

$$n_e = n_i e - n_d Z_d e = n_i e - n_d \; 4\pi\epsilon_0 r_d \; \phi_p. \tag{2.14}$$

Thus, high enough dust densities n_d lead to electron depletion in the plasma. Then, there are not enough free electrons available to charge the dust particle to the undisturbed potential value. The influence of the dust is described through the so-called Havnes-parameter [98], which is the dust charge density in units of the electron density

$$P = 695 T_{e,eV} a_{\mu m} \frac{n_d}{n_e}, \tag{2.15}$$

where $T_{e,eV}$ is the electron temperature in electron volts and $a_{\mu m}$ is the particle radius in microns.

In the single particle limit $P \to 0$ the floating potential ϕ_p corresponds to the undisturbed floating potential and approaches $\phi_p \to 0$ as $P \to \infty$ as shown in Fig. 2.5.

2.5 Forces acting on dust particles

Generally, the trapping and transport of dust particles in a plasma is governed by the forces acting on them [47]. The forces acting on the dust include gravity, electric forces, ion drag force [48, 49, 99–102], thermophoresis due to temperature gradients [103], polarization forces due to electric field gradients [104–106], and the neutral drag due to gas molecules collisions with dust particles when the particle is moving [107]. In a plasma under laboratory conditions, the electric field force, gravity, the neutral drag and thermophoresis are found to be the most important [75, 101, 102, 108, 109]. In the Fig. 2.6 a conceptual sketch is shown which represents how these forces act. Here, a short description of these forces will be given.
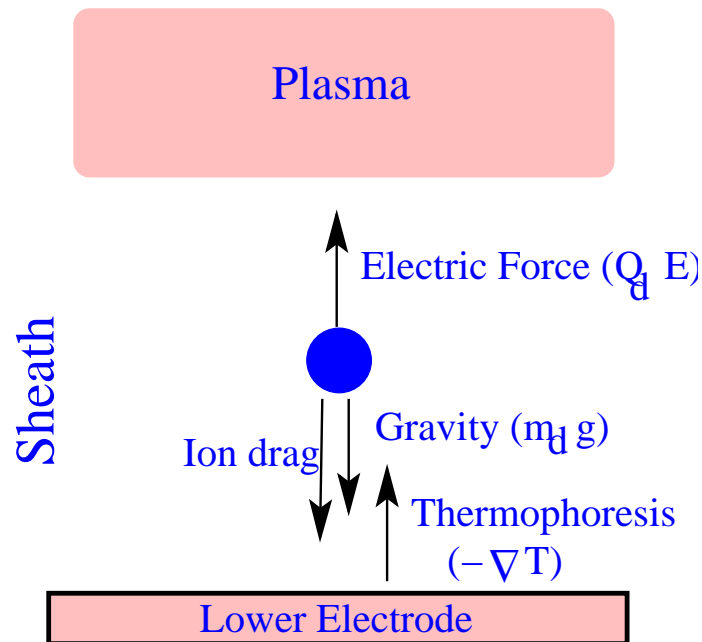
Figure 2.6: A sketch showing various forces acting on dust particle in rf discharges.

Gravity

A dust particle in a plasma has a huge mass compared to other plasma species. This makes the gravitational force to be one of the dominant forces in dusty plasmas. The gravitational force is proportional to the particle mass, i.e. to the dust particle volume and its mass density ρ:

$$\vec{F}_g = m_d \vec{g} = \frac{4}{3} \pi r_d^3 \rho_d \vec{g}, \tag{2.16}$$

where r_d and ρ_d is the dust particle radius and density, correspondingly. This makes the gravitational force to be proportional to the cube of the dust particle radius.

Electric force

Due to its charge, a dust particle is affected by electrical fields that are present in the plasma. The large inertia of a dust prevents the particle from following the oscillating rf field. Hence, the microparticles are only affected by time-averaged electrical fields. In rf-plasmas, the time-averaged plasma potential reaches its maximum value in the center of the discharge and decreases towards the plasma reactor walls and electrodes [32]. Thus, an electric force pushes the negative dust particle towards the discharge center.

An electrostatic force acting on the dust particle in a plasma in the presence of an external electric field $\vec{E}$ is well approximated by the vacuum force [104]

$$\vec{F}_{el} = Q\vec{E} \tag{2.17}$$

when the dust particle radius a is smaller than the linearized Debye length λ_D.

It is important to note that, although the sheath around a dust particle shields it from the surrounding plasma, it does not screen the particle from an externally applied electric field. It was pointed out in [105] that the Debye sphere around the dust particle is not attached to the particle and represents only a local perturbation of the background plasma.

In the space charge sheath, a spatially dependent electric field prevails. Due to the drop of plasma potential towards the electrode the electric force increases in this direction. As a result, there will be in many cases a unique vertical position where this force acting on the negatively charged dust particle balances gravity. At this position the dust particle is trapped and a horizontally extended plasma crystal can be formed.

Such crystals contain typically one to several thousands charged dust particles [24, 26–28, 110–116]. In the plasma bulk, the electric force is much weaker compared to the sheath situation.

Neutral drag

Dust particles moving in a plasma environment experience a friction force due to momentum transfer with the residual gas [117]. There are two regimes of this force which depend on the Knudsen number K_n. The Knudsen number is the ratio of the mean free path of a neutral gas molecule and the radius of the dust particle, $K_n = \lambda_m/r_d$. For small K_n values the neutral drag force is obtained from Stokes' law. However, in the regime typical for rf discharges of dusty plasma experiments, the mean free path of the gas molecules is much larger than a few hundred micrometers. This is much larger than the typical dust particle radius r_d, which is of the order of several micrometers. It makes the Knudsen parameter to be much larger than one. Such a regime is called 'kinetic' or 'long mean free path'.

For low relative speeds between microsphere and neutral gas the neutral drag in the kinetic regime can be well approximated by the Epstein relation [107]

$$\vec{F}_{Nd} = -\delta \frac{4}{3}\pi r_d^2 m_{gas} n_{gas} v_{th,gas} \vec{u}_d. \tag{2.18}$$

m_{gas} is the mass of the gas molecule, $v_{th,gas}$ is the thermal velocity of gas molecules, $\vec{u}_d$ is the mean velocity of dust particles relative to the gas. Thus, the neutral friction is proportional to r_d^2.

The Millikan coefficient δ denotes the type of reflection. Eq. (2.18) with $\delta = 1$ is the expression for specular reflections of gas molecules from the particle. Here the molecules colliding with the dust particle with their velocity components perpendicular to the dust particle surface are reversed after collision. $\delta = 1 + 4/9$ expresses the regime of perfect diffuse reflections, when the molecules are absorbed and re-emitted by the surface of the dust particle. They are emitted with a semi-isotropic Maxwellian distribution at the dust particle temperature. The δ value depends on the mass ratio of gas molecules and surface molecules, on the gas and surface temperature and on the adsorption energy [100, 118, 119]. At the pressure of 50-110 Pa the δ values were experimentally found to be 1.28±0.01 , which is in agreement with other measurements [117, 120] and corresponds to the regime with diffuse reflections.

In the case of ideal gas $n_{gas} = p/(kT_n)$ Eq. (2.18) can be written as

$$\vec{F}_{Nd} = -m_d\beta_E\vec{u}_d \tag{2.19}$$

with the Epstein coefficient

$$\beta_E = \delta\frac{8}{\pi}\frac{p}{\rho_d r_d v_{th,gas}}, \tag{2.20}$$

where p is the gas pressure, and $m_d = (4/3)\pi r_d^3\rho_d$ is the mass of the dust particle.

Thermophoretic force

The thermophoretic force is of crucial importance for the formation of Yukawa balls. This force arises due to the gradient of the neutral gas temperature. In this case, the momentum exchange rate during collisions between gas molecules and the dust particle is larger for the hotter side of the particle. Thus, there is a net moment transfer from the ambient gas to the particle. The absolute value of the thermophoretic force is proportional to the temperature gradient. The force is directed from the region of higher temperature to the region of lower temperature (opposite to the temperature gradient). An analytical expression for the thermophoretic force [121] is given by

$$\vec{F}_{th} = -\frac{32}{15}\frac{r_d^2}{v_{th,gas}}\left[1 + \frac{5\pi}{32}(1 - \alpha)\right]k_T\nabla T_{gas}, \tag{2.21}$$

where k_T is the translational thermal conductivity of the gas and T_{gas} is the gas temperature. Thus, the thermophoretic force is proportional to r_d^2 like the neutral drag force.

A reasonable approximation for the accommodation coefficient is $\alpha \approx 1$ [121] if the gas and the dust particle surface temperatures is less than 500K. If the pressure is high enough this expression does not depend on the gas pressure. Both these conditions are met in typical experiments.

Ion drag

An ion drag force arises due to momentum exchange between the streaming positive ions and the dust particle. The streaming motion arises due to ambipolar diffusion or in strong electric fields in the sheath. This force has a significant influence on the particle in laboratory plasmas in regions where the ion flux is large. It can play a significant role if the discharge power is large enough [42, 48, 122–125].

The total ion drag force (F_{id}) on a grain is the sum of two contributions: the collection (or absorption or direct) force, F_{coll} and the orbital (Coulomb or indirect) force, F_{orb}. The collection force is contributed by those ions which collide with the dust grain and transfer their momentum (see Fig. 2.7). The orbital force is due to ions which exert a momentum on the dust through Coulomb collisions, i.e. the deflection of ion trajectories in the field of the dust.

The discussion concerning a quantitative description of the orbital force was dealt with by many researchers [47–49, 84, 99, 100, 119, 123], but still a complete theory or model for computation of orbital force over the full range of collisionality is not existing. The most widely used are the approach of Barnes et. al [47] and a recent model of Khrapak et. al [48]. Some of the models are described briefly hereunder. Recently, there is much attention given to quantify this force [126, 127]. In the present work, we also try to compute the ion drag force for a collisional plasma background existing in rf discharges.

2.6   Analytical models and Experiments for ion drag
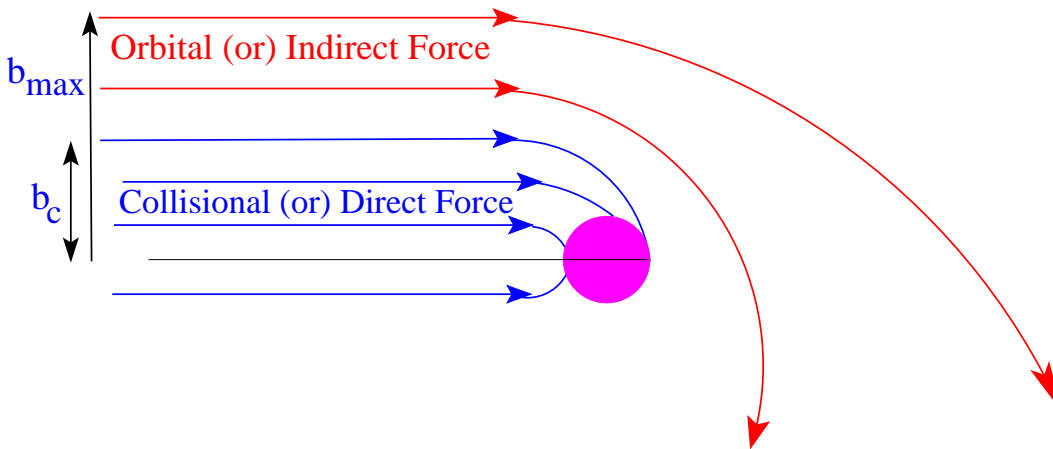
Figure 2.7: Different contributions for the ion drag force.

The problem of Coulomb collisions was first dealt with by Chandrasekhar [128] to study stellar collisions. Here, a point-like central object was considered taking not into account the finite size of the central object (dust particle) and hence not accounts for the collection ion drag contribution. This model was modified for the dusty plasma case [2, 40–43, 47–49].

The orbital drag force for a point-like object can be calculated due to those ions which are deflected in the electric field of the dust.

$$F_{orb} = momentum\ transfer\ \times\ flux\ \times\ orbital\ cross\ section \tag{2.22}$$

In reality, the range of Coulomb field is infinite which will result in infinite orbital (or Coulomb) collision cross section. But, to obtain a finite orbital collision cross section, the integration is truncated at some value of the impact parameter, the so-called "cut-off" distance, beyond which the collisions are considered to be of negligible contribution. Usually, this truncation length is the Debye length λ_D. Then, the orbital cross section is given by

$$\sigma_{orb} = 4\pi b_{\pi/2}^2 \ln \frac{b_{max}}{b_{\pi/2}} = 4\pi b_{\pi/2}^2 \ln \frac{\lambda_D}{b_{\pi/2}} \tag{2.23}$$

where $b_{\pi/2} = e^2/(4\pi\epsilon_0 m_i v_i^2)$ is the impact factor for 90° deflection. Then the orbital ion drag contribution is given by

$$F_{orb} = m_i v_s n_i v_f \sigma_{orb} = m_i v_s n_i v_f 4\pi b_{\pi/2}^2 \ln \frac{\lambda_D}{b_{\pi/2}} \tag{2.24}$$

Here $v_s = (v_f^2 + v_{ti}^2)^{1/2}$ is the mean velocity. n_i is the unperturbed ion density, v_{ti} is the ion thermal velocity, v_f is the ion flow velocity.

Barnes Model

Barnes et al. [47] derived an expression for the ion drag force including the finite size of the dust particle and hence also the collection contribution. The collection contribution is given by the ions which are responsible for the charging, given by (using the OML ion current to the grain)

$$F_{coll} = momentum\ transfer\ \times\ flux\ \times\ collection\ cross\ section \tag{2.25}$$

$$= m_i v_s n_i v_f \pi b_c^2 = m_i v_s n_i v_f \pi r_d^2 \left(1 - \frac{2e\phi_p}{m_i v_s^2}\right) \tag{2.26}$$

where ϕ_p is the floating dust potential and b_c is the collection impact parameter. All the ions within b_c collide the central object (see OML charging).

Barnes also corrected the above Coulomb cross section for finite-size dust, where it was proposed that the minimum collision impact parameter should be taken as

collection impact parameter (b_c). So, here the Coulomb collision cross section was integrated between b_c and λ_D, resulting in the orbital drag force:

$$F_{orb} = m_i v_s n_i v_f 4\pi b_{\pi/2}^2 \ln \left(\frac{\lambda_D^2 + b_{\pi/2}^2}{b_c^2 + b_{\pi/2}^2} \right)^{1/2} \tag{2.27}$$

Hence, in this model only Coulomb collisions within one Debye length λ_D are considered. Also, it is not clear which Debye length has to be used, the electron or the ion Debye length. Usually the electron Debye length is used, but this is subject to a large number of discussions.

Khrapak Work

Khrapak and coworkers [2, 48, 49] have provided improved expressions for the Coulomb logarithm for finite size dust grains with a Yukawa potential (shielding) and considering collisions outside the Debye sphere. Here, the Coulomb collision cross section is obtained by using for the upper impact parameter cut-off, the orbit whose closest approach to the dust is equal to the Debye length (in order to include collisions outside the Debye sphere). Here, the orbital drag force is given by

$$F_{orb} = m_i v_s n_i v_f 4\pi b_{\pi/2}^2 \ln \left(\frac{\lambda_D(v) + b_{\pi/2}}{r_d + b_{\pi/2}} \right) \tag{2.28}$$

Hutchinson Work

Hutchinson, et.al. [40–43] performed extensive computational studies using the SCEP-TIC PIC code to compute currents to the dust grain and the ion drag on grains for the full range of dust sizes and Debye lengths for collisionless plasma backgrounds. Only ion trajectories are followed while electrons are treated as background with Boltzmann density. From the computed ion currents and the potential distribution around the grain, the collection and orbital ion drag forces have been computed on a virtual spherical region around the dust. This work delivered ion drag forces as a function of ion drift velocities.

Further, they proposed analytical fits to their numerical results, which are based on OML currents considering into ion drift. There, the collection contribution to the

drag force is given by

$$F_{coll} = n_i r_d^2 m_i v_{ti}^2 \frac{\sqrt{\pi}}{2} \tag{2.29}$$

$$\left[u \left(2u^2 + 1 + 2\chi \right) e^{-u^2} + \left[4u^4 + 4u^2 - 1 - 2 \left(1 - 2u^2 \right) \chi \right] \frac{\sqrt{\pi}}{2} \ \text{erf}(u) \right] / u^2$$

where $u = v_f/v_{ti}$ is the normalized flow velocity and $\chi = -Ze\phi_p/T_i$ is the normalized floating dust potential. The terms in the parenthesis account for the ion drift. The orbital drag force is given by

$$F_{orb} = n_i \ \frac{q_i^2 \phi_p^2}{m_i v_{ti}^2} \ r_d^2 \ 8\pi \ G(u) \ \ln \Lambda \tag{2.30}$$

with the Chandrasekhar function G(u), which includes the effect of finite flow velocities, given by

$$G(u) = \frac{\left[\text{erf}(u) - 2ue^{-u^2}/\sqrt{\pi} \right]}{2u^2} \tag{2.31}$$

and Coulomb logarithm $\ln \Lambda$ given by

$$\ln \ \Lambda = \ln \left[\frac{b_{90} + \lambda_s}{b_{90} + r_d} \right] \tag{2.32}$$

and impact factor for 90° deflection is given by

$$b_{90} = \frac{r_d Ze\phi_p}{m_i v_{\text{eff}}^2} \tag{2.33}$$

and the adopted form of effective shielding length and effective velocities are given by

$$\lambda_s^2 = \frac{\lambda_{De}^2}{1 + \frac{2ZT_e}{m_i v_{\text{eff}}^2}} + r_d^2 \tag{2.34}$$

and

$$m_i v_{\text{eff}}^2 = 2T_i + m_i v_f^2 \left(1 + \left[\frac{v_f/\sqrt{ZT_e/m_i}}{0.6 + 0.05 \ \ln(m_i/Z) + (\lambda_{De}/5r_d) \left(\sqrt{T_i/ZT_e} - 0.1 \right)} \right]^3 \right) \tag{2.35}$$

T_i is the ion temperature, T_e is the electron temperature and $q_i (=Ze)$ is the ion charge.

Experimental methods to derive ion drag

Experimental techniques to derive the ion drag force are only relatively few. The works include laboratory experiments [123–125, 129–131] and experiments under microgravity [31, 132].

- The dust particle trajectories are analyzed to derive the ion drag force from the force balance equation [31, 123, 129, 131, 132].

  In experiments under microgravity [31, 123, 129], a focused laser beam is moved in a controlled way to drive particles in the extended dust cloud and at the void boundary. From the observed particle motion together with Langmuir probe measurements, the forces on the particles in the dust cloud and at the void boundary are derived. Then from the force balance equation between the inward electric field force and the outward ion drag, the ion drag is derived. The derived ion drag is compared with Barnes, Khrapak and Hutchinson's models and some deviations are found with Barnes model.

  In [131], hollow glass microspheres are dropped into the plasma and allowed to fall due to gravity. The ion drag force was derived from the particle trajectory deflection from the vertical direction.

- In Yaroshenko et al. work [124, 125], the ion drag force is derived from two experimentally determined quantities: the particle drift velocity and the electric field. This method does not require a priory knowledge of the particle charge, but uses the charge gradient determined from the same experiment.

Discussion of the ion drag models

The above theoretical and computational works mainly deal with a collisionless plasma background, where the mean free path (mfp) of collisions is very large compared to the Debye length. Very recently, Hutchinson and coworkers [44, 127] as well as Khrapak and coworkers [126, 133–137] have further extended their investigations to compute the ion flux and drag on the grain in collisional environments.

Khrapak et al. showed analytically that the force acting on a small absorbing grain in a collision-dominated plasma with slowly drifting ions can decrease substantially in comparison with the force acting on a nonabsorbing body. In addition, their work [137] constitutes investigation of the effect of plasma production and losses on the ion drag

force. The results show that for a nonabsorbing grain the ion drag force is positive, i.e., it acts along the direction of the ion drift independently of the loss mechanisms; The magnitude of the ion drag force is unaffected by plasma production for weak ionization rate and reduces strongly for high ionization rates. For an absorbing grain, the ion drag force is negative for low ionization rate and reverses its direction for high ionization rate. However, these drag computations are for a highly collisional (hydrodynamic) background.

Hutchinson et al. computed the ion drag force on a spherical dust over the entire range of charge-exchange collisionality. It has been shown that the ion drag force shows a local maximum where the CX collision mean free path is smaller than the effective shielding length ($\lambda_{mfp} \leq \lambda_s$) and reaches a limiting value at high collisionality.

A general agreement between experiment and calculations has been obtained, but direct quantitative comparisons are lacking, also because precise measurements for a detailed comparison are not available so far. Additionally it is known that in low-temperature laboratory rf plasmas, the distributions are non-Maxwellian [45, 46]. Further, the dust potential is asymmetric in the sheath region due to streaming ions.

Hence, to quantify the ion drag force under experimental conditions, it is important to self-consistently quantify the plasma background, the electron distribution functions, the dust charge, the dust potential and the potential distribution around the dust grain. Kinetic particle simulations are suitable tools for such studies, as they are able to resolve the trajectories of all plasma species in the dust field.

2.7   Dust structures

Depending on the strength of interaction between charged particles, plasmas can be divided into ideal or weakly-coupled and non-ideal or strongly-coupled plasmas. The strength of interaction is represented by the coupling parameter Γ, which is the ratio between the mean potential energy (E_{pot}) of Coulomb interaction between two charges Q_1 and Q_2 and the thermal energy E_{kin},

$$\Gamma = \frac{E_{pot}}{E_{kin}} = \frac{1}{4\pi\epsilon_0} \frac{Q_1 Q_2}{\overline{r_{12}}} \cdot \frac{1}{kT}, \tag{2.36}$$

where $\overline{r_{12}}$ is the mean distance between the particles. For ideal or weakly coupled plasmas $\Gamma \ll 1$, and plasma components can be treated as an ideal gas. Most of the ordinary plasmas in space and laboratory are weakly coupled. The system of

charged particles is said to be strongly coupled when the electrostatic interaction energy between the particles exceeds their thermal energy ($\Gamma \gtrsim 1$). Due to the large charges of dust particles the interparticle interaction energy is also large. Thus, even the crystallization (at $\Gamma \gg 1$) in the dust particle system becomes possible. The particles in such systems are trapped by an external harmonic potential. Such ordered finite systems are called *dust clusters* in contrast to ordered expanded dust systems, which are called *dust crystals*.

Experimentally, two-dimensional ordered systems of dust particles were first discovered in 1994 in a cathode sheath of a radio-frequency discharge, where strong upward sheath electric fields compensate gravity, and the particle levitation is possible [23–26]. Because of this force balance the particles arrange in a horizontally extended 2D structure. Under an additional horizontal confinement the particles arrange in 2D finite clusters (see Fig. 2.8). Later, dust crystals were found in a thermal plasma at normal pressure [138], in a positive glow gap of a dc discharge, and in nuclearly excited dusty plasmas [139].
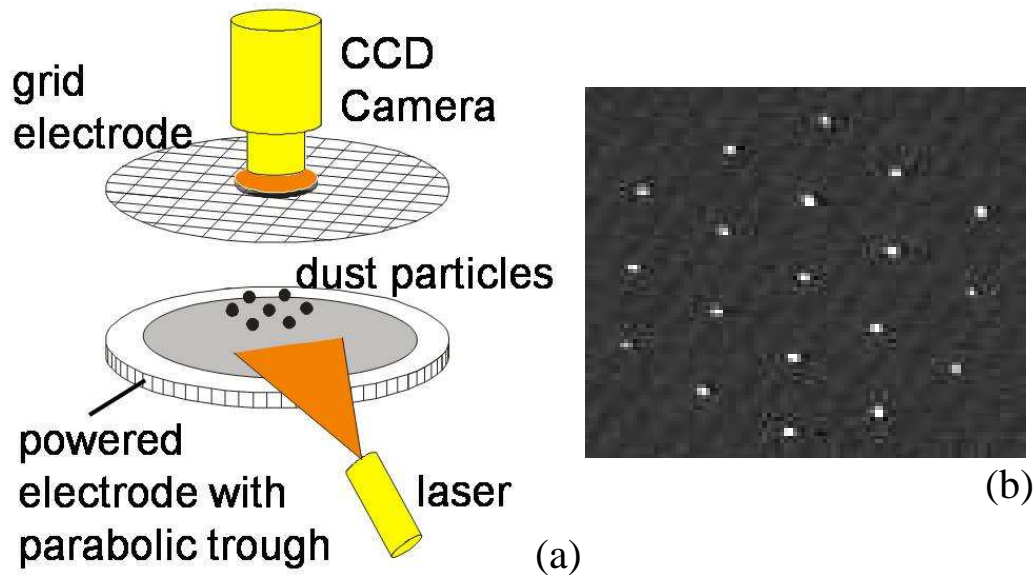
Figure 2.8: (a) Schematic picture of a two-dimensional dust crystal experiment [26], and (b) A typical 2D dust crystal.

Three-dimensional dust clusters and crystals are much more difficult to realize in the lab due to the huge gravity force acting on dust particles. Due to this reason 3D dust crystal experiments had to be made under microgravity conditions on board of a space station [140] or during the plane parabolic flights [141].

In 2004 the spherically 3D dust clusters, so-called Yukawa balls, were first experimentally observed in dusty plasmas under laboratory conditions [108, 109]. The confinement of Yukawa balls is obtained from a superposition of various forces acting on dust particles. There, a glass box is placed on the powered rf electrode (see Fig. 2.9). The lateral Yukawa ball confinement is attributed to the horizontal component of the plasma-induced electric force. This force acts on the negatively charged particles towards the center of the glass box and thus confines negatively charged dust particles in the glass box center. The vertical Yukawa ball confinement is due to the compensation of gravity. An upward thermophoretic force was applied by heating the powered electrode. The ion drag force was shown to be negligible [108, 109]. The upward thermophoresis pushes the dust particles into the plasma bulk. The thermophoretic force is supported by additional electric forces, which result from surface charges on the glass walls. Thus, superposition of gravity, the plasma induced electric force, and the thermophoretic forces models the Yukawa ball trap which was found to be harmonic in 3D [109].
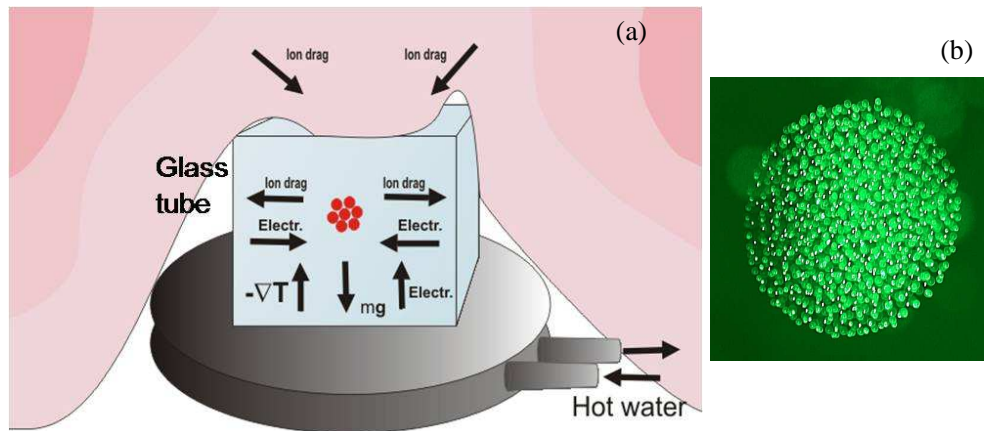
Figure 2.9: (a) Schematic picture of three-dimensional Yukawa ball formation and force balance [109] and (b) A typical Yukawa ball

The parabolic flight experiments or experiments on the International Space Station show [141], however, that under microgravity other forces like the ion drag become important, that lead to the formation of large dust-free areas in the center of the plasma discharge as shown in Fig. 2.10.

Hence, it can be seen that dust parameters like dust charge, floating potential and dust potential distribution are very important for dust structure formation. Hence, computing these parameters for actual discharge conditions is necessary to characterize the system, which is the goal of this thesis.

electrode

electrode
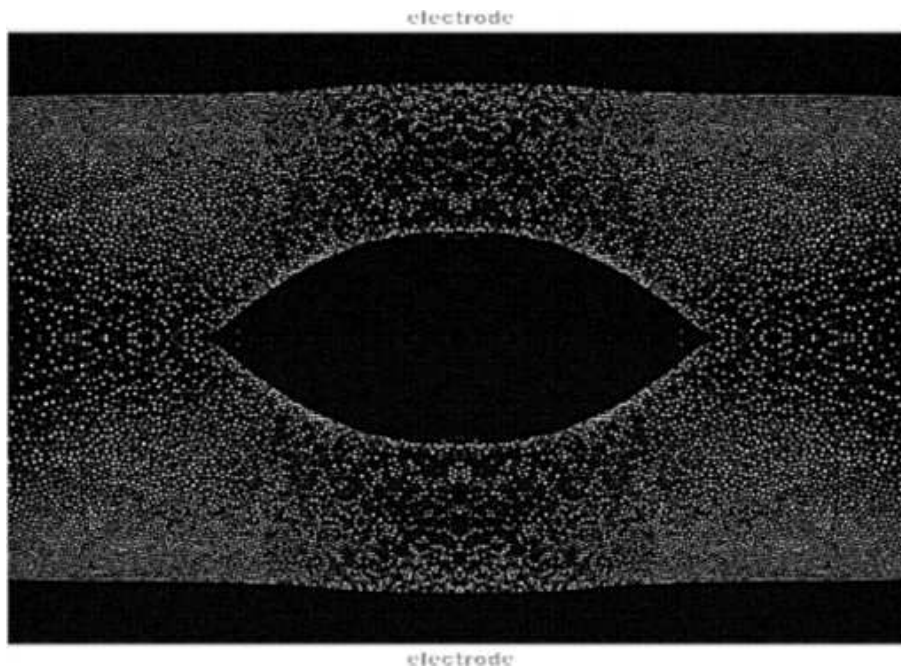
Figure 2.10: Typical appearance of a dust-free void in microgravity experiments [141].

The basic elements of dusty plasmas, charging of dust, forces acting on the dust in a plasma have been introduced. Before discussing the computational results, the computational tool used for this thesis will be introduced in the next chapter.

Chapter 3

P^3M code

In this chapter, the computational tool used for the simulation of multicomponent reactive rf discharges and for dust charging process is described. As already mentioned in the previous chapter, these are low temperature plasmas with low ionization. The fluid approximation [142] or fluid codes cannot be used to study such plasmas, as the fluid description is valid only when plasma particles have a Maxwellian velocity distribution, and plasma parameters are not changing much on the mean free path length. But in the case of low temperature plasmas, due to the strong potential drop in the sheath, distribution functions of both ions and electrons are non-Maxwellian [61, 143]. Hence, a kinetic approach with the particle-in-cell (PIC) method [144, 145] is suitable for the study of such plasmas. One-dimensional Particle-in-Cell (1D PIC) simulations were performed for multicomponent reactive plasmas in order to study the effect of an ion extractor system on ion energy distributions (IEDs) [see appendix A]. A three-dimensional Particle-Particle-Particle-Mesh (3D P^3M) code was applied for studying the dust charging and the ion drag force on single and multiple static and dynamic dust grains immersed in rf discharges. These codes have been obtained from K. Matyash and modifications have been done for dust parameter diagnostics. For a detailed description of the code, one can refer to [46, 146, 147]. Here a brief description of the PIC method, its limitations in estimating charging dynamics and the P^3M method is provided. The modifications and additions done to the codes will be presented later.

3.1 PIC method

In the PIC method, one follows the kinetics of 'Super Particles' (each of them representing many real particles), moving in self-consistent fields (electric and magnetic) calculated on the grid according to the Maxwell equations. In this work, only electrostatic calculations are done and therefore only the Poisson equation is solved. 'Super particles' are simulated because the number of charged real particles in systems of interest is usually very large (10^{12}) and not possible to simulate even on the fastest computers. The particle collisions are handled by Monte-Carlo collision (MCC) routines, which randomly change particle velocities according to the actual collision dynamics. Hence, these codes are also called PIC-MCC codes.
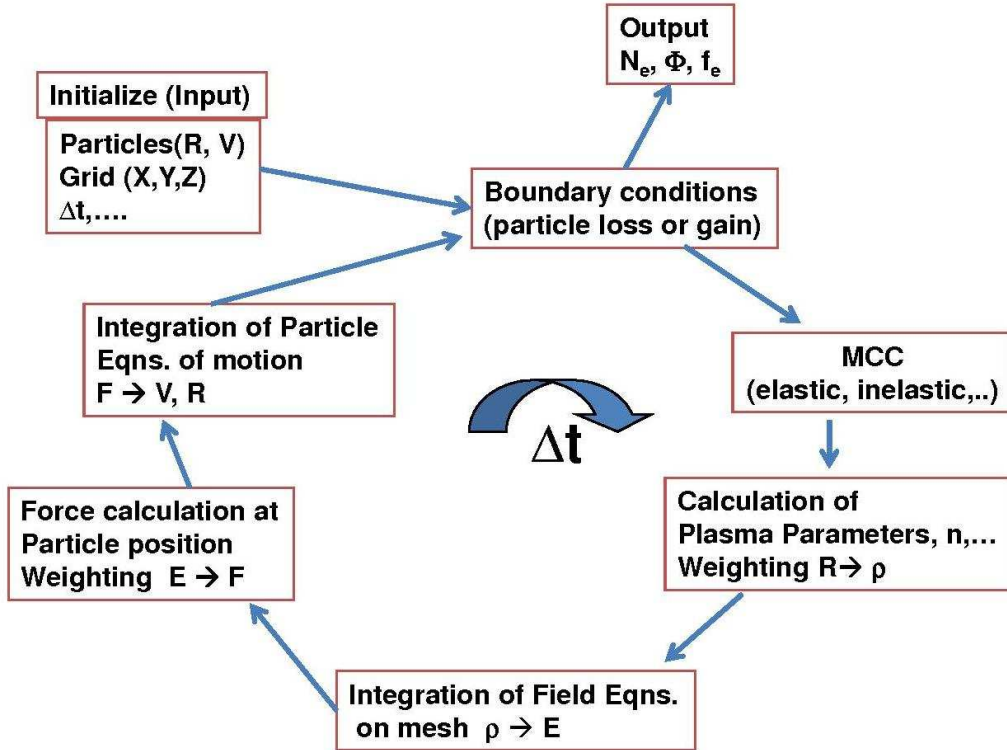
Figure 3.1: Computational algorithm in a typical PIC-MCC code.

The computational algorithm of the PIC scheme is presented in the Fig. 3.1. Main steps involved in the computation are the following:

(i) Compute the approximate plasma characteristics of the system.

- $\lambda_{De} = \sqrt{\epsilon_0 k_B T_e / n_e e^2}$, similarly λ_{Di}, mean free paths.

- $\omega_{pe} = \sqrt{n_e e^2 / \epsilon_0 m_e}$

(ii) Prepare a computation grid in the physical system with grid width $\Delta x \leq \lambda_{De}$. Usually $\Delta x = 0.5\lambda_{De}$ is used.

(iii) Initiate the plasma species (electrons, ions, neutrals) in the grid.

(iv) From the particle positions in the neighboring cells of a grid point, charge and current densities are computed at the grid point, using extrapolation techniques.

Usual extrapolation methods used are Nearest Grid Point (NGP) method, Cloud-in-Cell (CIC) method, etc. [144]. NGP weighting scheme is relatively noisy and introduces artificial forces (self-forces) to the solution [147]. In our simulations the CIC weighting method is used, in which charged particles are treated as rigid 'clouds' of uniform density with dimensions equal to grid width in all directions and can freely move through each other.

(v) In electrostatic problems, the Poisson equation is solved on the grid to update fields at the grid locations from the charge densities. $\nabla^2 \phi = -\rho/\epsilon_0$

For three-dimensional simulations, the Poisson equation is discretized on the grid using a 7-point finite-difference scheme [148]. The resulting sparse system of linear equations is solved using the LU-decomposition method [149]. For this purpose the SuperLU software library [150] is used. Then, the components of the electric field on the grid are calculated with a centered difference scheme:

$$
\begin{aligned}
(E_x)_{k,m,n} &= (\phi_{k-1,m,n} - \phi_{k+1,m,n})/2\Delta x \\
(E_y)_{k,m,n} &= (\phi_{k,m-1,n} - \phi_{k,m+1,n})/2\Delta y \\
(E_z)_{k,m,n} &= (\phi_{k,m,n-1} - \phi_{k,m,n+1})/2\Delta z
\end{aligned}
$$

(vi) Grid field values are used to compute field values at the particle positions using the same weighting techniques. The same weighting scheme is used to ensure momentum conservation.

(vii) With these field values, particles are moved according to the equations of motion.

$$
m_{i,e} \frac{dv_{i,e}}{dt} = q_{i,e} E_{i,e} \tag{3.1}
$$

$$
\frac{dr_{i,e}}{dt} = v_{i,e}; \quad r = x, y, z \tag{3.2}
$$

(viii) Boundary conditions are implemented. For absorbing boundaries particles are absorbed or lost and for periodic boundaries particles leaving from one side are introduced from the opposite side.

 (ix) Collisions are implemented and the resultant plasma species (electrons, ions, neutrals) are updated.

Collisions play a very important role in the formation and the sustaining of rf discharges. Details of how collisions have been implemented in the code are described in [148]. In the present code, following collisions have been implemented.

- electron-electron Coulomb collisions

- electron-ion Coulomb collisions

- ion-ion Coulomb collisions

- electron-neutral elastic collisions

- ion-neutral elastic collisions

- electron-neutral ionization collisions

- electron-neutral, electron-ion dissociation collisions

- dissociation with ionization collisions

- dissociation with electron-recombination collisions

- charge-exchange collisions

- excitation collisions

Coulomb collisions between charged particles are important for transport processes in plasmas. The electron-electron Coulomb collisions play a key role in populating the high-energy tails of electron distributions, pushing the distribution function towards Maxwellian. The high energy electrons, despite their relatively small number, strongly influence the properties of the whole system, because only electrons from the high energy tail of the distribution can participate in electron-impact ionization collisions with neutrals. In bounded plasmas the flux of very high energy electrons to the wall is responsible for compensation of ion current and formation of a sheath potential structure. Ion-neutral collisions in the bulk or the sheath determine the ion energy distributions (IEDs) and ion angular distributions (IADs). In the codes used, a binary Coulomb collision model described in [146, 151] has been implemented.

(x) Neutral particles can be updated or can be treated as a fixed background with constant density and temperature, as its density is much higher than the densities of charged species.

(xi) Steps (iii)-(ix) are repeated over prescribed timestep (Δt). Usually for accuracy of the differencing scheme [144], we use $\Delta t = 0.2/\omega_{pe}$. Due to higher masses ion equations are integrated over a bigger timestep than Δt, usually a few tens bigger timestep.

3.2 Limitations of PIC
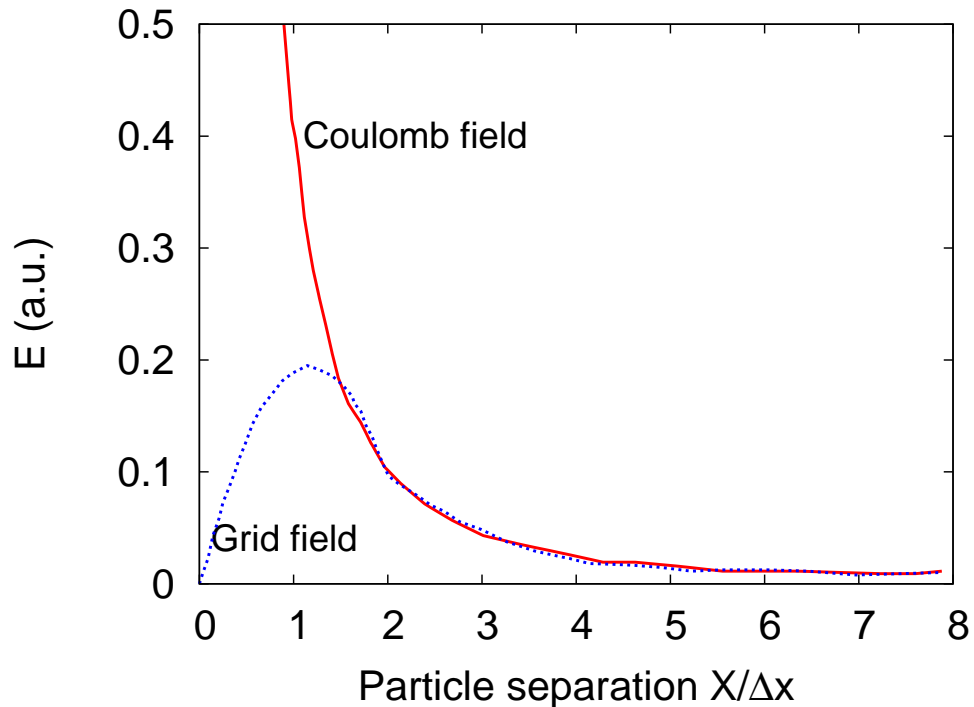
Figure 3.2: Interaction force from grid field between two charged particles in PIC model compared to the "right" Coulomb field [152].

The conventional PIC-MCC code can describe the details of rf plasmas including the sheath in front of the electrodes. This code has previously been extensively used for studying the formation of dust structures in low temperature laboratory plasmas, where originally a constant dust charge was prescribed [146]. But, the PIC-MCC can not handle the charging dynamics of a micron-size dust. It is because of the draw-

back in a conventional PIC method that the spatial resolution is limited by the size of the grid which is typically of the order of the Debye length, which is a fraction of a millimeter for rf plasmas. Whereas the size of the dust grains used in the laboratory experiments is much smaller than this, i.e. in micrometer-nanometer range. As mentioned in the previous section, due to the CIC weighting method, the particles in the conventional PIC algorithm which are represented by charged clouds of the grid size, can penetrate each other [146, 147, 152]. This leads to high inaccuracy for interparticle interaction when the distance becomes smaller than the cell size [152]. Fig. 3.2 shows the dependence of the interparticle interaction force on the distance, where the distance is normalized to the cell size, as calculated with the PIC model. The interaction force from the grid field strongly deviates from the Coulomb force for small distances and tends to go to zero as the inter-particle distance decreases. Therefore, the PIC model, being able to resolve long-range interaction between the particles (of the order of the Debye length), misses the close-range part for distances comparable with the radius of the dust grains.

One approach to overcome this is to use a PIC-MC particle collision operator [153] for describing plasma species absorption at the dust with the collision cross-section obtained from analytic OML [3] theory. This model is sufficiently fast, but can fail when plasma is strongly nonunifrom and/or non-Maxwellian. Another approach is to resolve or follow in an MD algorithm ion trajectories around dust until they are absorbed or scattered [41, 42, 152, 154]. The present simulations are based on the latter approach.

3.3 P^3M code

In order to accurately resolve close-range interactions between dust grains and plasma particles, the PIC model was combined with a molecular dynamic (MD) algorithm. In the resulting Particle-Particle Particle-Mesh (P^3M) model, the long-range interaction of the dust grains with charged particles of the background plasma is treated according to the PIC formalism. For particles which are closer to the dust grain than a Debye length their interaction force is computed according to a direct particle-particle MD scheme using the exact electrostatic potential. This is implemented in the following way: in the computational domain, the cell in which the dust grain is located together with the neighboring cells form the "MD" region as shown in Fig. 3.3. All particles

outside the MD region are treated according to the conventional PIC scheme. For plasma particles (electrons and ions) inside the MD region the electric field is calculated as: $E = E_{grid} + E_{dust}$. For the calculation of the grid field E_{grid}, the charge density as in the PIC part is used from which the dust grain contribution is subtracted. The dust contribution is accounted for by the exact Coulomb electric field E_{dust} calculated pairwise between the dust and the plasma particles. In order to resolve the particle motion on scales of the order of the dust grain size, particles in the MD region are moved with a smaller time step (t_{MD}). Usually $t_{MD} = \Delta t(r_d/\Delta x)$. Typical PIC time step (Δt) is about 1.1×10^{-10} sec and $\Delta x = 200$ μm. Hence for a 1 μm dust particle, t_{MD} is about 6×10^{-13} sec. Plasma particles which cross the computational dust grain boundary are assumed to be absorbed. The dust grain charge is updated each MD time step. This approach allows to follow the charged particles trajectories in the vicinity of the dust grain and by this to include finite-size effects for dust grains, self-consistently resolving the dust grain charging due to the absorption of plasma electrons and ions. The P^3M code is parallelized using the MPICH library. The computational algorithm in the P^3M code is shown in Fig. 3.4, where shaded boxes show the modifications for studying the dust charging with additional MD region.
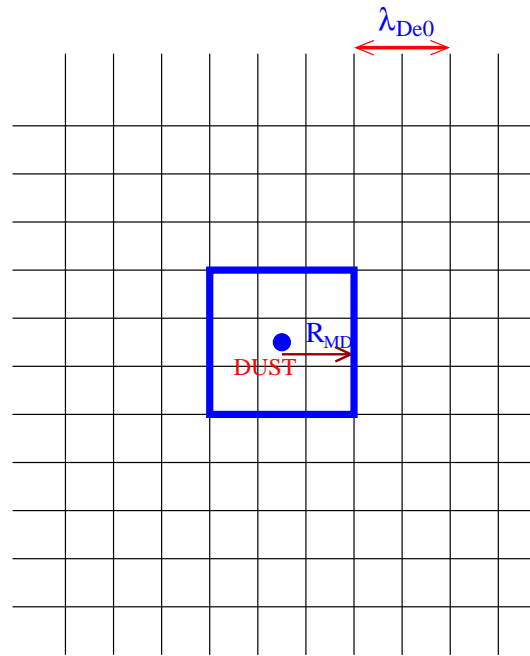
Figure 3.3: Schematic diagram showing MD region around the dust grain.

The additional computation in P^3M code includes the following:
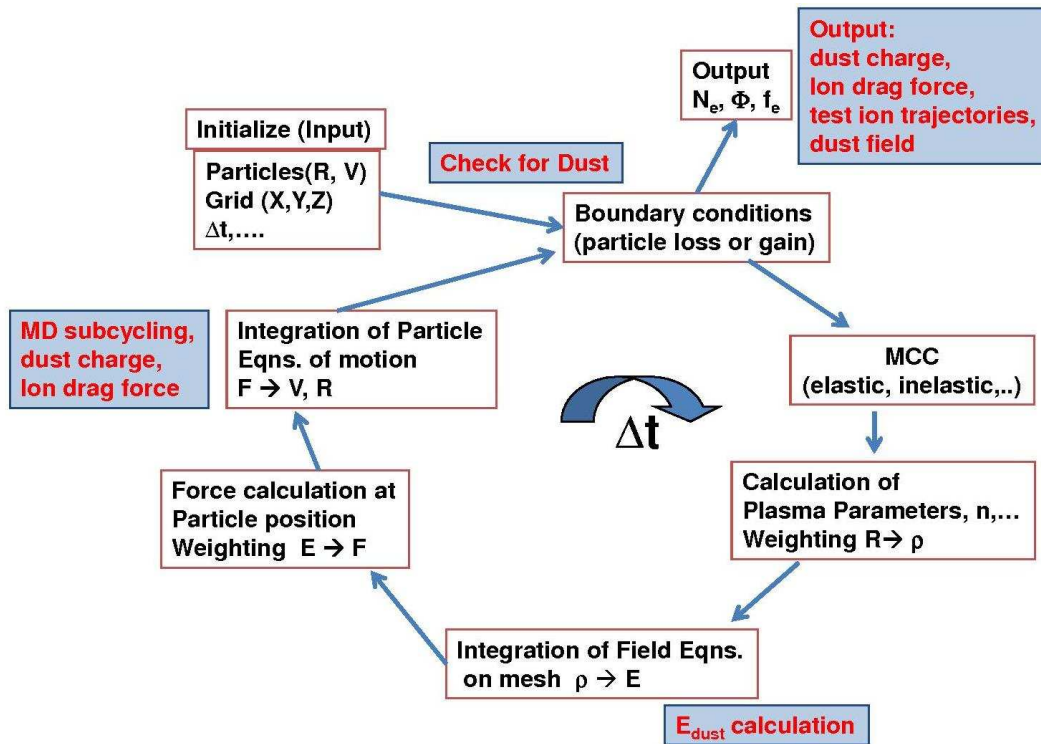
Figure 3.4: Computational algorithm in a typical P^3M code.

- Checking for the existence of the dust particles. If particles exist, determine the MD region boundaries around the dust.

- Determine the MD subcycling timestep depending on the ratio of dust size to grid width.

- Determine the dust density at grid locations from the dust particle positions.

- Compute the grid field due to dust (E_{dust}).

- For each MD subcycle push the plasma species (electrons and ions) and check for their absorption at dust or crossing the MD boundary. If plasma species are colliding with the numerical dust boundary count them and update the dust charge (see chapter 5).

- Compute the collection ion drag force from ions colliding with the dust and orbital drag force from all other ions in the MD region (see chapter 6 for details).

- Output the dust parameters: dust charge, ion drag force, electric field around the dust to derive the dust floating potential and potential distribution.

- Any other diagnostics, such as test ion trajectories.

Till now, the basic elements in dusty plasmas and the P^3M code have been introduced. In later chapters, the computational results for charge and ion drag on single and multiple dust particles located in rf discharges are presented. Before studying the dust charging, first the characteristics of the rf discharge which govern dust charging are studied and these properties are presented in the next chapter.

Chapter 4

Plasma discharge characteristics

Discharge properties, such as plasma species densities and velocity distributions, govern the charging process of the dust grain. The dust charge itself determines the dust potential and field around the dust, which again influences the shielding and ion drag force. Therefore, the presence of dust will modify the local discharge characteristics. Hence, it is necessary to study the discharge characteristics to gain an insight into the charging processes. The characteristics of rf discharges have been experimentally and theoretically studied by many researchers [32, 45, 46, 84, 148, 155]. Here, we present the computed rf discharge characteristics and recapitulate the physics of them.

4.1   Method of computation

We have applied the P^3M model (only PIC-MCC modules are employed and sufficient) to build-up the rf discharge plasma in argon, after equilibration of which the dust grains are immersed to study charging and drag forces. The parameters of the simulation were chosen to represent the conditions of the experiments with Yukawa balls (see Ref. [109]). As background gas, argon with pressure p = 50 Pa and neutral gas temperature T = 300 K was used.

The computational domain representing the rf discharges is shown in Fig. 4.1. The discharge system dimensions are taken as 0.15 cm×2.4 cm×0.15 cm. The plasma volume is divided into 8×128×8 computational cells (see Ref. [152] for selection criteria for cell-widths and time-step). The electrodes are aligned in the XZ-plane and the electrode separation is 2.4 cm. The lower electrode at Y = 0 cm is grounded and the upper electrode at Y = 2.4 cm is powered with a sinusoidal voltage at frequency f_{rf} =
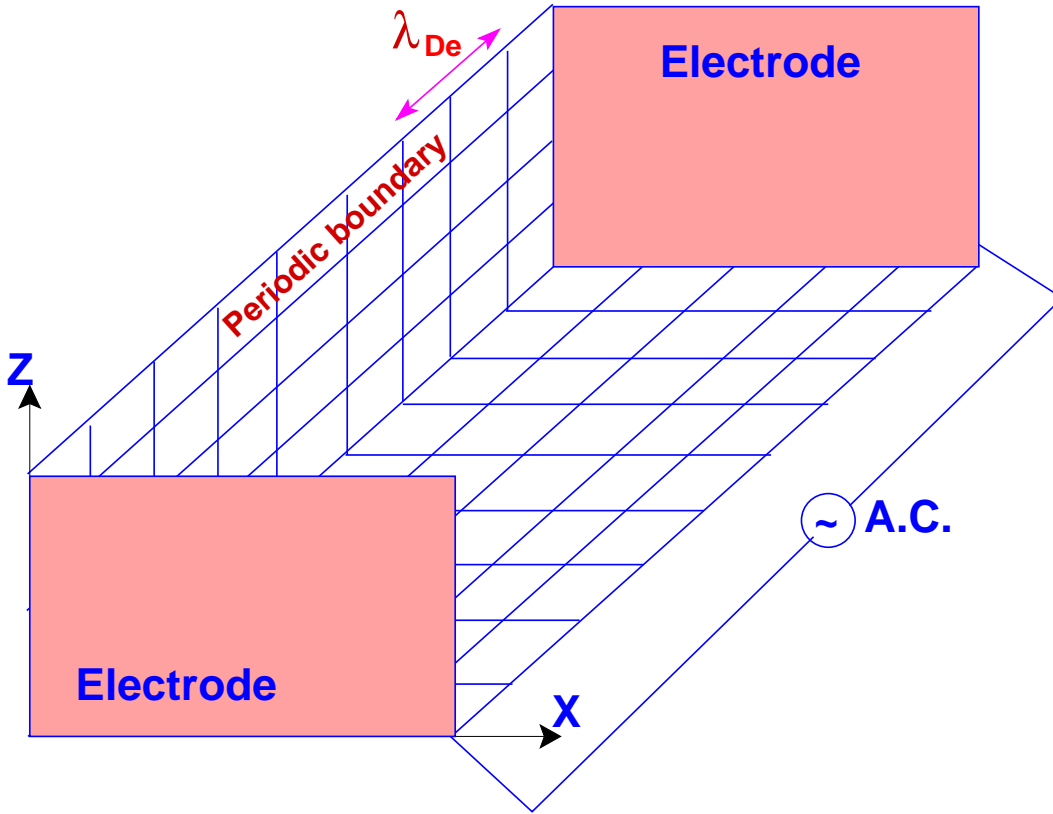
Figure 4.1: Schematic of 3D computational grid for simulation of rf discharges.

13.56 MHz and amplitude $U_{rf} = 30$ V or 50 V. At the electrodes absorbing wall bound-
ary conditions for the particles are applied. At boundaries in the X and Z directions
periodic boundary conditions are used, both for particles and potential. The neutral
argon was treated as a fixed background with constant density and temperature, as its
density is much higher than the densities of charged species. Only the charged particle
dynamics was followed. In the simulation, the plasma was sustained self-consistently
due to electron impact ionization of the neutral gas by the electrons accelerated in the
applied rf voltage.

In the present P^3M code, a binary Coulomb collision model described in [146, 151]
has been implemented. Coulomb collisions between charged species, electron-impact
ionization, efficient excitation, electron-argon elastic collisions and momentum transfer
charge-exchange collisions were taken into account in the simulation. The collisions
implemented for current study are listed in Table 4.1.

Table 4.1: List of collisions included in the current simulations

Collision	Reference
e-e, e-ion, ion-ion Coulomb	[156]
e-Ar Elastic Collision	[157]
Ar^+ - Ar Elastic Collisions	[157]
Ionization : $e + Ar \rightarrow Ar^+ + 2e$	[157]
Charge-exchange : $Ar + Ar^+ \rightarrow Ar^+ + Ar$	[157]
Excitation : $e + Ar \rightarrow Ar^* + e$	[157]

4.2   Results

Here, we present the characteristics of the rf discharges after equilibration.

Potential and Density
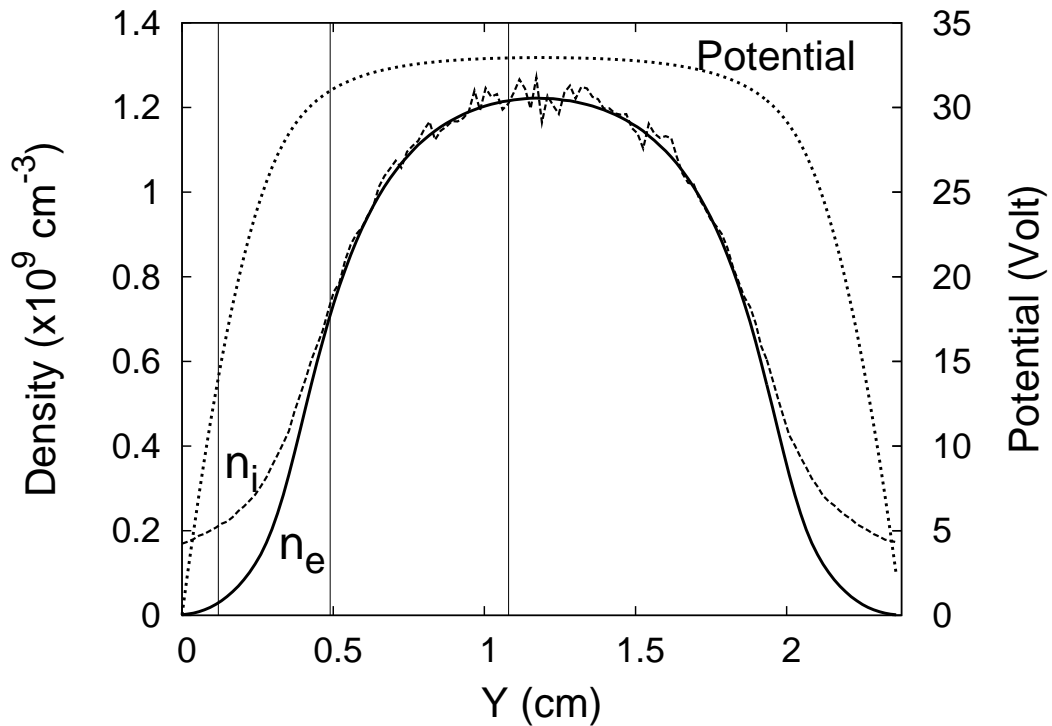
Figure 4.2: Time-averaged density and potential profiles. Vertical lines represent the y-coordinates of the dust.

Figure 4.2 shows the computed electron and ion densities in a rf discharge between the electrodes on the central axis, for a pressure of p = 50 Pa. The ion density equals the electron density in the bulk satisfying quasi-neutrality and exceeds the electron density in the sheaths. After equilibration, the bulk plasma parameters are n_e=1.22 × 10^9 cm^{-3} and T_e = 5.5 eV respectively, yielding an effective electron Debye-length λ_d=550 μm. Similarly, the effective ion Debye-length is $\approx$ 37 μm ($T_i/T_e \cong 0.0045$), which is one order smaller than the electron Debye-length. Fig. 4.2 also shows the time-averaged plasma potential between electrodes. A steep potential drop occurs near the electrodes within oscillating positive space-charge layers (in rf sheaths). The electric field in the bulk plasma is negligible in comparison with the field in the sheaths. This strong electric field in the rf sheath regions is directed toward the electrodes, preventing electrons from leaving the plasma for most of the rf cycle. The electrons are able to escape to electrodes only during a short time, when the rf sheath collapses. From the deviation from quasineutrality, the sheath width can approximately be derived to be about 0.5 cm. As ion plasma frequency is smaller than the rf frequency (due to high mass), ions are not able to react to the fast changing rf electric field. Thus ions respond only to the averaged electric field. Thus, the flux of energetic ions, accelerated in the sheath electric field to energies of about average sheath potential drop, constantly flows to the electrodes. The electrons respond to the instantaneous electric field and oscillate between the electrodes in the static background of the positive space charge of the ions. In the sheath regions the positive space charge of the ions during most of the rf period remains uncompensated because the electrons reach the electrode only for a short time, during the collapse of the sheath potential, to balance the ion current on the wall. The change of the net space charge near the electrode during the rf cycle, resulting from the different response of ions and electrons to the applied rf voltage, is responsible for the dynamics of the rf sheath electric field.

Electron distributions

The time-averaged electron energy probability function [32] at the center of the discharge is shown in Fig. 4.3. It can be seen that the electron distribution is non-Maxwellian, and rather Druyvesteyn-like [45, 46, 146] where a strong drop of high-energy electrons is observed. Similar electron distributions were experimentally found in low-pressure capacitive rf discharges [45]. Such electron distribution in the discharge indicates the Ohmic heating [45, 146] in a Ramsauer gas like argon. The mean free
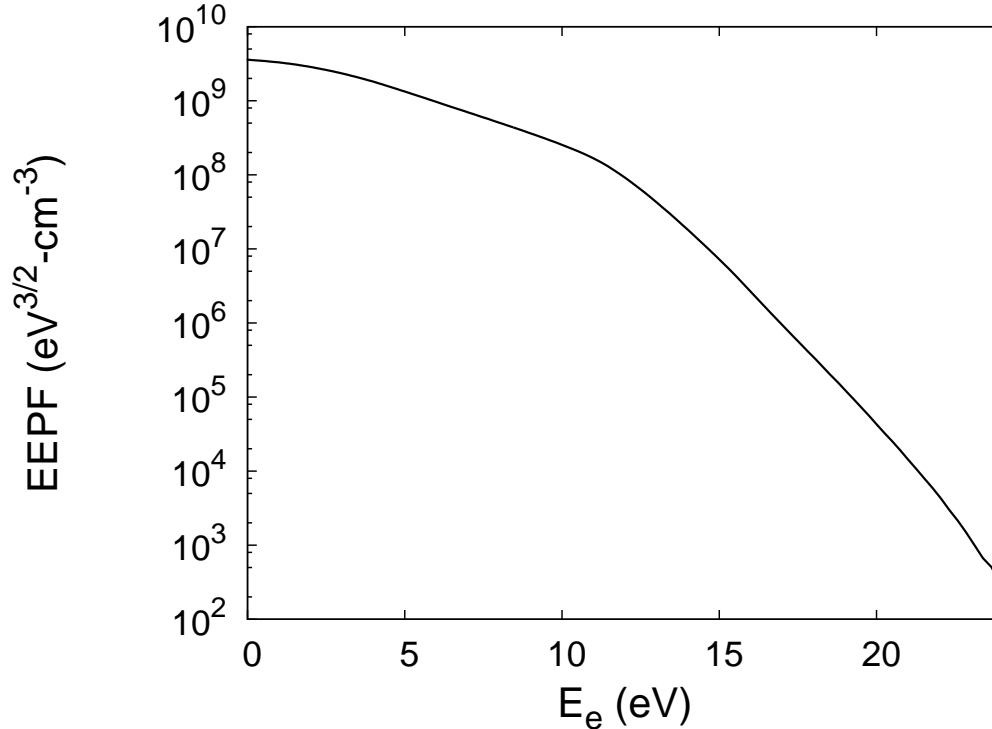
Figure 4.3: Time-averaged electron energy probability function

path of electron-neutral elastic collisions is ~ 0.08 cm, which is much smaller than the system length 2.4 cm and also smaller then the sheath width 0.5 cm. Thus, the Ohmic heating in the sheath region, when the electrons are accelerated in the strong electric field between successive elastic collisions with neutrals, is the mechanism of electron heating.

The deviation of electron distribution from the Maxwell distribution could have important consequences on dust charging. Due to the absence of high energy electrons compared to Maxwellian distribution, the electron flux to the dust is small when compared to the Maxwellian distribution case, which can result in smaller dust charge numbers and smaller floating dust potentials. This issue will be addressed in detail in chapter 5, where we compare the computed dust charges with the theoretical models which use Maxwellian distribution for electrons.

Ion distributions

Figure 4.4 shows the time-averaged Ion Velocity Distribution Function (IVDF) between the electrodes at the center of the discharge. In the bulk, the ions stay cold where their
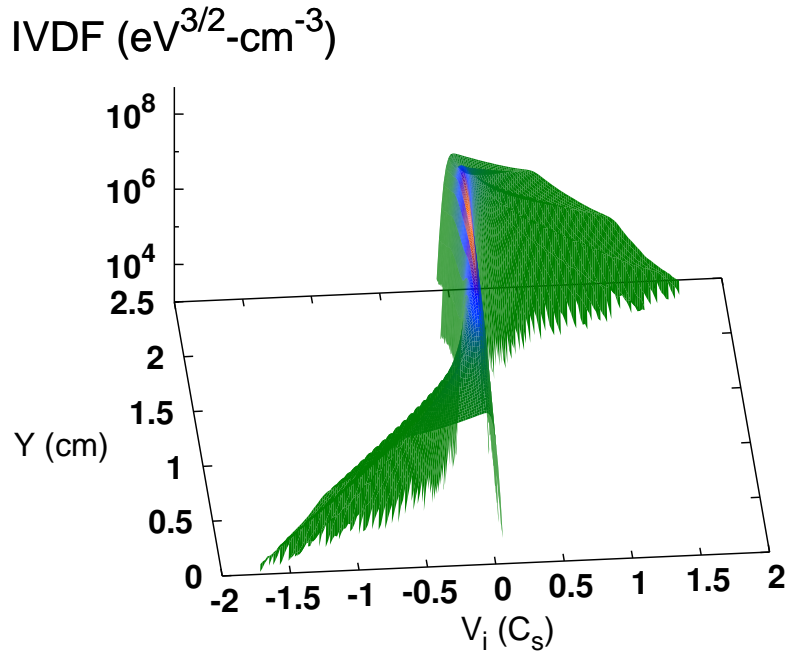
Figure 4.4: Time-averaged ion velocity distribution function along the discharge axis Y.

mean energy of random motion is close to the thermal energy of the background gas. In the sheath regions low-energy ions from the bulk plasma are sharply accelerated in the strong electric field toward the electrodes.

Figure 4.5 shows the time-averaged ion velocity (normalized to local sound speed) between the electrodes. It can be seen that ions are subsonic even in the sheath, except very close to the electrode. The approximate value of v_i/c_s near the sheath edge is 0.12. Ions are not accelerated to Bohm velocity near the plasma-sheath edge. This is due to the collisions in the system. The mean free path of ion-neutral charge-exchange collisions (λ_{mfp}) is only about 85 micron, which is less than the sheath width. Thus, this is a highly collisional sheath.

Now to summarize, the plasma discharge characteristics and various length scales are listed in the Table 4.2.

Plasma species distributions at low pressures

The rf discharge characteristics at very low pressures (a few Pa) differ very much from the above discussed. We have done simulations to study ion energy distributions
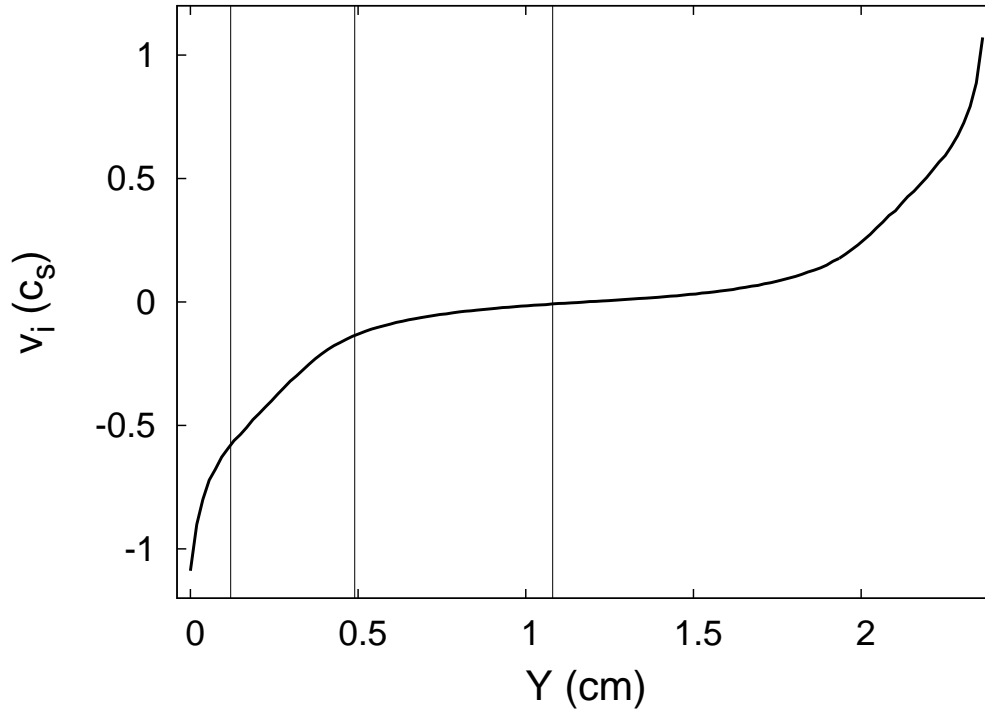
Figure 4.5: Time-averaged ion mach number (v_i/c_s) along the discharge axis Y. Vertical lines represent the y-coordinates of the dust.

(IEDs) at electrodes at pressures of 2-5 Pa in Ar/CH_4 gaseous mixture (please refer to the appendix for details). We also studied the effect of ion extraction system on IEDs. Hence, for the sake of comparison we list the differences in the characteristics of rf discharges at high and low pressures.

At low pressures of a few Pa,

- **Predominant heating mechanism is the Stochastic heating.** In the EVDF, there exist two groups of electrons: Cold electrons in the center of the discharge, and the tail of high-energy electrons oscillating between the electrodes. The electrons from the low energy group are not energetic enough to overcome the ambipolar potential barrier and penetrate the sheath region. Thus they are locked in the center of the discharge. The energy of these electrons is far below the energy threshold for the majority of inelastic collision processes, thus they are not participating in collisions with neutrals, except for elastic scattering. Eventually, due to elastic collisions, these electrons diffuse to the sheath region. This group of electrons is most likely populated by the low-energy secondary electrons, produced in electron- neutral ionization collisions. Unlike the electrons from the

Table 4.2: rf discharge characteristics and various length scales for p=50 Pa, U_{rf}=50 V.

Bulk electron density	1.22×10^9 cm^{-3}
Bulk electron temperature	5.5 eV
Bulk ion temperature	0.025 eV
Electron Debye length	550 μm
Ion Debye length	37 μm
System length along discharge	2.4 cm
Sheath width	0.5 cm
mfp of CX collision	85 μm
mfp of electron-neutral elastic collision	0.08 cm

low-temperature group, the electrons from the high-energy tail can easily over-come the ambipolar potential barrier and penetrate into the region of strong electric field in the sheath. These electrons oscillate between the rf sheaths, get-ting reflected from them by the strong retarding electric field. Although during single reflection from the sheath, an electron can both gain and loose energy, de-pending on the phase of the rf field, but on average, electrons are accelerated due to stochastization of their motion, similar to the Fermi acceleration mechanism [32].

- The electron distribution is biMaxwellian, i.e., it is a sum of two Maxwellian distributions with different temperatures. The low temperature part corresponds to the static group of cold electrons in the bulk region, whereas the high- tem-perature component is contributed by the energetic electrons, oscillating between sheaths. [45, 158, 159].

- Ion energy distributions resemble the high pressure case, i.e., in the bulk the ions stay cold and into the sheaths the ions are accelerated upto average sheath potential drop.

4.3   Summary

rf discharges have been simulated using a three-dimensional PIC-MCC code for the discharge conditions relevant to the dusty plasma experiments. After equilibration

of the rf discharges, its characteristics, including species density, potential, species distribution functions have been studied. From the mean free path analysis, the system is collisional, charge-exchange collisions between ions and neutrals being dominant. Electron and ion distributions are non-Maxwellian, electrons behave Druyvesteyn-like and ions are subsonic even in the sheath due to charge exchange collisions.

After fully understanding the characteristics of the rf discharges, now the dust particles are located at various positions in the discharge to address the issues of charging mentioned. The results will be presented in the next chapters.

Chapter 5

Charging of single dust particles

5.1 Introduction

The dust grain attains a charge (positive or negative) due to various charging mechanisms [6], such as absorption of electrons, ions, secondary electron emission, etc. Charging of a dust grain is determined by the background plasma properties, where collisions between various plasma species play an important role. The dust charge governs the electrostatic potential around the dust and interdust grain interaction and hence the formation of dust structures. Also the ion drag force - the force exerted on dust grain by traversing ions around the dust due to coulomb interaction - which plays a crucial role in phenomena such as wake-field formation in rf sheaths [28] and dust void formation in microgravity dusty plasma experiments [31], depends on the dust potential and dust charge. So, in order to quantify these various properties for realistic discharge conditions in rf discharges, dust charge and potential have to be determined accurately. Since in rf discharges the plasma bulk and sheath have different properties (e.g. streaming of ions), the dust charge and potential might vary for dust grains located at different positions in rf discharge.

The analytical theories of charging described in chapter 2 do not account for streaming ions leading to difficulties in determining the charge of dust located in the sheath. Also, they assume Maxwellian distributions for the plasma species, which is not shown to be true in the chapter 4 and also in [45, 46]. Kinetic simulations are suitable tools for charging studies for realistic experimental conditions. The present work is an extension of work by K. Matyash [152, 160] to obtain more insight into collisional effects on the dust charging and shielding in rf discharges. In this work, we present the dust

parameters computed for a single static spherical dust grain located at different positions in an rf discharge. We compare the simulation results with existing charging models. The dust potential distribution is compared with the Debye-Hückel potential, as it is widely used in the dusty plasma community.

5.2   Method of computation

We have applied the P^3M model to investigate the dust grain charging process in a capacitive rf discharge in argon. The parameters of the simulation were chosen to represent the conditions of the experiments with Yukawa balls (see Ref. [109]). As background gas, argon with pressure p = 50 Pa and neutral gas temperature T = 300 K was used.
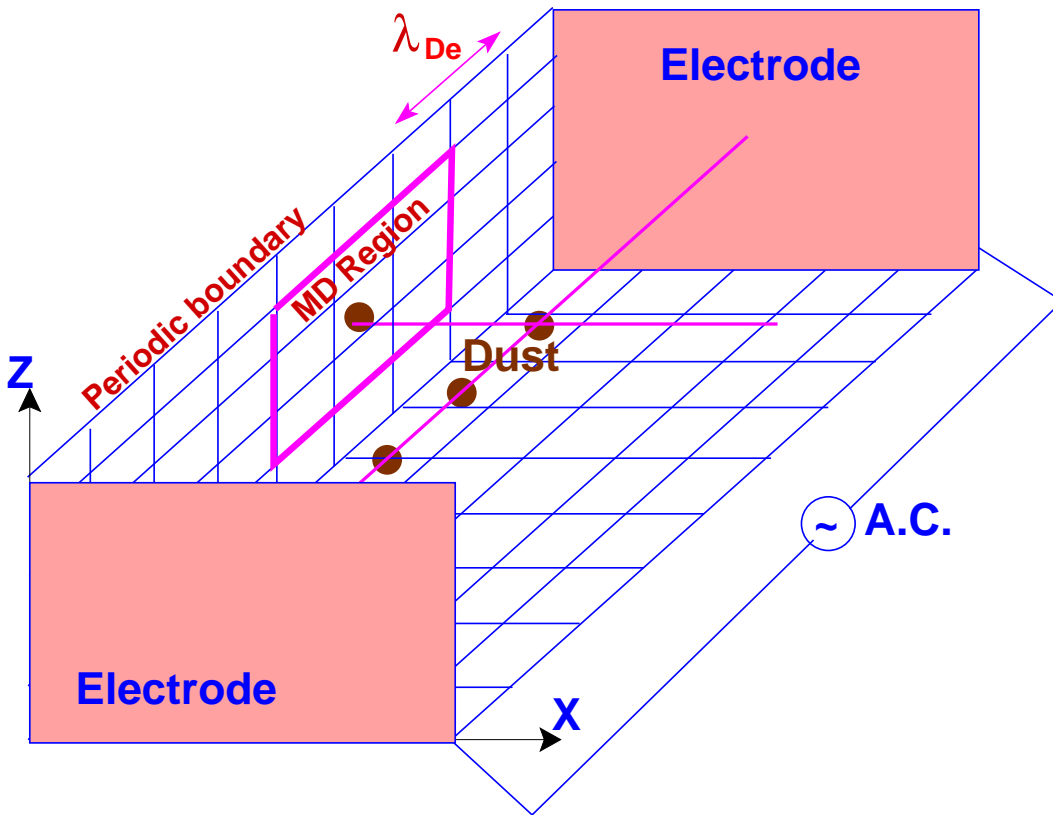
Figure 5.1: Schematic of 3D computational grid for simulation of dust in rf discharges. The MD region (cube) of the central dust particle is projected onto the left wall.

The computational domain representing the rf discharges and dust locations is shown in Fig. 5.1. The computational domain and boundary conditions are similar to

the ones described in the previous chapter. Dust particles with radii $R_d = 2.5, 5.0, 7.5$ and 10.0 μm were introduced into the discharge with zero starting charge. The position of the dust particles was fixed at three different positions of y = 0.12, 0.49 and 1.08 cm, which correspond to locations in sheath, presheath and bulk regions respectively (in x,z the particles are centered in the simulation domain). The cell in which the dust grain is located together with the neighboring cells form the "MD" region, as shown in Fig. 5.1.

Plasma particles which cross the computational dust grain boundary are assumed to be absorbed. The absorbed plasma species are counted to obtain the dust charge. Other charging processes, such as secondary electron emission, or surface photo emission, have not been considered. In our model, the dust potential is computed independent of the dust charge. It is derived from the computed electric field around the dust. From this field, the potential is derived by integration.

5.3   Results

Here, we present the simulation results for dust parameters (dust charge, potential and potential distribution) computed for static spherical dust grains located at the three positions in the rf discharge. The results will also be compared with theoretical models.

5.3.1   Dust potential

After the background plasma of equilibrated rf discharges has been characterized, we have computed the floating potential on the dust particles of different radii, located at different positions in the rf discharge plasma. Figure 5.2 shows the dust potential along the horizontal/vertical (X/Y) axes for dust particles in the plasma bulk. It can be seen that the floating potential on the dust grain is about -2.98 V and radially symmetric around the dust.

Figure 5.3 shows the dust potential along the horizontal/vertical axes for dust particles in the plasma sheath. In determining the dust potential profile in the sheath, one has to account for the strong change of the plasma potential in the sheath. The potential profile observed in the sheath along X is symmetric, but is asymmetric around the dust along the Y-direction (which is along the electrode separation). This asymmetry is introduced due to the streaming ions in the sheath. The dust potential profile will be analyzed in more detail below.
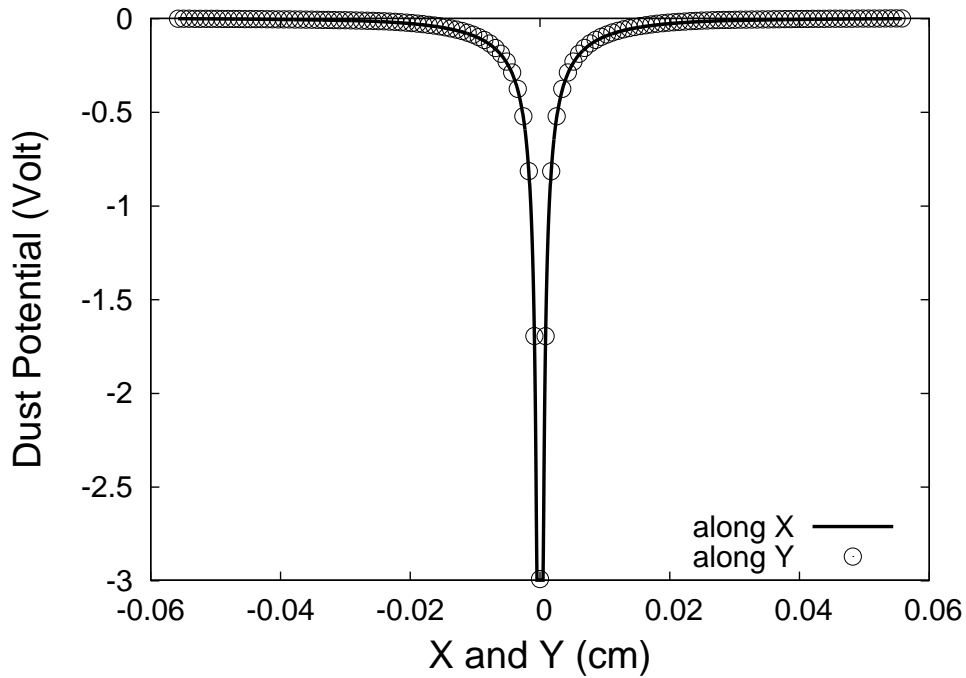
Figure 5.2: Spatial dust potential distribution for a 5 micron dust grain located in the plasma bulk
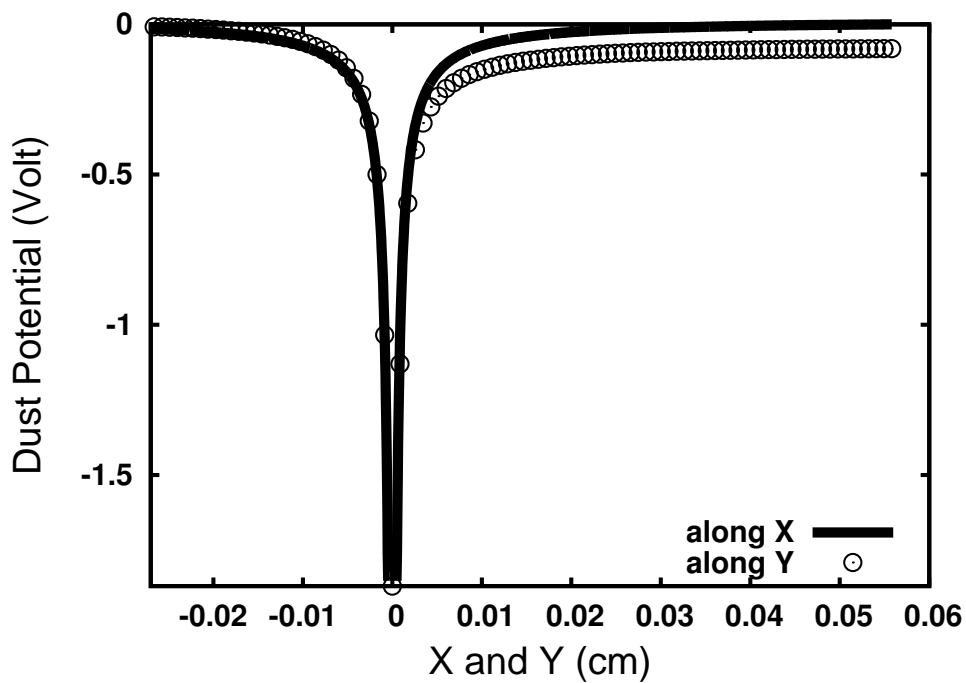
Figure 5.3: Spatial dust potential distribution for a 5 micron dust grain located in the plasma sheath

5.3.2 Dust Potential vs. Dust size & location
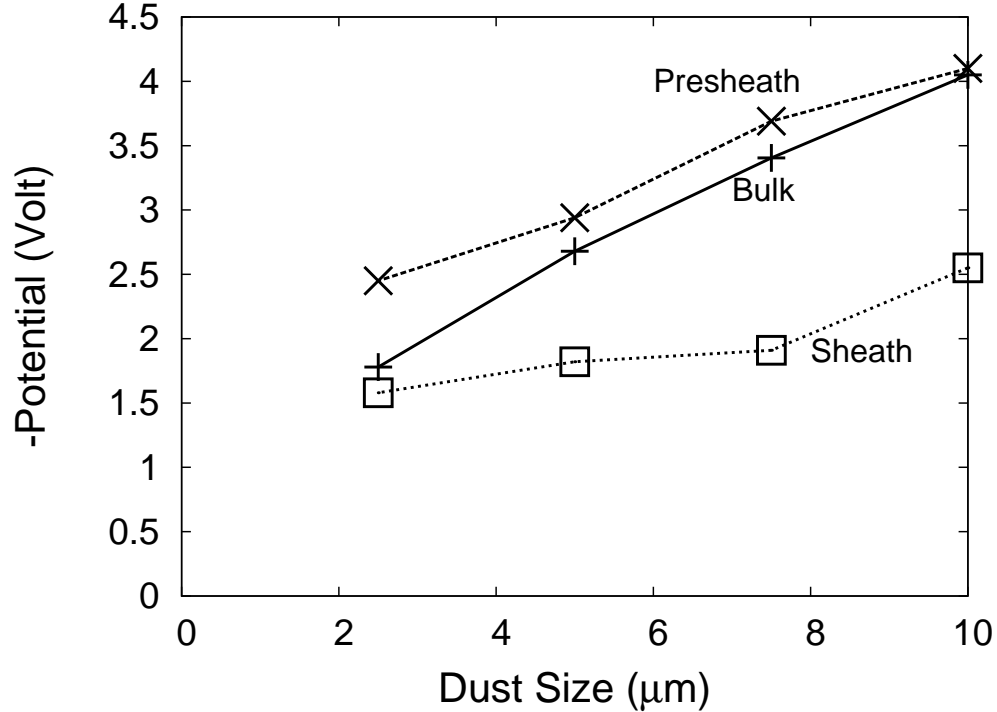
Figure 5.4: Dust potential as a function of dust size

Now the dust potential is analyzed for dust of different sizes (see Fig. 5.4). It can be seen that the dust potential scales nearly linearly with dust size (R_d). As already mentioned, the dust potential is computed by the integration of the dust field around it. From the collisionless models like OML[3], one expects that the dust potential is independent of dust size. But for this collision-dominated plasma, the ion current (I_i) to the dust grain increases (the issue of ion current will be dealt with in detail in the chapter 6), resulting in a size-dependence other than R_d^2 in OML [4, 39]. This collisional ion current contribution results in a dust-size dependence of the dust surface potential. These results qualitatively agree with the simulation results of Zobnin et.al. [4, 39], where a dependence of dust potential on dust size has been demonstrated. There, an additional collisional contribution to the ion current onto the dust grain in a stationary plasma has been obtained by solving the kinetic equation accounting for charge-exchange ion-neutral collisions. Zobnin et.al. derived ion current, surface potential, etc., for intermediate collisionality. For particles with $r_d/\lambda_s \geq T_i/T_e$ the absolute value of the surface potential increases with the particle size linearly. In

our case, for a 5 μm particle $r_d/\lambda_s \approx 0.03$, $T_i/T_e \approx 0.0045$ this condition is fulfilled. Zobnin et.al. [4] also proposed analytical approximations for the ion currents. These analytical formulae show that the ion current is a complex function of collisionality and particle size, resulting in a size-dependence of the surface potential. In Fig. 5.5, dust surface potential for various dust sizes obtained in the present simulations have been compared with the values obtained from the analytical formulae given in [4], for the shielding lengths obtained in our simulations (see below). Both results show the same tendency, but shifted by about 1 volt. This deviation can be attributed to the use of a Maxwellian distribution for electrons in [4], whereas here the distribution is Druyvesteyn-like. The Maxwellian distribution contains more high energy electron population (high energy tail) which contributes additional electron flux to the dust resulting in a more negative dust potential. Hence, dust potential values from Zobnin fit are smaller than the values obtained in our simulations.
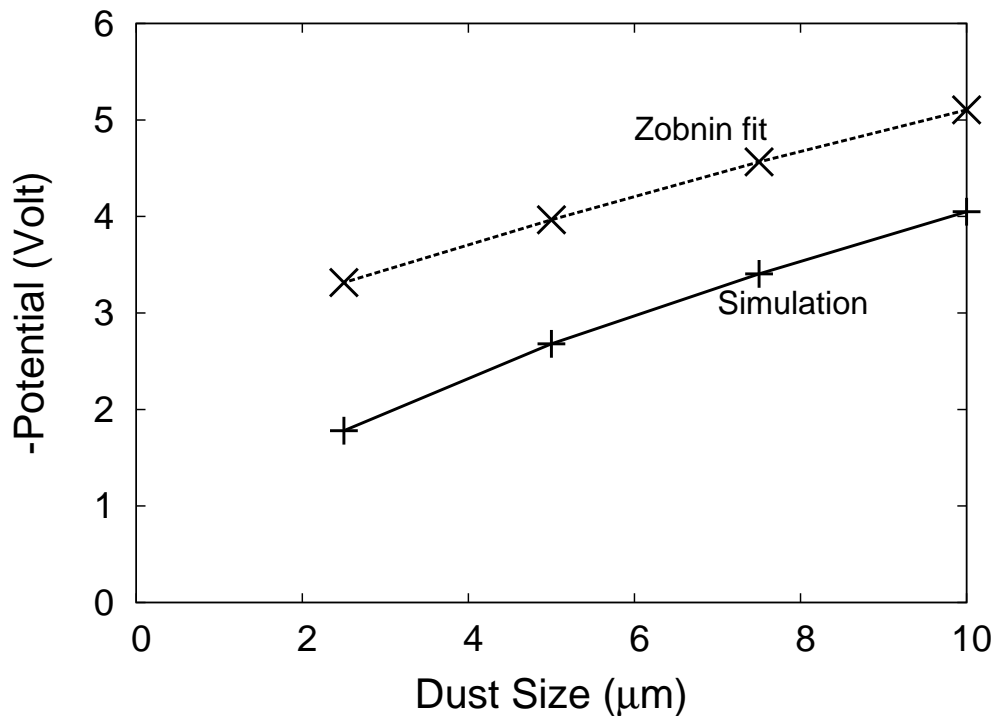
Figure 5.5: Dust size dependence of floating potential (in plasma bulk) determined in our simulations, compared to the analytical fit given by Zobin et.al. [4]

5.3.3 Shielding

We now discuss the dust potential distribution around the dust. The potential around a charge or probe in a plasma is screened or shielded by the plasma particles. It is usually assumed that dust potential screening is a Debye-Hückel (or Yukawa) type. Here, the potential at a distance R from dust is therefore compared to

$$\phi_d(R) = U_d \; \frac{r_d}{R} \; \exp\left(-\frac{R - r_d}{\lambda_s}\right) \tag{5.1}$$

where U_d is the floating potential on the dust. This is an important parameter, which governs the particle interactions. The dust potential around the dust is plotted in units of $\log\left(U_d r_d / R\right)$ versus $(X - r_d)$, as in these units the Yukawa potential is linear. From our kinetic simulations thus the shielding length λ_s is retrieved. Here, only the horizontal X-coordinate is used for this study due to streaming of ions in Y-direction.
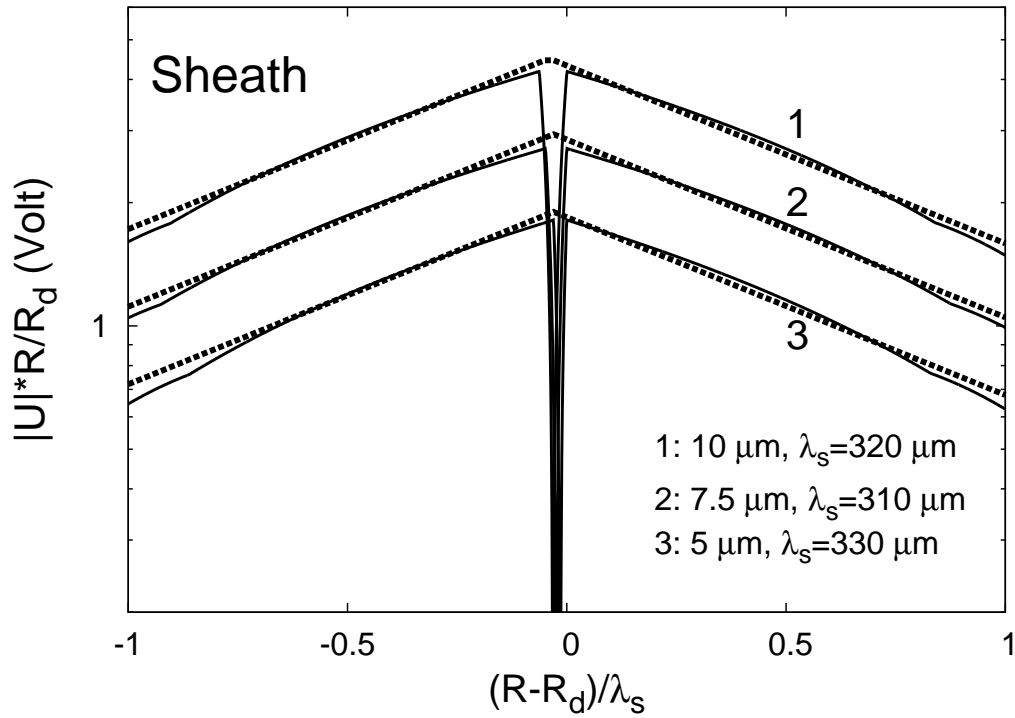
Figure 5.6: Computed dust potential in the sheath compared to the Debye-Hückel potential (dashed line) for various sizes of dust. The resulting screening lengths are also listed.

In Fig. 5.6, the simulated dust potential distributions for various sizes of dust grains located in the sheath are compared to the analytical Debye-Hückel potential. Thus, the dust potential from the P^3M code behaves like a Debye-Hückel potential in a region

close to the dust particle up to a distance $R = \lambda_s$ to $R = 1.5\lambda_s$. Due to finite MD region size, discussion of the long range behavior of the shielding is not possible. Shielding lengths derived for all the cases are about 320 μm. Moreover, the shielding length is found between the electron and the ion Debye lengths. Hence, it can be concluded that the effective shielding is done both by electrons and ions. Deviations of shielding lengths from ion Debye length have already been discussed in [4, 38, 161].
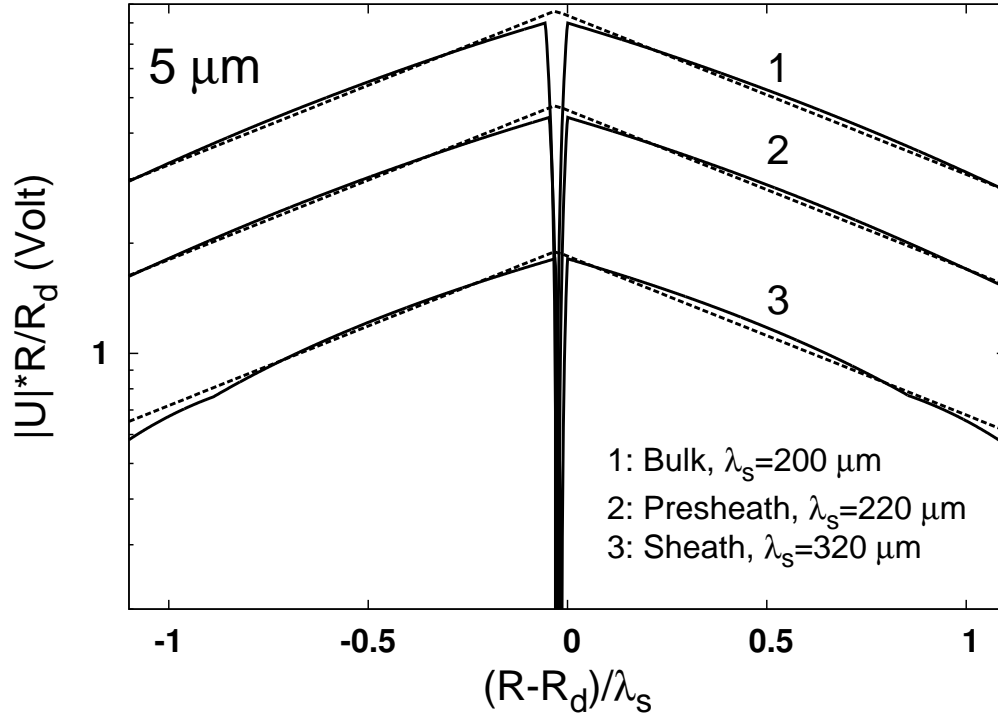
Figure 5.7: Computed dust potential distributions for three dust locations in the discharge compared to the Debye-Hückel potential (dashed line). The resulting screening lengths are also listed.

Figure 5.7 shows the simulated dust potential distributions for 5 μm dust grains located at the three positions in the discharge. In the bulk and the presheath, we find a similar behavior: the potential is Debye-Hückel-like with screening lengths 200 and 220 μm respectively. The screening lengths in the presheath and the sheath are larger than the cell size and are reliable. The screening length in the bulk is comparable to the cell size. However, these values are in agreement with the values of the shielding length which are found to fit the charge and potential calculations in Sec. 5.3.4 very well. From the bulk to the sheath the ion velocities increase and ion shielding becomes increasingly ineffective. Hence, the shielding length slightly increases from the bulk to the sheath.

Physically, the deviation of shielding length in the bulk from the ion Debye length can be attributed to the ion-neutral collisions in the vicinity of absorbing dust grain [50]. The work of Khrapak et al. [50] shows the effect of ion-neutral collisions on the potential distribution. It has been shown that the effect of collisional flux is to extend the potential distribution beyond the ion Debye length indicating an increased shielding length.

5.3.4 Charge evolution on dust

We have also computed the charge on dust particles of different radii, located at the three positions in the rf discharge plasma by counting the plasma particles arriving at the numerical particle boundary.
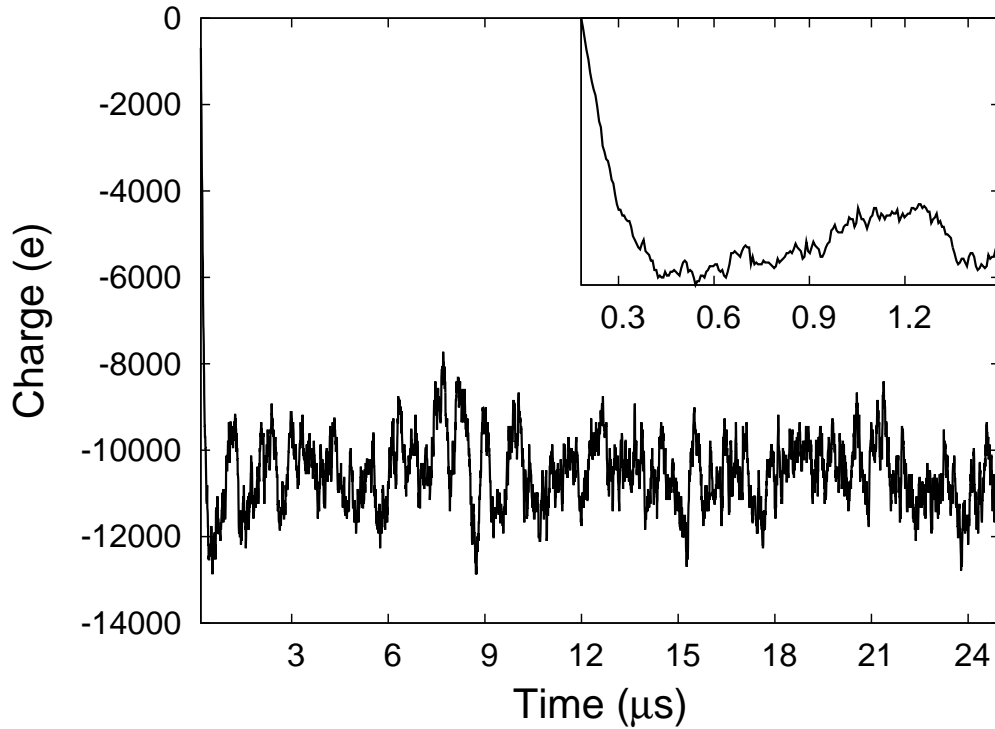
Figure 5.8: Temporal evolution of the dust charge for a 5 micron particle in the bulk. The inlet shows a magnification of the first 1.5 μs of charging.

In Fig. 5.8, we present the evolution of the electric charge of a dust grain with a radius of 5.0 μm located in the plasma bulk. A fast initial charging takes place due to the collection of electrons, while equilibration takes place on the ion time scale (of the order of 0.5 μs in our case)[146, 152]. The equilibrium dust charge is subject

to stochastic fluctuations due to the discrete nature of charge carriers. Stochastic fluctuations have been studied by Cui et. al. [96], and it has been shown that the amplitude of the stochastic fluctuations is approximately equal to $0.5\sqrt{Z_d}$, where Z_d is the equilibrium number of the charges. For the 5.0 μm dust particle case presented here, Q_d=-10482e and so the amplitude of the fluctuations should approximately be equal to 51e. In the simulations, the amplitude of the stochastic fluctuations is approximately equal to 825e. This deviation is due to the fact that in the simulation one computational particle represents 89 real electrons or ions.

Dust Charge vs. Dust size & location
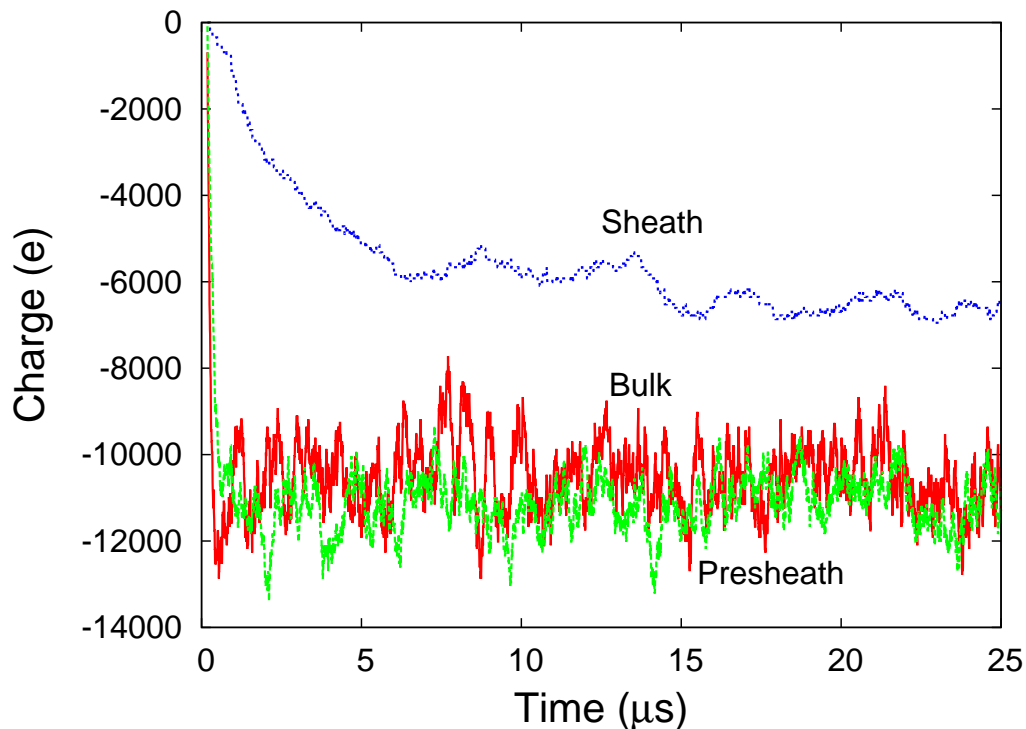
Figure 5.9: Temporal dust charge evolution of a 5 micron particle for different locations

Figure 5.9 shows the charge evolution for a 5.0 micron dust particle located at the three different positions in the discharge. It can be seen that the charge is reduced in the sheath compared to the bulk or presheath value. The charge in the presheath is equal or slightly larger than the bulk value. This can be explained as follows: Charging is due to electron and ion currents to the dust grain. The electron or ion current is

proportional to the density (n), velocity (v) and collection area (σ_d) of a dust grain.

$$I_{e,i} \quad \propto \quad n_{e,i} \; v_{e,i} \; \sigma_{de,i} \qquad\qquad (5.2)$$
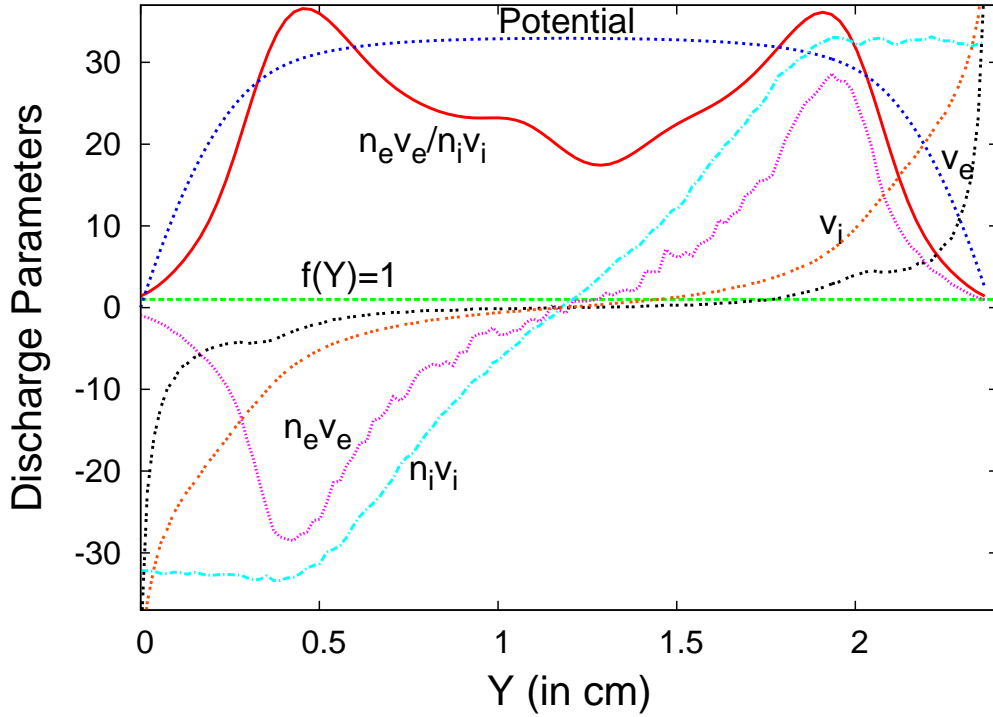
Figure 5.10: Discharge parameters $(v_e, v_i, n_e v_e, n_i v_i$, electron to ion flux ratio, potential) between electrodes. All the parameters are scaled to fit into the scale of flux ratio.

The variation of the dust charge for locations from the bulk to the sheath in a discharge can be explained by analyzing the electron to ion flux-ratio, individual species flux profiles and other discharge parameters along the discharge axis (see Fig. 5.10). The electron (and ion) density decreases from the bulk to the sheath (as shown in Fig. 4.2), whereas the velocities increase. As the ions, due to high inertia, respond to the average electric field, the ion velocity profile (v_i) resembles the time-averaged potential profile, i.e., the ion velocity monotonically increases from the bulk to the sheath. Electrons respond to the instantaneous electric fields, but due to the strong electric field in the sheath directed towards the electrodes prevents electrons from leaving the plasma for most of the rf cycle. The electrons escape to electrodes during a short time, when the rf sheath collapses. Hence, the electron velocity profile does not follow the average potential drop. The electron flux $(n_e v_e)$ increases nonlinearly from

bulk to presheath and falls drastically thereafter in the sheath. The ion flux increases almost linearly from bulk to presheath and stays constant beyond the presheath. It is due to the absence of sources and sinks, like recombination, etc. Near the electrodes, the electron and ion fluxes balance each other, as shown by $n_e v_e / n_i v_i = 1$ in the electron to ion flux-ratio profile. Hence, in case of dust grains located in the presheath and the sheath, ion currents at both locations are almost equal, but the electron current is smaller in the sheath, resulting in a reduced charge in the sheath. The charging time increases when dust is moved from the bulk towards the sheath, due to the same reason. In the presheath, the electron density is comparable to the bulk value, but the effective electron flux has a maximum there. From the flux-ratio profile, $n_e v_e / n_i v_i$ value at the presheath is greater than the value at the bulk. Hence, the charge number in the presheath is equal to or slightly larger than the bulk value.
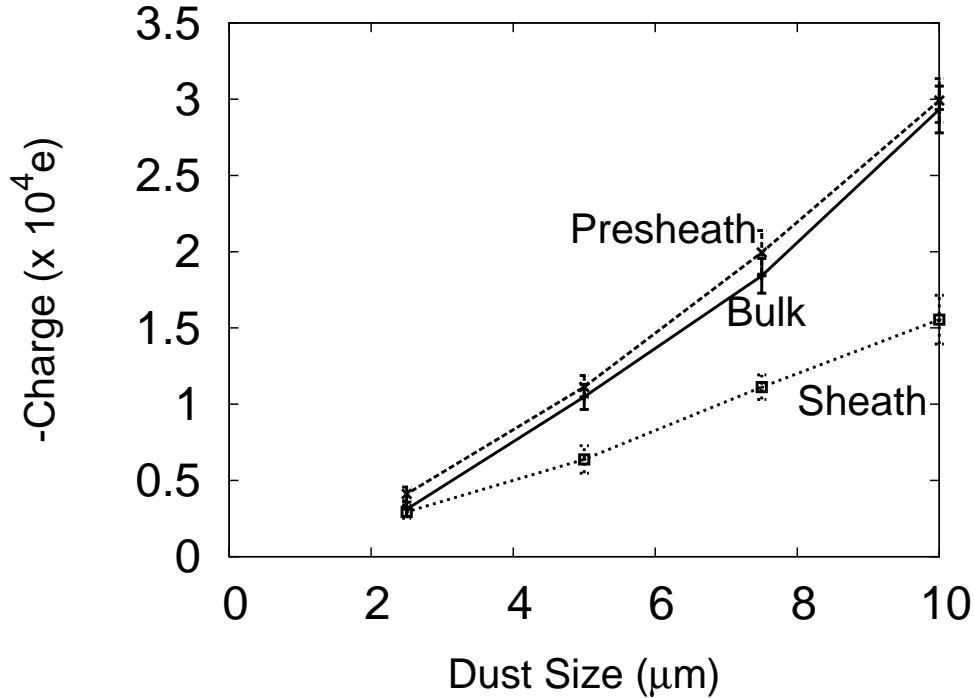
Figure 5.11: Dust charge as a function of size for the different locations of the dust grain

Now the dust charge as a function of size for different positions in the plasma is studied (Fig. 5.11). The charge number on the dust increases nonlinearly with the dust radius. This can be understood from the capacitor model, where the charge is given by Eq. 2.11. As $r_d \ll \lambda_s$ for the present case, $Q_d \propto r_d \phi_d$. In the previous section, it

has been shown that the dust potential (ϕ_d) scales almost linearly with the dust size, resulting in a nonlinear dependence of charge on dust size.

The dust charge from the simulations is in general reasonable agreement with experiments [109, 162]. In experiments on Yukawa balls with particles of 1.7 μm radius a charge of about 2000 is found [109], whereas the simulations yield 2800 charges for a particle of 2.5 μm. From melting experiments [162], a charge of about 9000 is measured for a 4.7 μm radius particle. Here, the simulations suggest a value of about 10400 for 5.0 μm size particle. Shielding lengths can also be derived by fitting the above function with inclusion of the shielding term (Eq. 2.11) to the Q_d, ϕ_d data obtained in the simulations. The shielding lengths derived from this method are about 192 μm, 200 μm, 310 μm respectively for dust grains located in bulk, presheath and sheath. These values are consistent with the values obtained from potential distribution curves in Sec. 5.3.3. If the shielding length in the bulk were smaller than the computed value, in the capacitor model the term containing the shielding length would also play a more dominant role and the size-dependence of dust charge would be even stronger than that already obtained.

5.3.5   Comparison with theoretical models

Now we discuss the effect of ion-neutral charge-exchange collisions, which are dominant in rf discharges in Argon. In order to do this, simulations have been performed switching-off charge-exchange and excitation collisions. Also, the simulation results are compared with theoretical charging models of OML[3], ABR[1], Lampe et. al. [38] and Khrapak et. al. [2].

Figure 5.12 shows the discharge parameters at the three dust locations in the rf discharge obtained in simulations with and without ion-neutral collisions. It can be seen that the main effect of collisions is to reduce the net flow velocity. The flow velocity even in the sheath is subsonic, if collisions are considered as discussed above. If collisions are not included, the flow velocity is supersonic, as can be expected by the Bohm criterion.
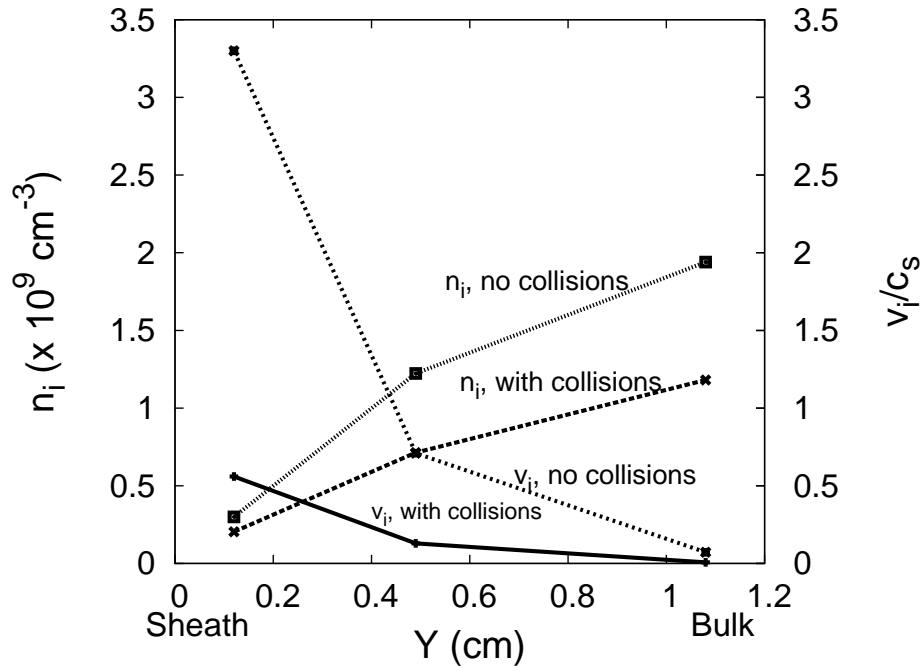
Figure 5.12: Comparison of discharge parameters with and without ion-neutral collisions
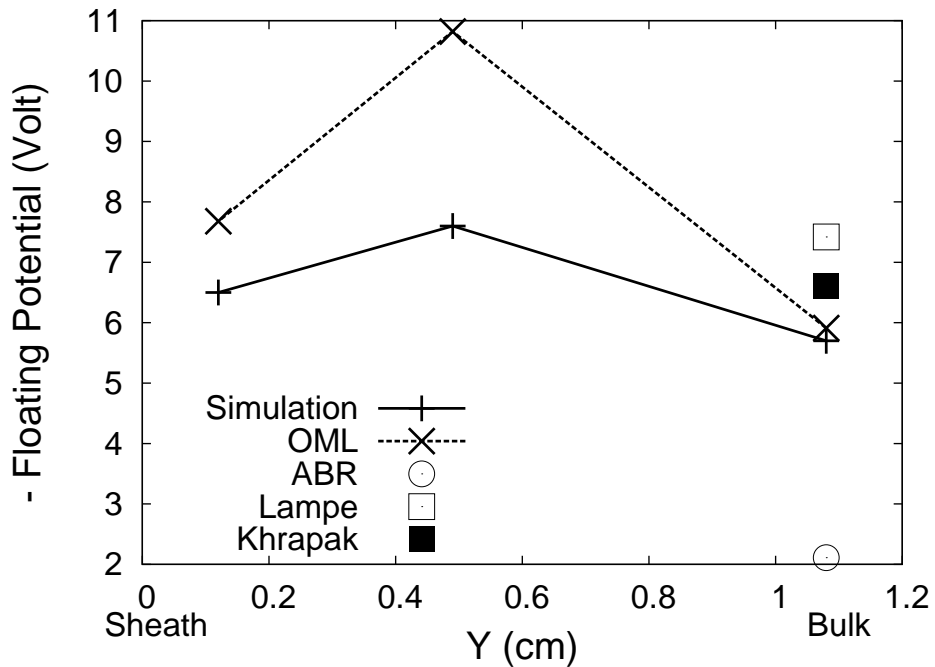
Figure 5.13: Comparison of dust floating potential with theoretical models for a 5 μm particle in case ion-neutral collisions are not considered

Figure 5.13 shows the dust floating potential values obtained without ion-neutral charge exchange collisions and excitation collisions. Also, the dust quantities computed from theoretical models (OML, ABR, Lampe, Khrapak) are presented. ABR model predicts a single value for the dust potential for a given dust size and Debye-length ratio, irrespective of collisionality. Lampe and Khrapak models do not account for streaming conditions and are given for the bulk only here. The dust potential predicted by these models has been used to obtain the dust charge from the capacitance model. In case when collisions are not considered, the dust quantities obtained in simulations are comparable to OML, except in the presheath region. The dust quantities from simulations are larger than ABR and slightly lower than the values obtained from Lampe and Khrapak models. This means that when the collisions are not effective, the ions retain their orbital trajectories and hence the OML is a good approximation.
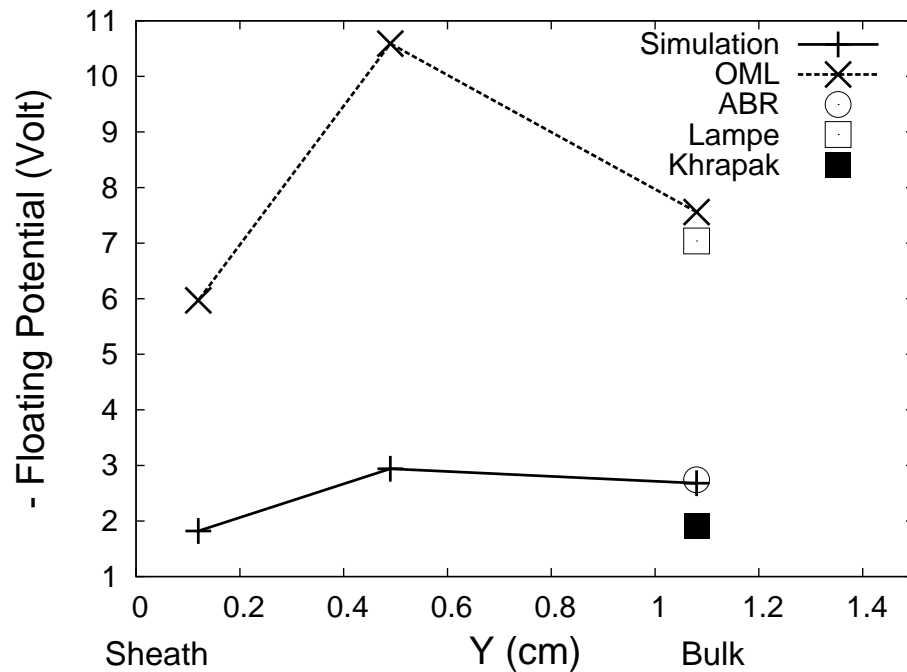
Figure 5.14: Comparison of dust floating potential with theoretical models for a 5 μm particle in case ion-neutral collisions are considered

Figure 5.14 shows the dust floating potential values obtained with ion-neutral charge exchange collisions and excitation collisions. In case when collisions are effective, the computed dust quantities are considerably lower than the calculated values from the OML model, but comparable to values obtained from the ABR model. The reason is the following: the role of collisions is to result in lower velocity ions. These low

velocity ions get attracted by the dust strongly obtaining radial motion with respect to the dust center. Hence, numerous collisions destroy the orbital motion of the ions. The dust charge obtained from simulations is slightly higher than ABR value, because of non-Maxwellian distribution.

Lampe [38] and Khrapak [2] models calculate the dust parameters as a function of collisionality index [38], which is equal to λ_s/λ_{mfp}, where λ_s is the shielding length and λ_{mfp} is the mfp for ion-neutral charge-exchange collisions. For our discharge parameters, $\lambda_{De}/\lambda_{mfp} \approx 6.5$ and $\lambda_{Di}/\lambda_{mfp} \approx 0.43$. Khrapak [2] used the ion Debye length as the shielding length. Lampe [38] used the effective screening length from both the electrons and ions, $\left(\lambda_{De}^{-2} + \lambda_{Di}^{-2}\right)^{-1/2}$ (which is again equal to the ion Debye length for our parameters), as the shielding length. But, our simulation results presented in the previous section show that in the plasma bulk the shielding length is in between electron and ion Debye lengths. As the Lampe model predicts the dust quantities only up to a collisionality index 0.5, we only consider the ion Debye length for calculations. From Fig. 5.14, it can be seen that the dust quantities obtained from the Lampe model are larger than the values obtained in simulations. We compute also the dust quantities for the Khrapak model, considering only the shielding length obtained in our simulations. Dust parameters obtained from the Khrapak model are slightly smaller than the simulation results.

5.4   Summary

Three-dimensional simulations have been carried out using a Particle-Particle-Particle-Mesh code to compute the dust charge and potential on a dust particle located at various positions in an Argon rf discharge. These simulations are very first of their kind, which account for realistic plasma background existing in experimental rf discharges. Dust charge and the potential on the dust located in the presheath are slightly larger than the charge and potential values in the bulk due to the higher electron flux in the presheath. From the presheath to the sheath, the dust parameter values decrease due to the decrease in the fluxes. It has been found that in plasma bulk and presheath regions the shielding lengths are in between ion and electron Debye lengths, indicating shielding by both ions and electrons. A linear dependence of dust potential on dust size has been found, which results in nonlinear dependence of the dust charge with the dust size. This is in agreement with the independent diagnostics of the dust charge

by charge carrier collection. The computed dust potentials have been compared to the OML and ABR models as well as models of Lampe and Khrapak. The simulated dust floating potentials are comparable to values obtained from ABR and Khrapak models, but much smaller than the values obtained from the OML model.

Chapter 6

Ion Drag on single dust particles

6.1   Introduction

The ion drag force is the force exerted on a dust grain immersed in a plasma, due to the interaction between the dust grain and streaming plasma ions. It is one of the dominant forces acting on a dust grain [6] in laboratory rf discharges. Recently, the force has received great attention for its crucial role in phenomena such as the void formation in microgravity dusty plasma experiments [29–31]. The ion-dust interaction is also of importance for the formation of wake-fields in rf sheaths [27]. In this chapter, simulations have been performed to quantitatively determine the ion drag force under realistic discharge conditions.

6.2   Method of computation

The parameters of the simulation, discharge conditions and computational scheme is similar to the one explained in previous chapters. Ion drag is computed in the following way for dust particles with radii $R_d = 2.5$, 5.0, 7.5 and 10.0 μm introduced at different locations into the discharge. The collection part of the ion drag force (F_{coll}) is computed by summation of momenta transferred by all ions which cross the computational dust grain boundary during the averaging time t_{av} as,

$$F_{coll} = \frac{\sum_{ions} m_i v_i}{t_{av}}, \tag{6.1}$$

where m_i is the mass of the Ar^+ ion and v_i is its velocity at the time of collision with the dust grain. F_{coll} is also corrected to account for the drag contribution due to ion trajectories prior to absorption. The orbital ion drag force (F_{orb}) is computed as the sum of the momenta transferred by all other ions in MD region, which are scattered in the dust field and do not cross the computational dust grain boundary, during the averaging time from:

$$F_{orb} = -\frac{q_i \sum_{ions} E_i}{t_{av}/\Delta t_{MD}}, \tag{6.2}$$

where q_i is the ion charge, E_i is the dust electric field at the ion location and Δt_{MD} is the subcycle time step inside the MD region. E_i is computed as $E_i = Q_d/4\pi\epsilon_0 R^2$, as in the MD region particle-particle scheme of interaction between the dust and plasma species is employed. R is the distance between the ion and the dust grain. The typical averaging times (t_{av}) are about 500-1000 rf cycles. This division of forces is similar to that in the analytical models [47].

6.3   Results

Here, we present the simulation results for the ion drag force computed on a static spherical dust grain located at various positions in the rf discharge. The results will also be compared to analytical fits or theoretical models from the literature.

6.3.1   Effect of collisions on ion trajectories and ion flux

To understand the various contributions (collection or orbital) to the drag force it is necessary to study the effect of the dust electric field on the ions. In order to illustrate the effect of collisions on ion trajectories in our simulations, some ions are randomly picked, marked and followed after the dust charge has reached its equilibrium value. The trajectories of these ions have been followed including collisions of these ions with other plasma species. For comparison, the same ions have been followed from their starting point in the dust potential artificially assuming no further collisions.

Figure 6.1 shows the artificially collisionless ion trajectories around 5 μm dust grains located in the plasma bulk and the presheath respectively. It can be seen that there are three classes of ions: 1) direct ions, which are accelerated in the dust electric field and directly hit the dust grain; 2) scattered ions, which are deflected in the dust field; and 3) trapped ions, which are confined to the dust potential and permanently orbit
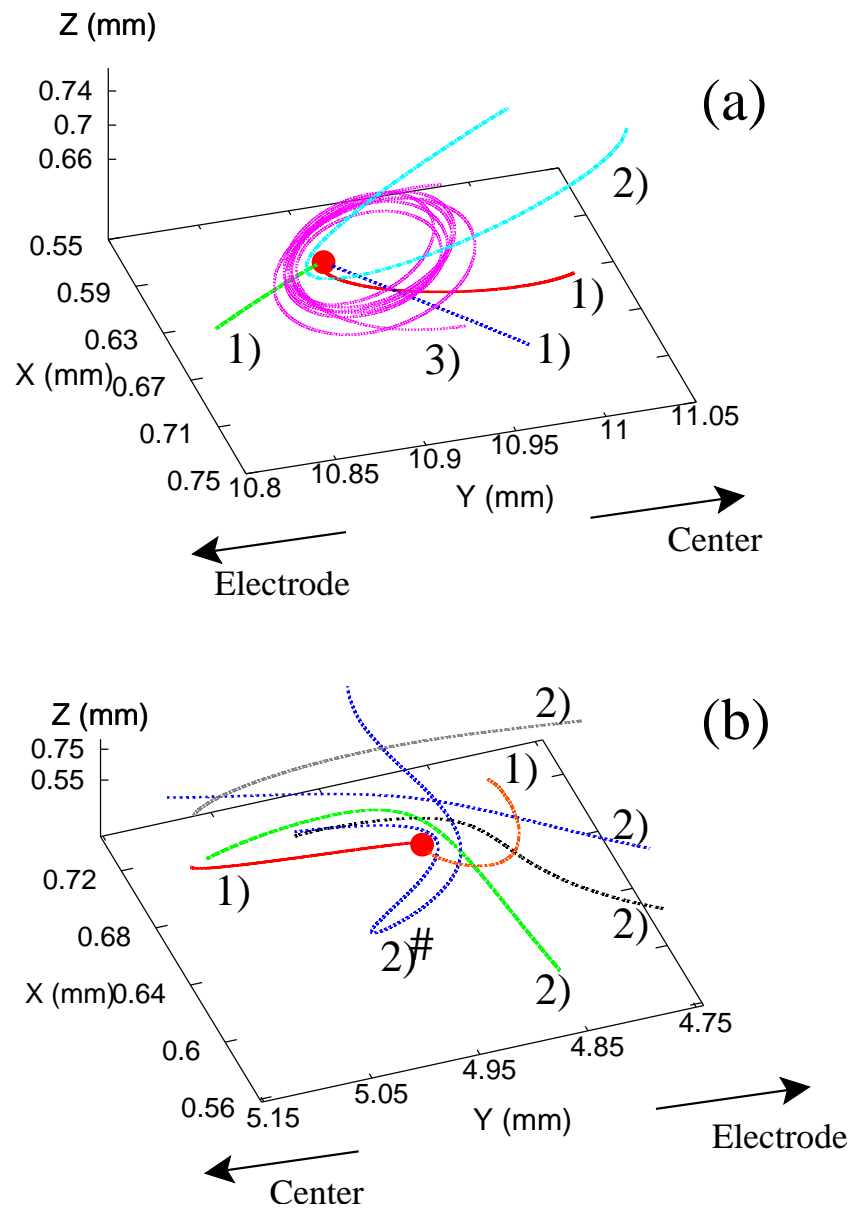
Figure 6.1: Artificial collisionless ion trajectories around the dust for dust locations in (a) the bulk (b) the presheath.

around the dust. Trapped ions have been found only around dust particles in the bulk, but not for dust particles in the presheath or sheath. It is due to the acceleration of the ions in the (pre)sheath electric field. If any ion gets scattered by more than 90° (e.g., trajectory marked # in Fig. 6.1(b)), before these ions completely encircle the dust grain, the strong electric field distort these ion trajectories and accelerate them

towards the walls. In our simulation, the direct ions would contribute to the collection drag force. The scattered and the trapped ions would contribute to the orbital drag force (although on average the contribution of the trapped ions would vanish).
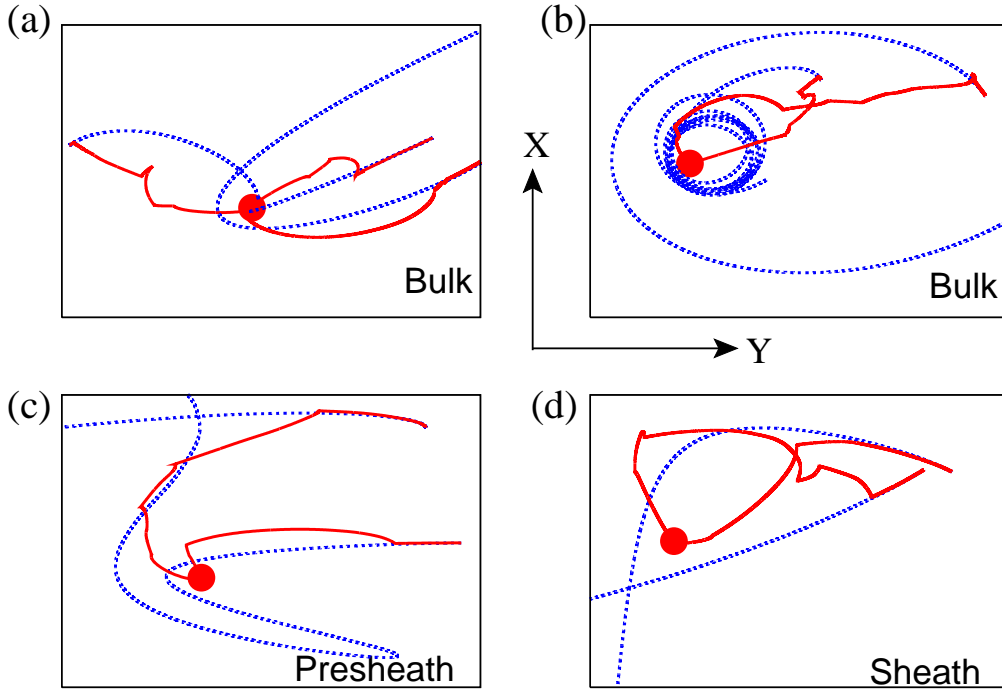
Figure 6.2: Ion trajectories around the dust located in the bulk and the presheath with collisions. Note that the three-dimensional trajectories have been projected onto the XY-plane. Dashed lines represent the artificial collisionless ion trajectories and the solid lines show the realistic collisional ion trajectories.

Now, we consider realistic ion trajectories with collisions. Fig. 6.2 shows examples of ion trajectories around the dust grains located at the three locations in bulk, presheath and sheath. Ion-neutral charge-exchange collisions are the dominant collisions affecting the ion trajectories. It can be seen that there is more than one such collision (i.e., more than one abrupt change in the direction of motion) for some ions investigated indicating the strong collisionality regime. The effect of these collisions is to result in ions with lower velocity which either fall onto the dust grain or become trapped and orbit the dust grain. After subsequent collisions, even these trapped ions fall onto the dust grain. Fig. 6.2(a)-(b) show the collisionless and collisional trajectories to the dust grain in the bulk. Due to subsequent collisions, all sorts of ions (direct, scattered and trapped) fall onto the grain. In the presheath and the sheath also collisions result low energy ions which fall onto the dust grain (see Fig. 6.2(c)-(d)). Hence, the main effect of

collisions is to increase the ion flux to the dust grain (see also [4, 39, 44]). This result can further be supported by using the values of dimensionless collisionality parameter ($\nu r_d/c_s$) used in [44], where ν is the mean free path of CX collisions and c_s is the sound speed. There, it has been shown (see Fig. 6.3) that the ion flux to the dust increases from OML value to a maximum value as the collisionality parameter increases from 0.0 to about 0.1, and then decreases (to hydrodynamic limit) with a further increase in the collisionality parameter. For our rf discharge, the values of this parameter at the three locations of the dust are 0.0022, 0.0062 and 0.017 respectively. Hence, this corresponds to a regime of flux enhancement with collisionality.
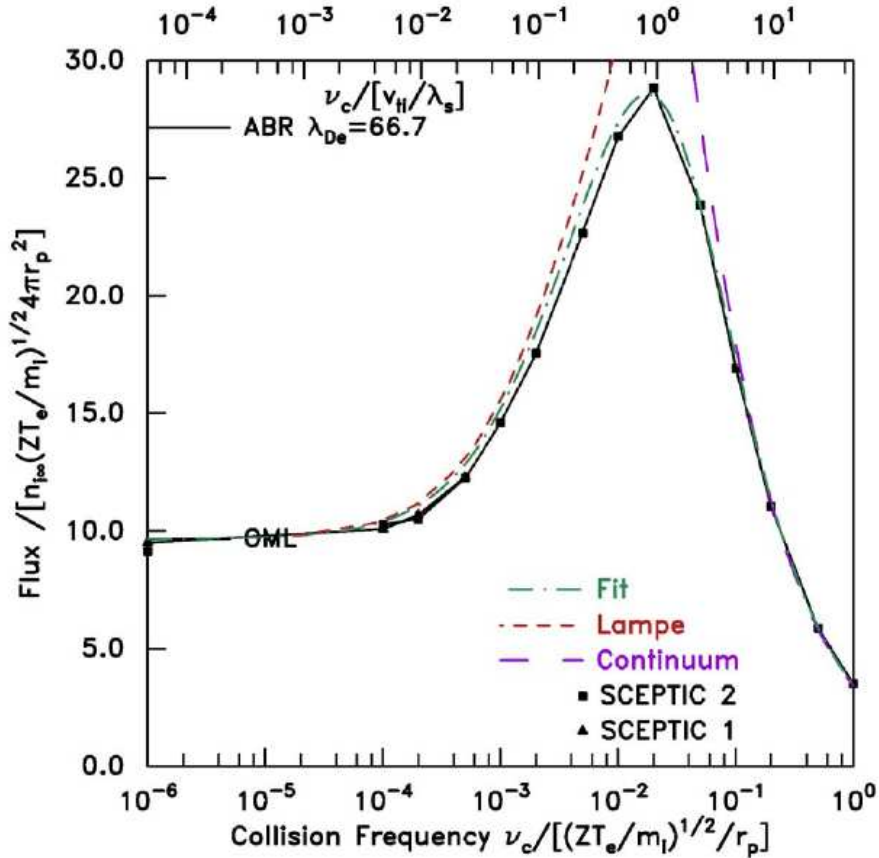
Figure 6.3: Ion collection flux to a floating sphere in Ar^+ plasma as a function of charge-exchange collision frequency (extracted from [44]).

6.3.2 Drag evolution

Figure 6.4 shows the temporal evolution of the ion drag force on a dust grain with a radius of 5.0 μm located in the presheath together with the dust charge evolution. The
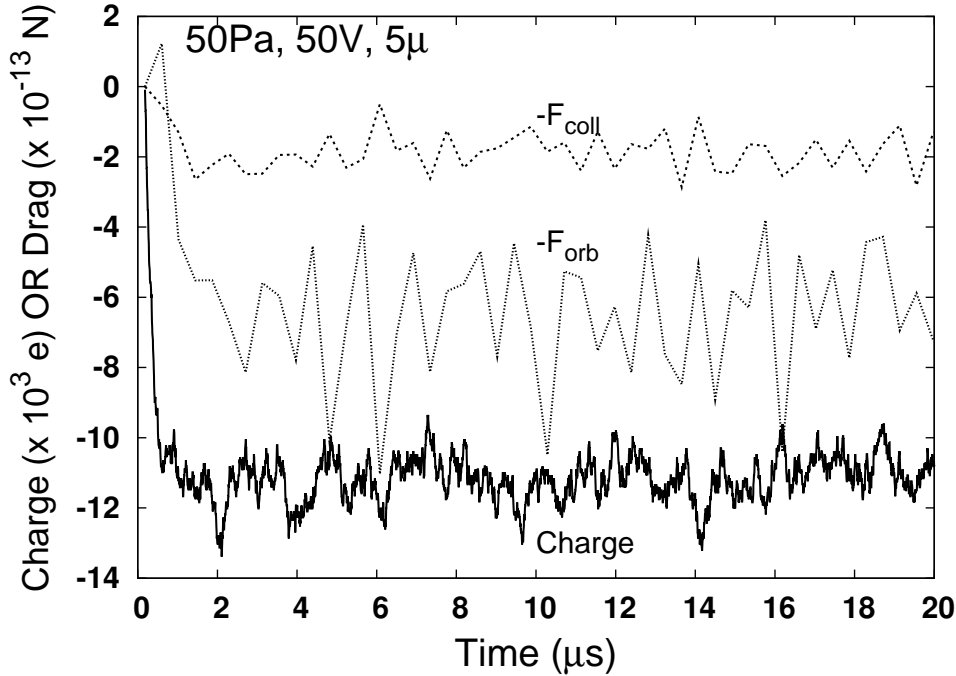
Figure 6.4: Temporal evolution of charge and drag forces on a 5μ dust located in the presheath.

drag evolution generally follows the charge evolution. As the electron and ion fluxes equilibrate, the charge on the dust reaches an equilibrium value and the dust potential also equilibrates to floating potential. Then, the drag force (collection and orbital) also equilibrates. The stochastic fluctuations in the drag force is due to the stochastic nature of the collision processes.

6.3.3   Benchmarking with collisionless models

In order to validate the ion drag computing module in the P^3M code, the computed ion drag force has been compared to the ion drag values obtained from collisionless models [43]. The reason for this choice is that for the collisionless case, sophisticated quantitative results and corresponding fit formulae are available to exactly compare with our simulations.

In order to mimic a situation close to that in [43], we have performed simulations in a modified scenario. The discharge voltage has been turned off, only Coulomb collisions between the plasma species and electron-ion elastic collisions have been considered, i.e. all inelastic collisions have been turned off. Ionization is provided by inserting plasma species in the center of the discharge. The source (i.e., number of plasma

particles introduced and frequency of insertion) and the Coulomb collision frequency
has been tuned until plasma characteristics very close to those used in [43] have been
obtained. Fig. 6.5 shows the electron energy probability function (EEPF) and ion
velocity distribution function (IVDF) obtained at a location far from source and sheath
boundary where the dust has been located. It can be seen that the plasma species
follows a quite nicely a Maxwell distribution over many orders of magnitude as required
for a quantitative comparison with [43]. The ion drag force computed for two different
flow velocities from such a simulation is presented in Table 6.1 in comparison with the
results obtained from the analytical fit from [43].
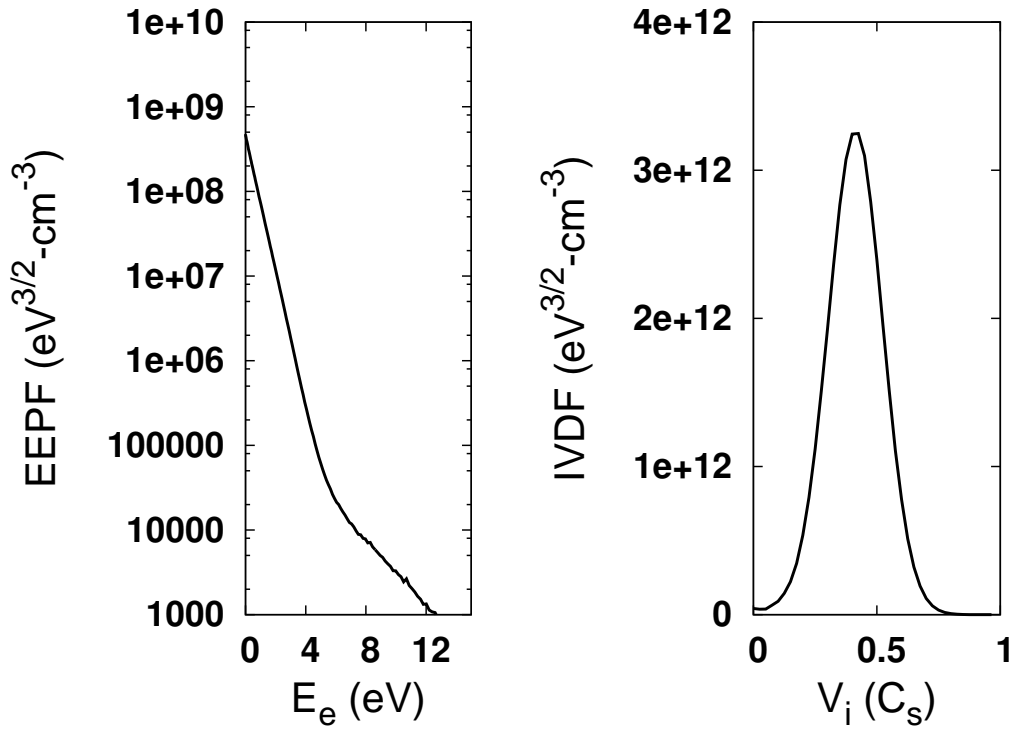
Figure 6.5: EEPF and IVDF at the dust location in a rf discharge with source at the center of the
discharge.

The values of n_i, v_{ti}, v_f, T_i, T_e, which are necessary to evaluate the force from the
analytical model are used from the computational cell upstream just outside the MD
region. The dust floating potential (ϕ_p) obtained from the simulations has been used.
The computed results agree very well with the values obtained from the analytical
formulae. Within the errors of our simulation (statistical noise) there is nearly perfect
agreement. This validates our ion drag computing module.

Table 6.1: Benchmarking our collisionless simulation with analytical formulae of a collisionless model [43]

V_{flow}	F_{coll} $(\times 10^4 \text{eV/cm})$		F_{orb} $(\times 10^4 \text{eV/cm})$	
	Simulation	Analytical	Simulation	Analytical
$0.4C_s$	0.2782 ± 0.082	0.292	3.982 ± 0.32	4.12
$2.0C_s$	1.5844 ± 0.494	1.326	3.116 ± 0.18	3.09

MD region size & Upper integral cut-off
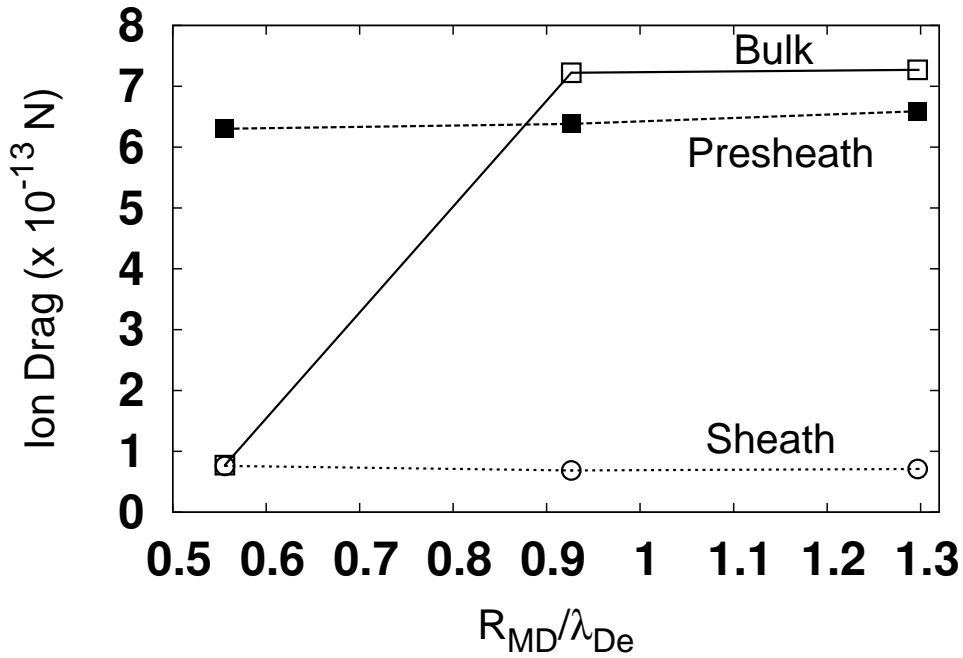
Figure 6.6: Orbital ion drag force as a function of the MD region size.

Here, we show that the size of the MD region in our simulations is suitable for the ion drag force computations. The MD region used should be large enough to account for the majority of small angle collisions which might occur even very far from the dust. Also, for the collisional plasma background, collisions occurring very far from the dust (even larger than the shielding length) may also contribute to the drag force. Using kinetic simulations with different MD region sizes, the optimal size for drag force computations can be derived. For our collisional plasma background, the shielding

lengths (λ_s) around the dust are between the electron and the ion Debye lengths [163] (see chapter 5). Hence, we have performed simulations by varying the MD region size from the smallest possible size (R_{MD}=0.55 λ_{De}) to sizes larger than one electron Debye length. From the computational point of view, a trade-off between most accurate force calculations with large MD sizes and the computational costs favoring small MD sizes has to be obtained.

Fig. 6.6 shows only the orbital drag force as a function of MD size. The collection drag force is not affected by the MD size and hence is not presented here. The simulation results suggest that MD regions equal to about half the electron Debye length (about 275 μm) are sufficient to obtain the drag force in the presheath and the sheath. This value of the MD size is of the order of the dust shielding length (λ_s). For the plasma bulk, MD regions of about one electron Debye length are necessary for the type of distribution functions exhibited by plasma species in the present rf discharges. This value is decisively larger than the computed dust shielding length (about 220 μm) in the bulk. This is since there the ions have subthermal flow speeds and are strongly affected by the dust potential even outside the dust shielding length.

The above computed MD region sizes can be qualitatively supported by looking at the averaged ion velocities around the dust at the different locations. Fig. 6.7 shows the ion density and velocity vectors around the dust grains located in the bulk, presheath and sheath respectively. In these plots, the distances are expressed in terms of the computed shielding lengths [163] at the respective locations. In the plasma bulk, ions at distances larger than the shielding length are being attracted by the dust grain supporting the above reported value in the bulk. Also, one can see that due to the low velocity of the ions, the ions have preferably a radial motion.

For dust grains located in the presheath ions at distances larger than the respective shielding length get only slightly scattered in the Coulomb field of the dust grain (Fig. 6.7(b)). This supports the derived MD region size reported above. For dust grains in the sheath, only ions very close to the grain at distances less than about half the shielding length are scattered in the dust field (Fig. 6.7(c)). Also, from the ion density plots around dust grains in the presheath and the sheath, one can see a focusing effect of flowing ions downstream under the dust grains, indicating wakefield formation.

It should be noted that the MD region size in our simulations represents the upper cut-off in the analytical theories [47, 128]. For finite sized dust particles, ions with impact (or collision) parameter (b) less than collection impact parameter (b_c) are con-
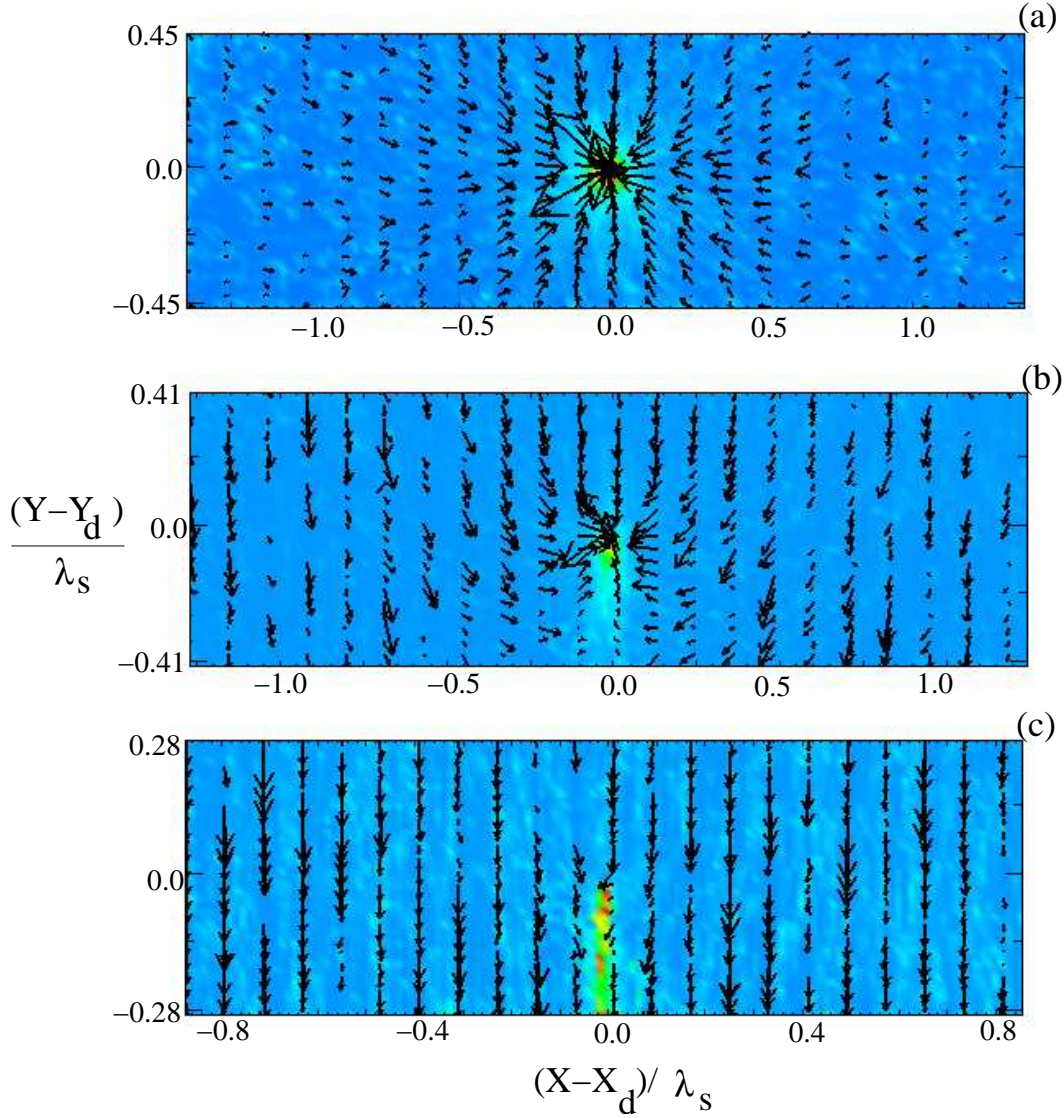
Figure 6.7: Ion density (color-coded) and velocities along xy-plane around the dust grain located in the (a) bulk (b) presheath and (c) sheath.

sidered to be absorbed by the grain and contribute to collection drag force. Ions with impact parameter $b > b_c$ are scattered and contribute to the orbital drag force. For analytically computing the orbital drag force with the long-range electrostatic potential of a dust grain, an upper limit is imposed upto which collisions are considered, which is called upper cut-off (b_u). How to determine b_u has been a point of discussion, even for collisionless plasmas for some time. In early investigations [99], the electron Debye length has been proposed as the upper cut-off. Now, it is generally proposed [43, 47–49] to use a linearized shielding length for a non-flowing plasma and to use

flow-corrected electron Debye length for a streaming plasma. This is supported by our calculations.

Ion currents to dust
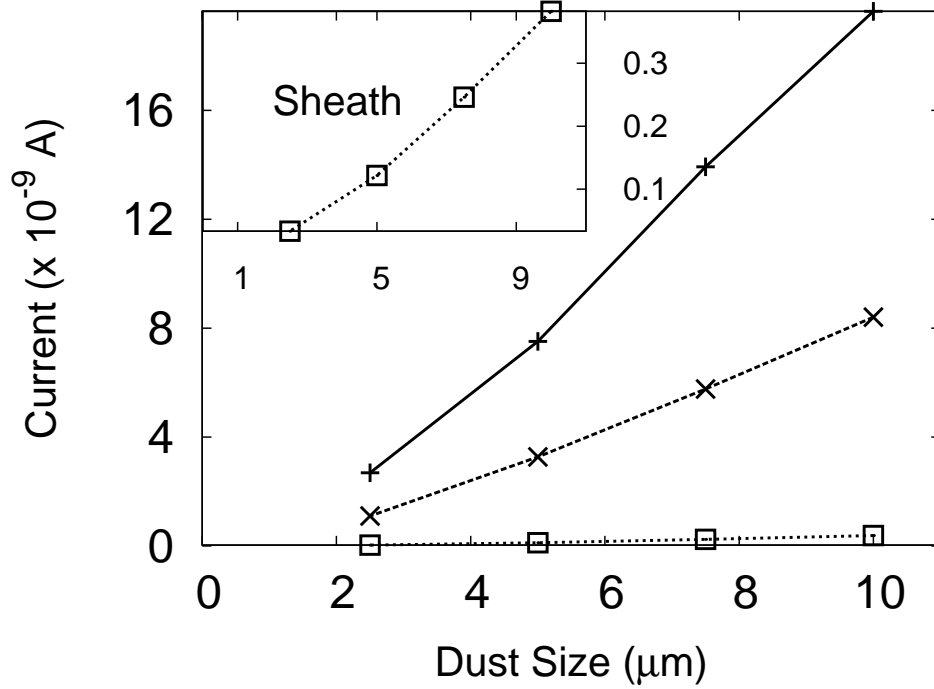
Figure 6.8: Ion current to different sizes of dust grains located at the three positions in the rf discharge. The inset shows the magnified ion currents to the dust in the sheath.

Figure 6.8 shows the total ion currents to dust grains of different size located at the three different locations in the rf discharge. The ion current decreases from the bulk to the sheath. These trends can qualitatively be explained using the flux $(n_i v_i)$ and collection cross section values at the dust locations. Fig. 6.9 shows the $n_i v_i$ profile between the electrodes in the center of the discharge for 50 Pa and 100 Pa gas pressures. The flux profile also approximately represents the flux through the Debye sphere around the grain, as the MD region size is of the order of a Debye length. Table 6.2 lists the impact parameter for ion collection $b_c(= r_d \left(1 - 2e\phi_p/m_i v_i^2\right)^{1/2})$, the 90° Coulomb collision parameter b_{90}, the Coulomb logarithm $\ln\Lambda$ and the orbital cross section σ_{orb} ($= 4\pi b_{90}^2 \ln\Lambda$) using the equations (2.29)- (2.35). The ion collection cross section ($\sigma_c = \pi b_c^2$) reduces from bulk to sheath. It is due to two factors: the dust potential reduces from

bulk to the sheath; and the ion velocity increases from bulk to the sheath. Similarly b_{90} also reduces from bulk to sheath for the same reasons. The Coulomb logarithm ($\ln\Lambda$) in Eq. (2.32), slightly increases from the bulk to the sheath due to increase in the shielding length from the bulk to the sheath. In effect, the orbital momentum cross section (σ_{orb}) reduces from the bulk to the sheath.
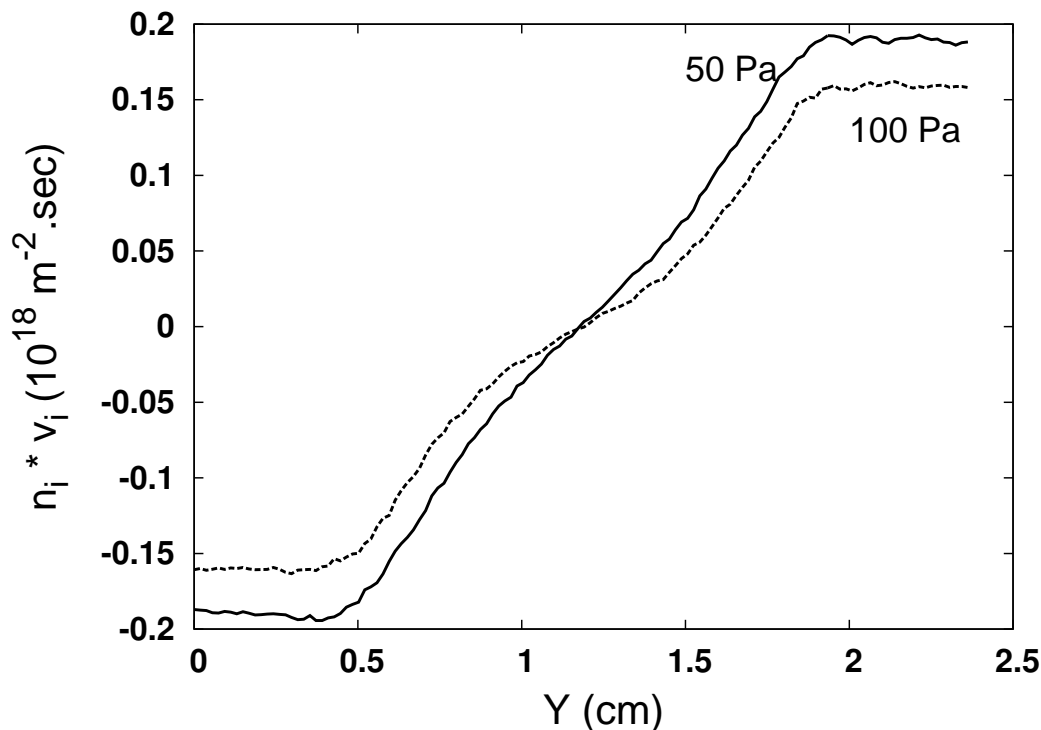
Figure 6.9: $n_i v_i$ profile between electrodes for gas pressures 50Pa & 100Pa

Table 6.2: Computed impact parameter and cross section values at the three locations for a 5 μm particle.

Variable	Sheath	Presheath	Bulk
$b_c(\mu m)$	17.9	66.1	192.
$b_{90}(\mu m)$	29.8	123.	315.
$\ln\Lambda$	1.88	0.98	0.68
$\sigma_{orb}/4\pi(\times 10^3 \mu m^2)$	1.67	14.8	67.4

The ion current is proportional to the product $n_i v_i \sigma_c$. The flux at presheath is larger than the value at bulk, but the impact parameter b_c value is smaller. Effectively

the current to the particle at the bulk location is larger than at the presheath. The flux values at the presheath and the sheath locations are equal, but the impact parameter b_c value is even smaller at the sheath when compared to the presheath value, resulting in even smaller currents to the dust located in the sheath than to the dust located in the presheath. The size-dependence of the ion current is non-linear, as expected because the flux to the grain should be proportional to the surface area of the grain.

Drag vs. dust position

The difference of the present problem from the collisionless model is due to two factors: non-Maxwellian distributions of the plasma species and the ion-neutral charge-exchange collisions. We now compare the computed results for the drag force with the collisionless models [43] and study the effect of collisions on the drag force.
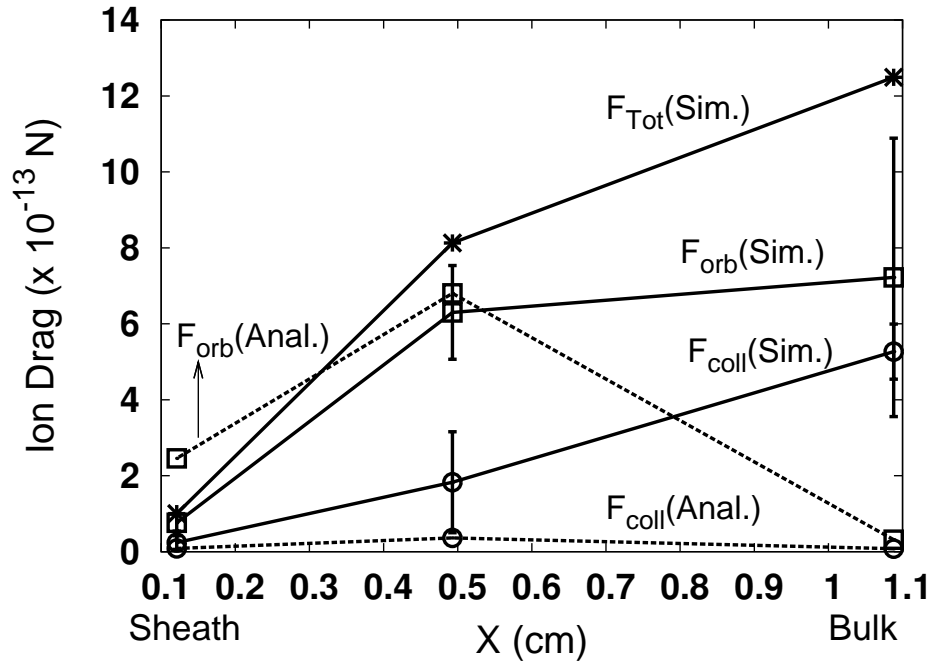
Figure 6.10: Comparison of computed ion drag force with analytical fits.

Figure 6.10 shows the computed collection and orbital drag forces for different locations of dust in the rf discharge with ion-neutral collisions. The collection drag force reduces from the bulk to the sheath. This can be explained as follows: The collection force is proportional to the product of ion collection current and average momentum. In the previous section, we already have discussed the variation of collection current as

a function of dust position, in terms of fluxes and collection cross sections. Hence, it is qualitatively reasonable to explain the drag force in terms of $v_i I_c$. The effect of collisions is to replace the high energy ion with a low energy ion at nearly neutral temperatures. As our plasma background is highly collisional, most of the ions collected by dust grain will have low and almost equal momenta for all locations of the dust. Hence, in the above product, I_c only governs the variation of the drag force. As already discussed I_c decreases from bulk to the sheath, the collection drag force behaves similarly. The orbital drag force also reduces from bulk to the sheath. The reason can again be attributed to the reduction in orbital current: Though the ion flux increases from bulk to presheath and stays constant in the sheath, the orbital momentum cross section (σ_{orb}) reduces by a few orders of magnitude from bulk to the sheath, resulting in smaller orbital current.

In Fig. 6.10, the collection and orbital drag forces obtained from the analytical fits in [43] are also shown. The (total) collisional drag force can be larger or smaller than the collisionless drag force, as it is the result of an interplay between two counteracting factors [44]. Collisions increase the ion flux to and towards the dust grain, the factor which increases the drag force. The increased ion flux reduces the charge (and potential) on the dust, which contributes to a reduction in the drag force. Hence, the normalized particle potential χ in eq. (2.29), increases or decreases depending on the relative variations in the ion momentum and dust potential due to collisions. As a result collection and orbital momentum cross sections enhance or decrease. The analytical values for the drag force in Fig. 6.10 have been obtained from Eqs.(2.29-2.35) using the plasma variables just outside the MD region, but with floating dust potentials obtained from simulations with collisions. The orbital drag force is larger than the collection drag force for both the cases. The simulated drag forces, in general, are larger than the values from analytical formulae for a collisionless case. This is the effect of increased flux towards the dust grain due to collisional plasma background. In the sheath the computed orbital drag force is smaller than the analytical value due to higher momentum of ions in the collisionless case. The total drag force is larger than the total drag force for collisionless case in the bulk and the presheath.

6.3.4   Drag vs. dust size & position

Now, we discuss the effect of dust grain size and its location in the rf discharge on the drag forces.
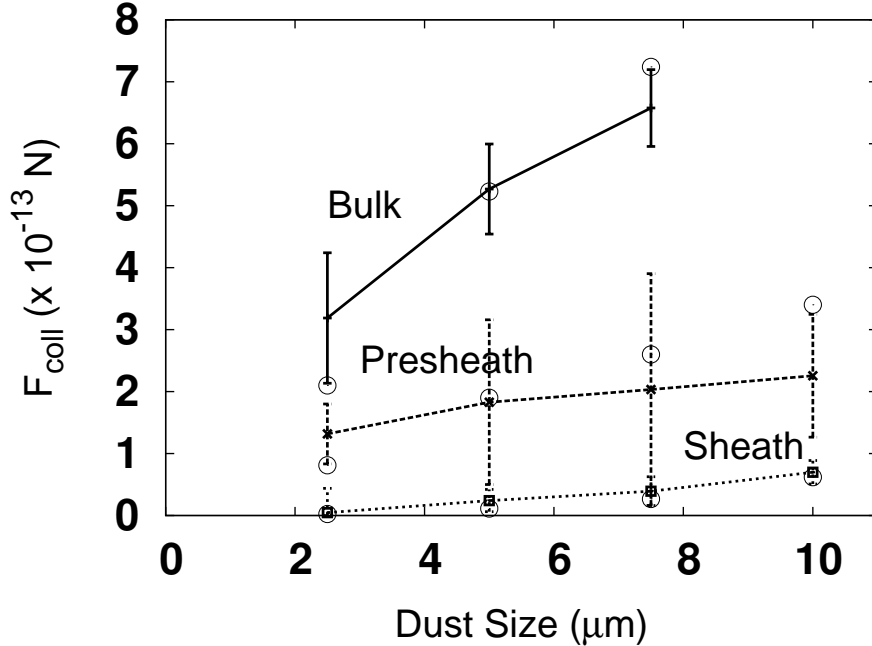
Figure 6.11: Effect of dust size and location on the collection drag force. Open circles are calculated using Zobnin's charging model.

Figure 6.11 shows the computed collection drag force for different sizes of dust located at the three positions in the rf discharge. The size-dependence of the drag force is non-linear. Also, it can be seen that the size-dependence of the collection drag force almost resembles the size-dependence of the ion current to the dust grains at the respective locations as shown in Fig. 6.8. It is due to the fact that the collection current is the dominating factor for the drag force as discussed above. In the previous chapter, we have shown that the size dependence of the dust floating potential agrees reasonably with the model proposed by Zobnin et al. [4]. This model computes the ion current to the dust grain with additional collisional ion current along with the orbital motion limited (OML) current. Hence, we used this model to calculate analytically the size-dependence of the drag force. Here, the drag force is obtained by multiplying the ion current from Zobnin's model with the corresponding momentum from the simulation. In Fig. 6.11 the so obtained force values are also shown. The so computed ion drag force agrees well with the simulation.

Figure 6.12 shows the dust size dependence of the orbital drag force for dust grains located at the three different locations in the discharge. The dust location dependence of the orbital force is already discussed. The orbital drag force in the sheath is smaller
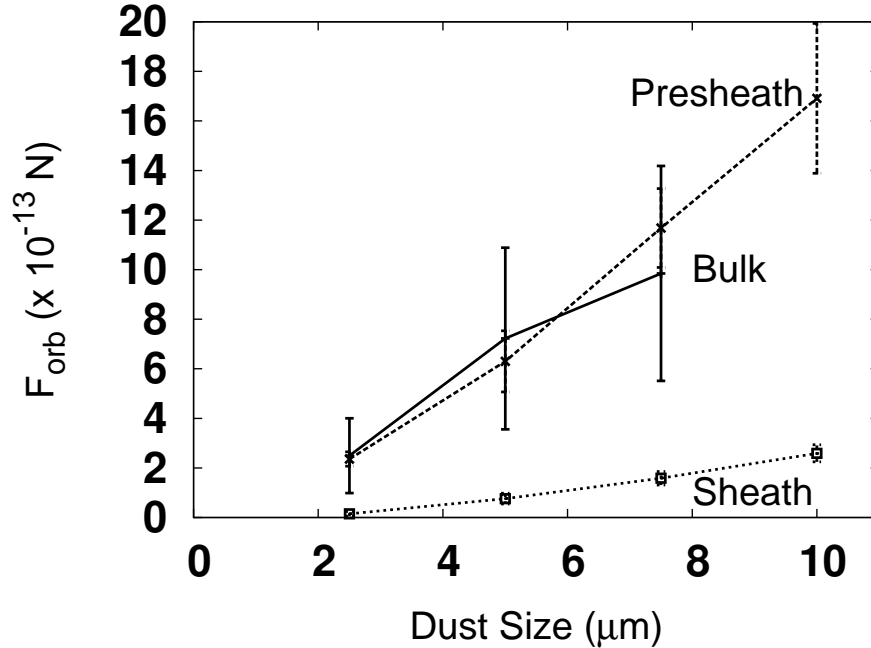
Figure 6.12: Effect of dust size and location on Orbital drag force.

than the bulk value because of the reduction in the orbital momentum transfer cross section (σ_{orb}) by several orders of magnitude. The orbital drag force scales nonlinearly with the dust size. Khrapak et al. [126, 135–137] computed drag forces for a highly collisional (hydrodynamic) background and Hutchinson et al. [127] reported drag forces for a specific ion drift velocity. Hence, a comparison for the computed orbital drag forces is not feasible, though the tests of MD size sufficiency discussed above validates the results for the computed orbital drag force.

6.3.5   Drag vs. discharge pressure

As the neutral gas pressure is varied the collision frequency changes and hence the background plasma characteristics (species density, velocities, etc.) vary. This can result in a variation of the ion drag force around the dust grain. We studied the dependence of the collection and orbital drag forces for scenarios defined by the experiment, namely a pressure between 50 to 100 Pa.

Figure 6.13 shows the results for 5 μm dust grains located at three different locations. All variations of drag forces are small and within the statistical error bars. These results agree with the results of [127], where it has been shown that the two drag
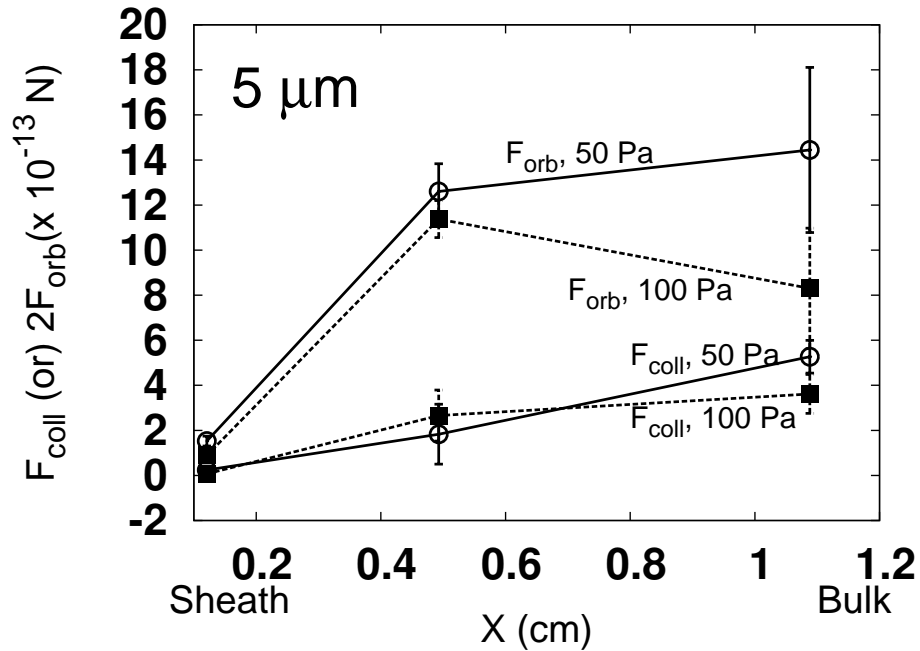
Figure 6.13: Effect of discharge pressure on collection and orbital part of the drag force for a 5 μm dust grain

contributions are very slowly varying functions of the collisionality parameter for our experimental conditions.

6.4 Summary

Three-dimensional simulations have been carried out using a Particle-Particle-Particle-Mesh code to compute the ion drag force on dust particles located at various positions in an argon rf discharge. All the other existing models of ion drag force are incomplete in treating exact plasma background. Here, for the first time forces for the realistic experimental conditions have been calculated. The ion drag force results have been benchmarked with previously published collisionless drag force calculations. The orbital drag force is typically larger than the collection drag force. The total drag force for the collisional case is larger than the collisionless case due to increase in the ion flux to the grain and the drag scales nonlinearly with the dust size.

Now, the above charging study is extended for multiple dust particle system and the results will be presented in the next chapter.

Chapter 7

Charging of multiple dust particles

7.1   Introduction

In the previous chapters, we have used a P^3M code to compute dust charge, floating potential and ion drag force on a single static spherical dust grain immersed in rf discharges. In reality however, the laboratory experiments (e.g. Yukawa ball experiments) involve multiple dust particles. The presence of neighboring dust particles might influence the charging dynamics and ion drag force on the dust grains. There can be competition for charges and a reduced charge number on the grains. Especially, in the flowing plasmas (sheaths), the ion focusing and wake-fields caused by one dust grain can influence the charging of neighboring dust grains. Hence, it is very interesting and important to extend the charging and drag force studies to two and multiple dust particles immersed in the rf discharges. We again use the static dust grains for the present study.

7.2   Method of computation

The method of computation is similar to the one described for single particle studies. Argon with pressure p = 50 Pa and temperature T = 300 K is used as background gas. The scheme of the placement of two dust particles is shown in Fig. 7.1. Dust particles with radius R_d = 5.0 μm and with separation distance b along X (normal to discharge axis, Y) are introduced into the discharge. As before the position of the dust particles was fixed at three different positions of Y = 0.12, 0.49 and 1.08 cm, which corresponds to locations in sheath, presheath and bulk regions respectively (in Z

direction, the particles are centered in the simulation domain). A big MD region around the two dust particles, which contains cells with dust particles and neighboring cells, is considered for resolving plasma species trajectories around the dust particles. The separation distance b is varied from $b_{max}=1000$ μm to $b_{min}= 45$ μm. Here, b_{max} roughly corresponds to several shielding lengths ($\lambda_s=200$, 220, 320 μm in bulk, presheath and sheath) or nearly two electron Debye lengths. b_{min} roughly corresponds to one ion Debye length. The dust separation is varied and the charge, potential and ion drag forces on the two dust particles have been computed following the methods explained in the previous chapters.
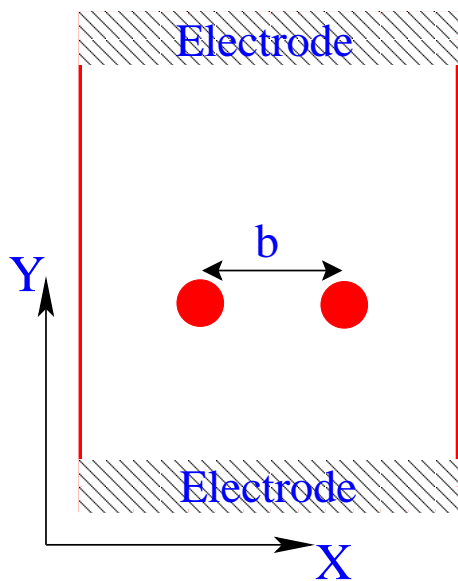
Figure 7.1: Scheme of the two dust particle system

In the case of study with multiple dust particles, we have carried out simulations with nine 5 μm static spherical dust particles arranged in a 3x3 grid as shown in Fig. 7.2, where the central dust particle position matches the location of the dust particle in the single dust study. In Z direction, the particles are centered in the simulation domain. Such set of nine dust particles is placed at various locations in the discharge (bulk, presheath and sheath) with dust separation distances $b = 186$ and 372 μm. Consequently, the charging dynamics have been studied. A big MD region around all the dust particles similar to two dust particle case is considered.
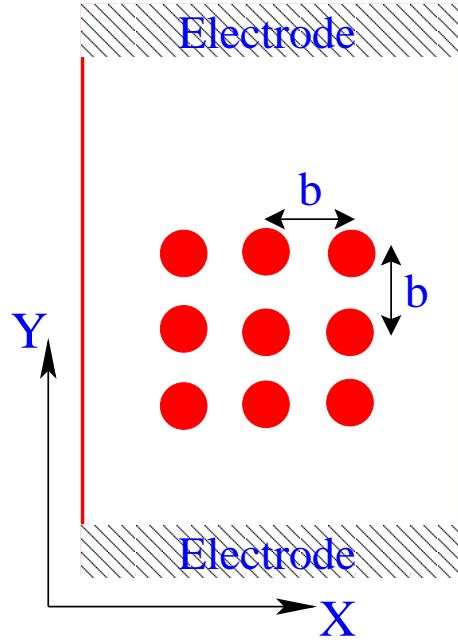
Figure 7.2: Schematic representation of nine dust particle locations in the XY-plane of the discharge.

Note on the effect of periodic boundary: Periodic boundary conditions are used at boundaries in the X and Z directions. Hence, even for the single particle case there exists mirror dust particles. If the particle is very close to the boundary and therefore to the mirror particle, the presence of the mirror particles will affect the computational results. Hence, in all the cases (single or multiple dust particles), the dust particles are placed so that the distance between the real and mirror particles is a few electron Debye lengths. At these larger separations the periodic boundary (the presence of a mirror particle) should not affect the charging of the real particle. e.g. in case of the two dust particle system, the distance between the left particle and its ghost particle (same is the case with the right particle) is about 7 electron Debye lengths.

7.3   Results: Two dust particles

Here, we present the simulation results for the charge, potential and ion drag force computed on two static spherical dust grains located at various positions in the rf discharge. The results will also be compared to the single particle dust parameters obtained in previous chapters.

Figure 7.3 shows the computed dust charges on the two dust particles when they

are located in the bulk and in the sheath, for different dust separations (b). The dust separation b is expressed in normalized units of shielding lengths at the respective locations (200 μm for the bulk and 320 μm for the presheath). At larger separation distances of nearly four shielding lengths the charge on the two dust particles is equal to the charge value obtained from single dust particle studies in the previous chapters. That means the two dust particles do not interact and behave as two single dust particles. This validates the functionality of our extended computational algorithm for multiple particles. As the separation distance is decreased the computed dust charges on the two dust particles at any location do not vary much, even if the dust grains are only separated by a distance as small as 45 μm.
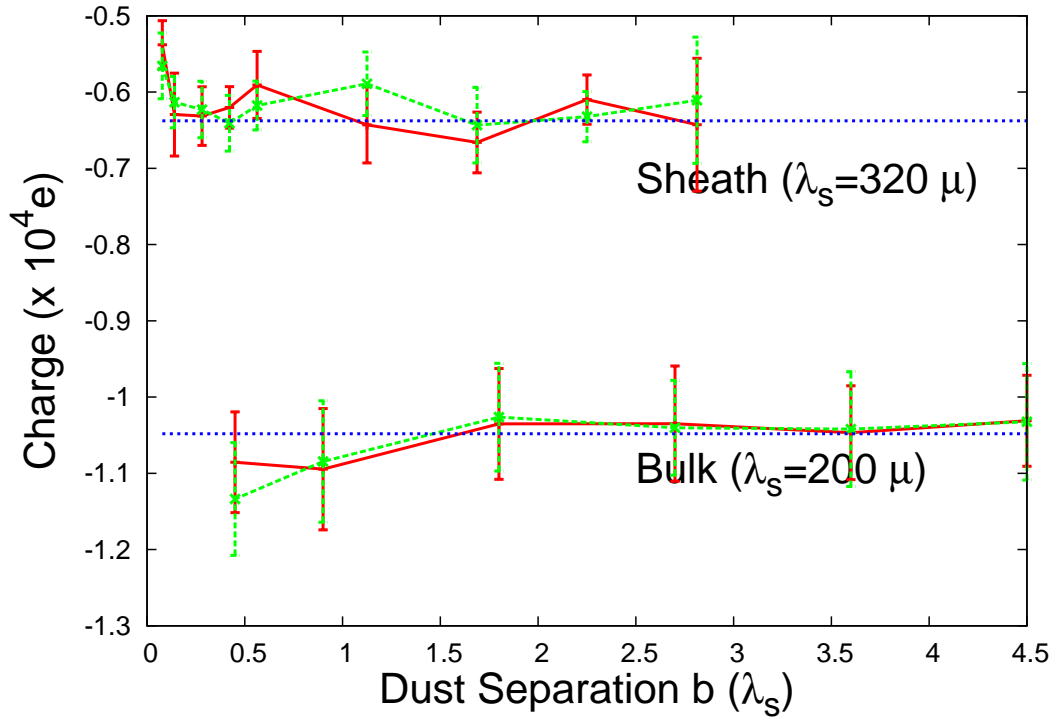
Figure 7.3: Computed dust charge on two dust particles located in the bulk and in the sheath (red/green). The blue dashed line corresponds to the single particle case.

In the Fig. 7.4, we present the computed floating potential values for the two dust particles located in the bulk and also in the sheath. The floating potential also behaves in a similar way to that of the dust charge, i.e., the floating potential at larger separation distances is equal to the computed value in the single dust grain studies and as the separation distance is decreased the floating dust potential does not vary much. This can be explained as follows: The plasma background is highly collisional, as shown

in the previous chapters. The collisions destroy the orbital motion of the plasma species and they fall radially on the grains. Due to collisions the flux onto the grains increases (as already discussed in chapter 6 based on the arguments of ion trajectories, the ion current and comparison with Hutchinson's work) and due to this there are always enough plasma species to charge the two dust grains equal to the single dust value for any separation distance. To qualitatively support this further, the collection impact parameter values (b_c) from collisionless theories can be used, though the present plasma background is collisional. The values of (b_c) at the dust locations in the sheath, the presheath and the bulk are 17.9, 66.1 and 192 μm respectively (see Table 6.2 in chapter 6). The impact parameters at various locations are either smaller or comparable to the smallest dust separation distance. Hence, for all dust separations, there is enough supply of plasma species so that the two dust particles charge up to nearly the single particle value.

In the presheath also, a similar charging behavior of the two particles is observed.
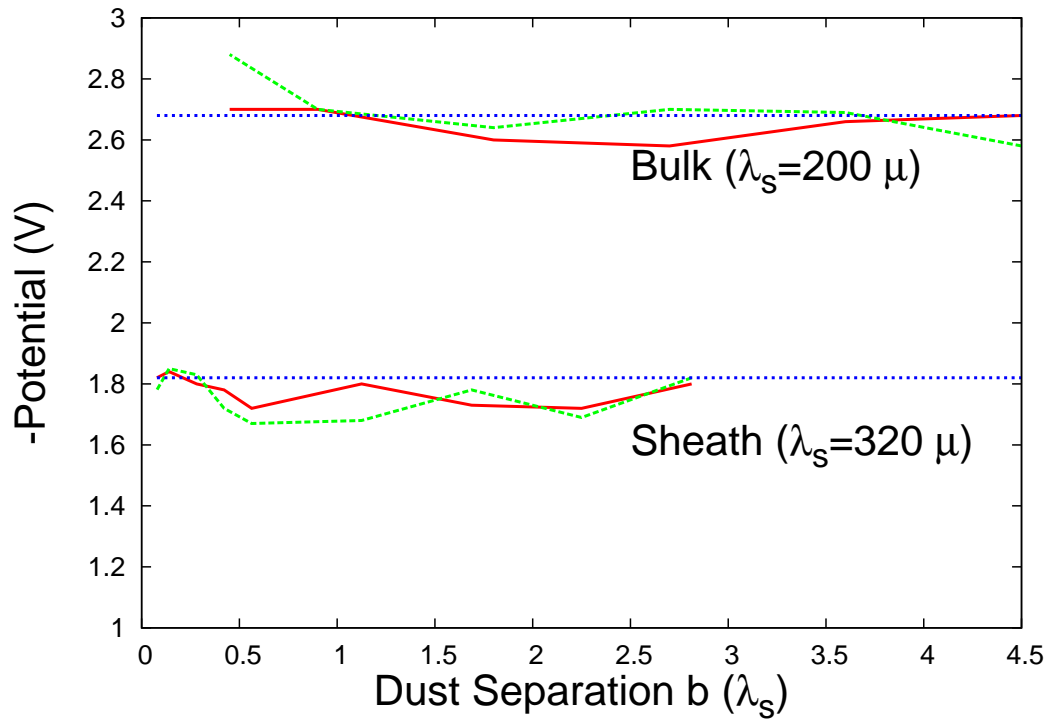
Figure 7.4: Computed dust floating potential on two dust particles located in the bulk and in the sheath. Red and green lines indicate the potential on the two dust particles, the blue dashed line indicates the single particle case.

Figure 7.5 shows the orbital ion drag force obtained from our computations of

the two dust particles located in the bulk and in the presheath as a function of dust separation distance. At larger separation distances of nearly four shielding lengths the ion drag force on the two dust particles is equal to the value obtained from single dust particle studies in previous chapters. This means the two dust particles behave like noninteracting dust particles at such separation distances. As the separation distance is decreased the orbital ion drag force remains equal to the single particle value. For lower dust separation distances (below one λ_s in the presheath and $1.5\lambda_s$ in the bulk) the drag force increases rapidly with reduced separation distance. Hence, for dust particles in the sheath, presheath and bulk, the interaction starts when the separation is below about one shielding length.
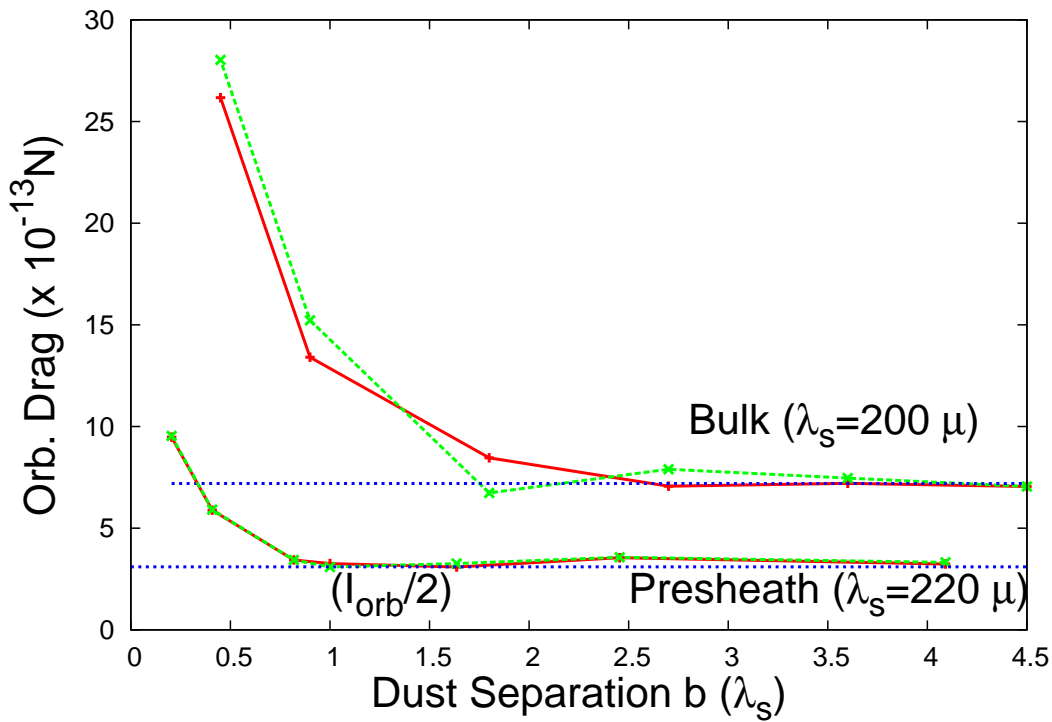
Figure 7.5: Orbital ion drag force on two dust particles (red/green lines) located in the bulk and in the presheath (drag values in presheath are scaled by a factor or 1/2 to appear on this scale). The blue dashed line indicates the single particle case.

Hence, for dust particles located in the bulk, the dust particles' interaction dynamics start when the separation distance is little higher than the shielding length at the corresponding location. For the dust particles located in the presheath and the sheath, the interaction between the dust particles starts for separation distances on the order of the shielding length at the respective location. The mechanism of interaction, i.e.,

the increase of the ion drag force can be explained as follows:
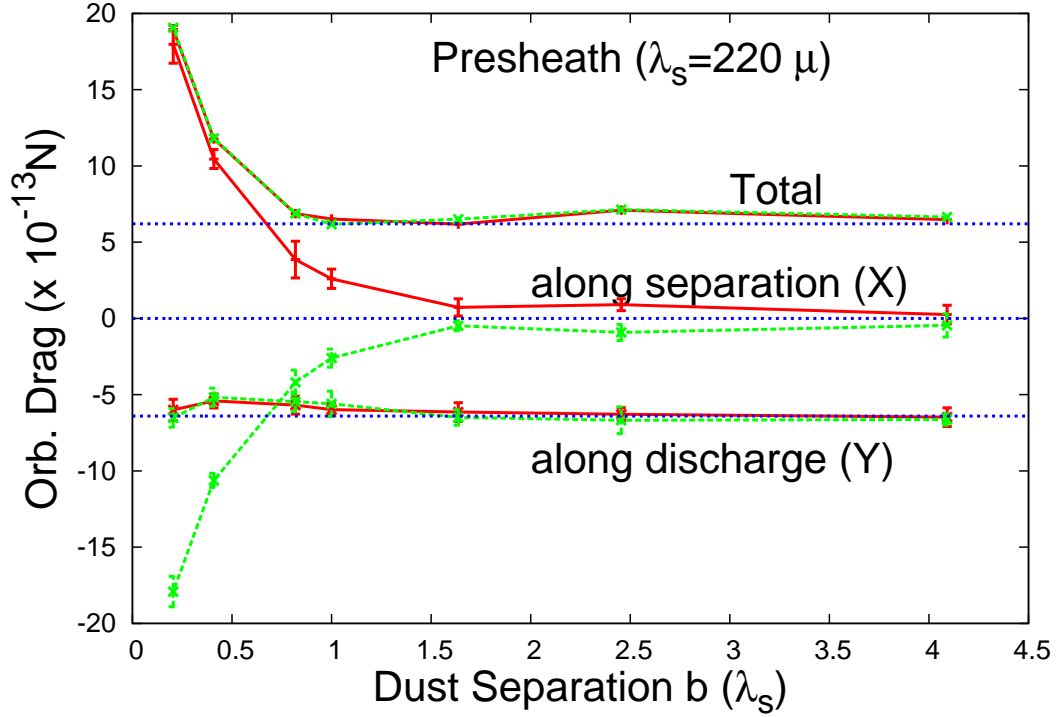
Figure 7.6: Variation of different orbital ion drag force components on the two dust particles (red/green) located in the presheath with the dust separation. The blue dashed line indicates the single particle case.

Figure 7.6 shows the variation of X-, & Y- components (along dust separation direction and along discharge direction respectively) of orbital ion drag force on the two dust particles placed in the presheath as a function of dust separation distance. The figure also shows the total ion orbital drag force variation with the dust separation. In the case of a single dust particle, the results presented in the previous chapter show that the X-component of the drag force is zero, as the force exerted by the ions left and right to the dust compensate. Hence, the total drag force is equal to the Y-component of the drag force for single particle case. In the present case of a two dust particle system, the component along the discharge direction is equal to the single particle value for all dust separations. But, the drag component along the dust separation (X) is zero for very large dust separations, implying that the two dust particles behave as two single dust particles at these distances. Hence, the total drag force is equal to the single particle value for larger separations. The X-component of the drag increases rapidly when the dust separation is reduced below one shielding length. This drag

force direction is towards positive X direction for the left particle and towards negative X direction for the right particle, i.e. the dust particles experience an attractive force. This is due to the decrease of the X-component of velocity for ions in the region between the two dust particles. This effect is analyzed in more detail in the following.
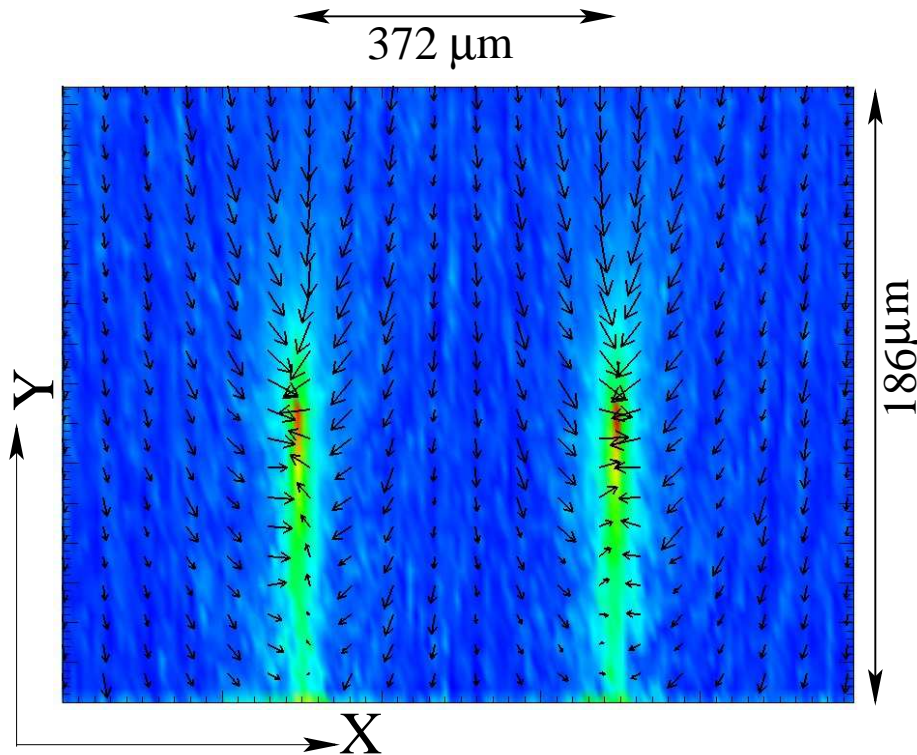
Figure 7.7: Ion density (color-coded) and velocities along xy-plane around the dust grains located in the presheath (b=372 μm)

The increase in the parallel drag component can be further explained using the ion density and velocity vector plots shown in Figs. 7.7 and 7.8. These correspond to the dust particles located in the presheath with separations $b = 372$ and 186 μm respectively. The situation can be schematically depicted as in Fig. 7.9. Let us divide the MD region into three regions as shown in the figure. For large separations greater than the shielding length, e.g. $b = 372$ μm the case in Fig. 7.7, the dust particles behave as two single particles. The parallel drag contributions to the left dust from regions 1 and 2 (and to the right dust from regions 2 and 3) are the same resulting in a zero parallel drag component for larger separations. This symmetry is broken when the separation between the two particles is within the shielding length, e.g. $b = 186$ μm the case in Fig. 7.8. In this case, ions in the region 2 are attracted by both dust particles distorting their original trajectories to more vertical ones. Hence, the parallel
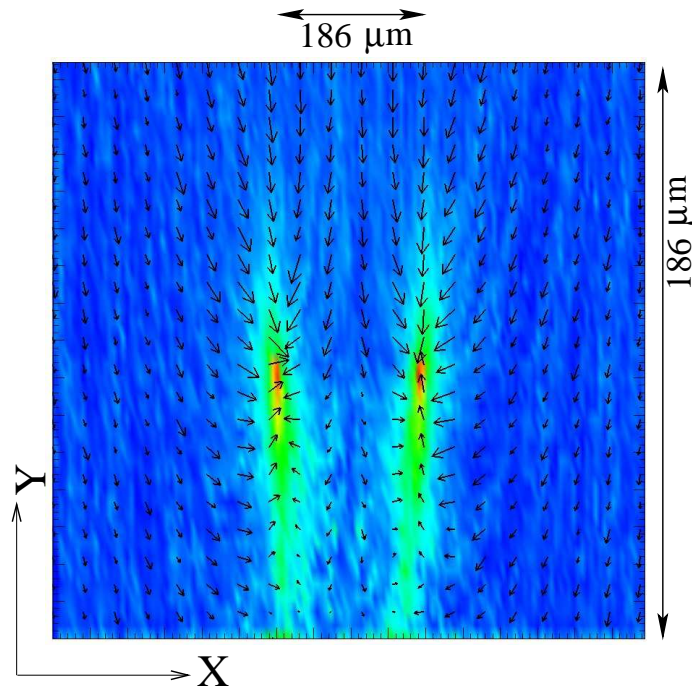
Figure 7.8: Ion density (color-coded) and velocities along xy-plane around the dust grains located in the presheath (b=186 μm)

velocity component of these ions decreases. But, in regions 1 and 3 the ions' parallel component does not change, resulting in a net force in the positive X-direction for the left dust particle and in the negative X-direction for the right dust particle. This degradation in the parallel component of the velocity can indeed be seen in the color plot of this velocity component in Fig. 7.10. Here, the parallel velocity component is plotted for two dust separations for the dust particles located in the sheath.
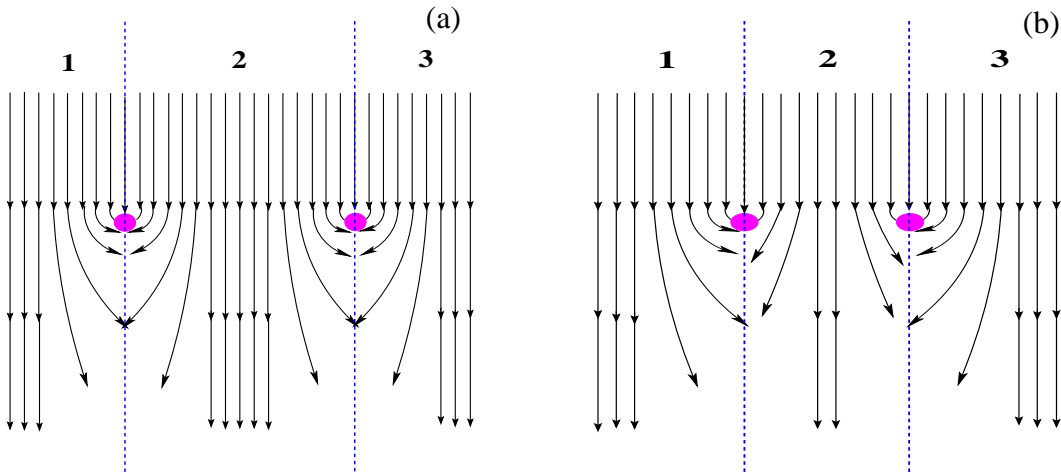
Figure 7.9: Schematic picture showing ion trajectories around two dust particles for (a) a very large separation and (b) a small separation.
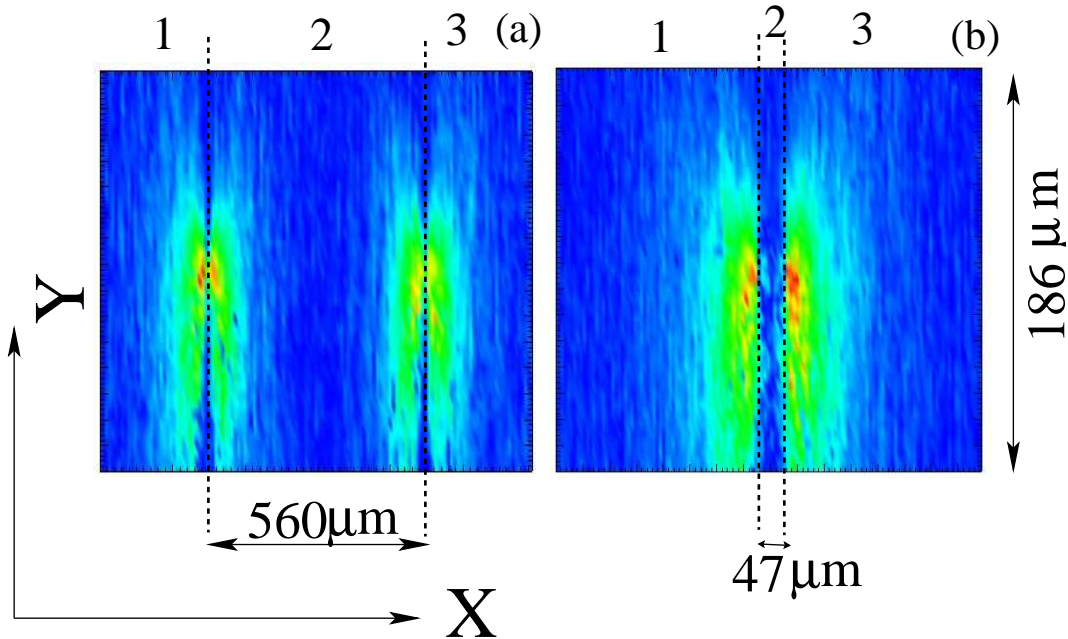
Figure 7.10: Plot showing the parallel (X) velocity component of ions around two dust particles in the sheath for (a) $b = 560$ μm (b) $b = 47$ μm.

Hence, due to the distortion of trajectories of the ions between the two dust particles for smaller separations within the shielding length, the asymmetry in the parallel velocity component raises which results in an increase in the parallel component of the drag force. Therefore, the total orbital ion drag force increases when the separation distance is of the order of or within one shielding length.

The collection drag force, which is due to ions colliding with the dust particles,

behaves in the same way. Fig. 7.11 shows the variation of collection ion drag force components on the dust particles along the discharge and along the dust separation directions with the dust separation b. Here, we illustrate the case of dust particles located in the presheath. For larger dust separations, the component along the discharge direction (Y) is equal to the single particle drag value and does not vary much with the dust separation. The collection drag component along the dust separation (X) is equal to zero for larger separations, resulting in the total collection drag force at larger separations being equal to the single particle case. For dust separations of the order of one shielding length the parallel component increases due to the same reasons explained above. This results in an increase in the total collection drag force at such separations.
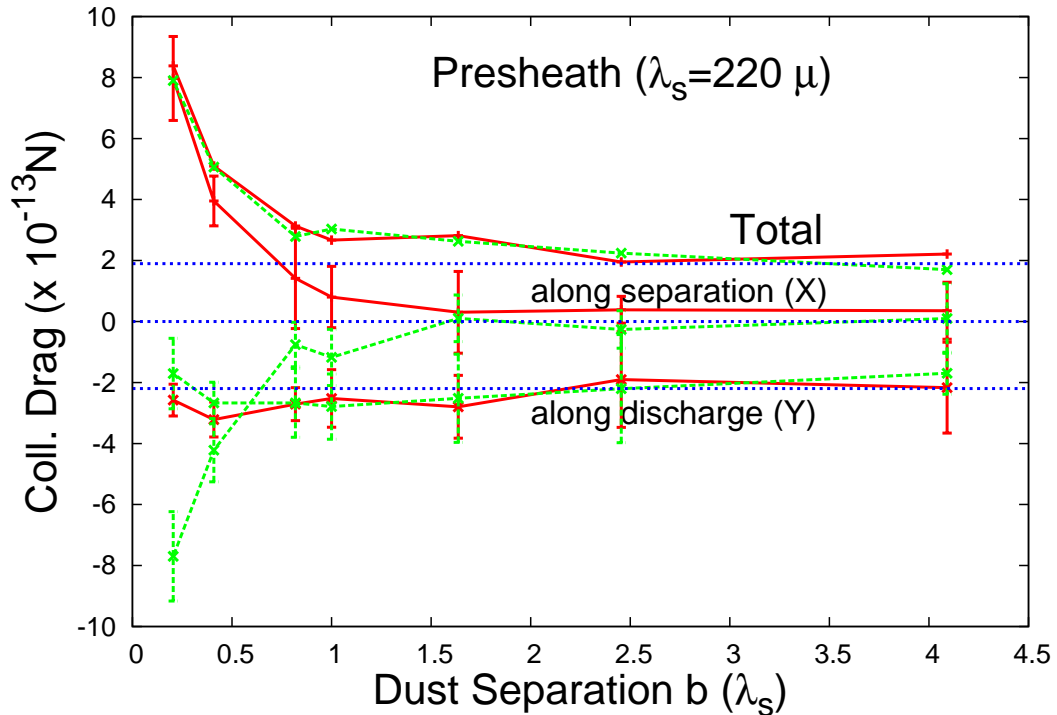
Figure 7.11: Variation of different collection ion drag force components on the two dust particles (red/green) located in the presheath with the dust separation. The blue dashed line indicates single particle case.

Hence, the dust charges and potentials on the two dust particles match with single particle values and do not vary for all dust separations. But, for separation distances below one shielding length the ion drag force increases due to the building up of asymmetry along the dust separation axes caused by a decrease in the parallel velocity

component for ions between the dust particles.

7.4   Results: Multiple dust particles

Now, it is interesting to extend this study to multiple particle systems where we have an extension of the dust system along the discharge direction Y. We have carried out simulations with nine 5 μm dust particles arranged in 3x3 grid as shown in the Fig. 7.2.
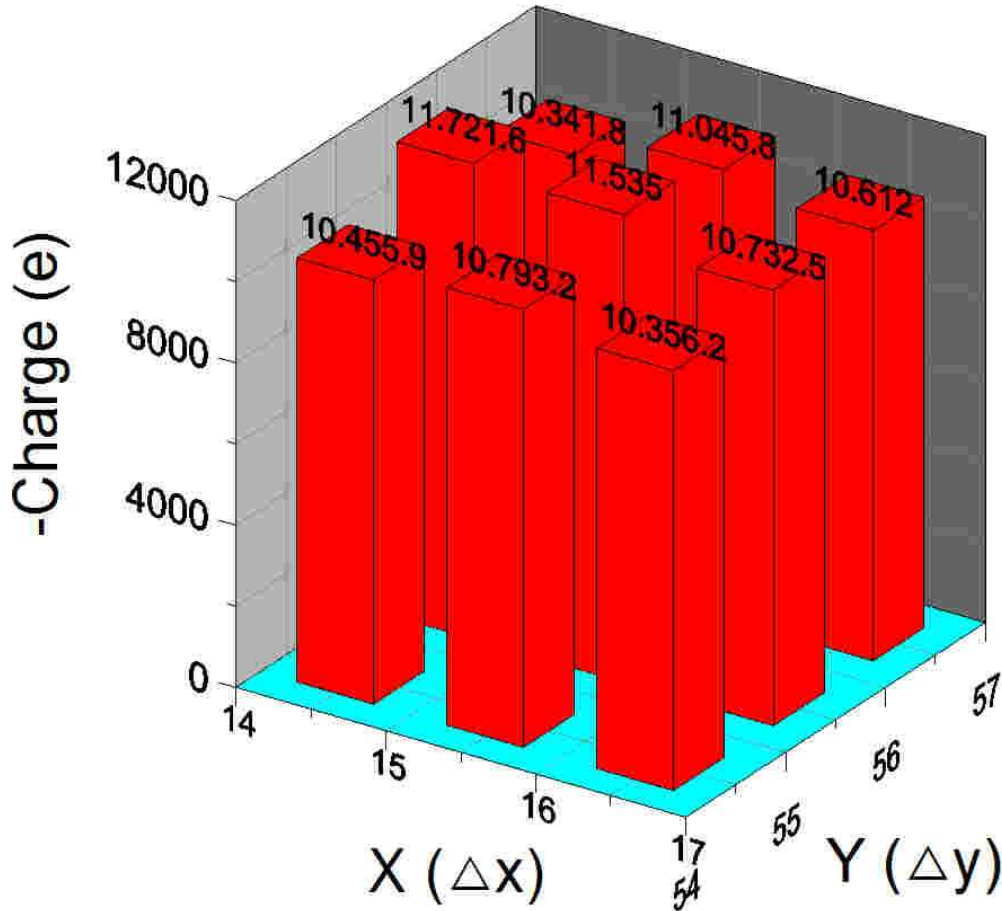
Figure 7.12: Computed dust charges for nine dust particles located in the plasma bulk (b=186 μm)

Figures 7.12 and 7.13 show the computed dust charge values of the nine dust particles located in the bulk and in the presheath. At either location, the dust charge on all nine particles is almost the same and is approximately equal to the single dust particle case, which is about 10500e in the bulk and about 11100e in the presheath. It means that the plasma species density is enough to charge all the particles to the single

particle value. We probably have still enough plasma supplied from the Z-direction and the neighborhood of the dust.
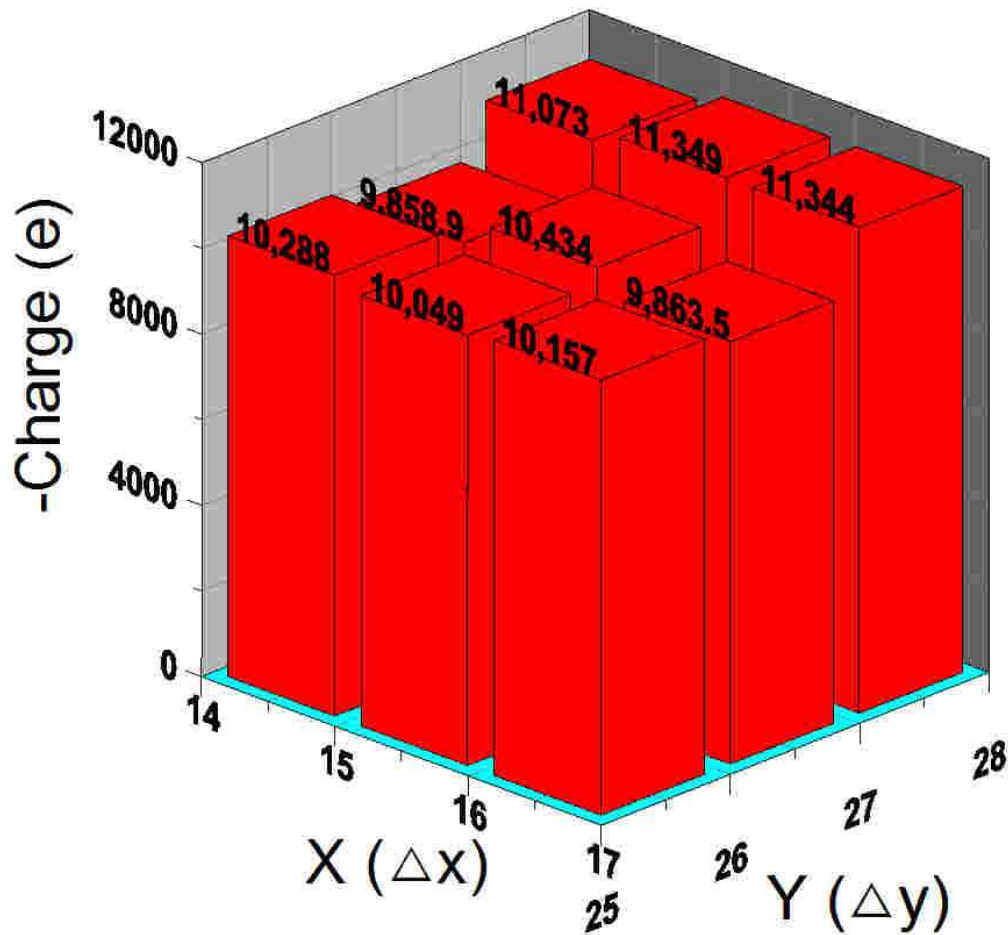
Figure 7.13: Computed dust charges for nine dust particles located in the presheath (b=186 μm)

In Fig. 7.14, the dust charge values computed for nine dust particles located in the sheath are presented. Here, the dust separation distance in either direction is 186 μm. It can be seen that the dust charges on the three dust particles in a single Y-layer is approximately equal. But the dust charge reduces drastically in the layers towards the electrodes. The dust charge on the three dust particles in the uppermost Y-layer (Y=7.5 Δx) is slightly larger than the dust charge value in the single particle case in the sheath which is about 6400e. This slight increase is due to the higher Y-position of the dust particle than in the single particle case, which is Y = 6.5Δx. In the central layer, where Y=6.5 Δx, the charge reduces almost to half of the single particle value and in the lower layer the charge reduces even further. The cause of this charge reduction will

be discussed in detail later.
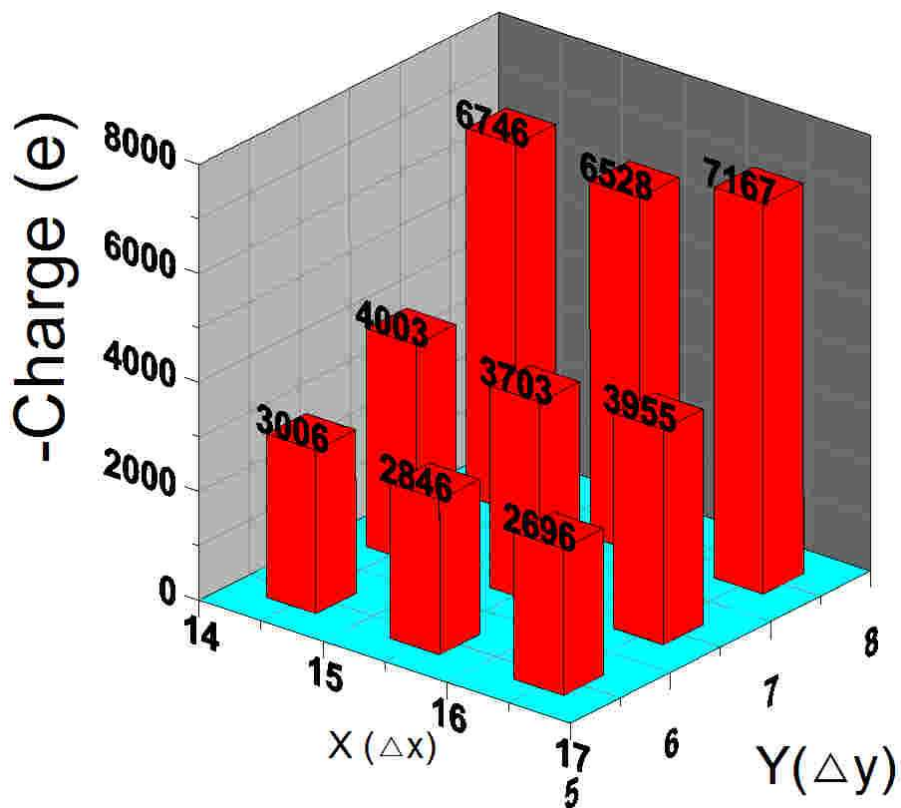
Figure 7.14: Computed dust charges for nine dust particles located in the sheath for a dust separation of $b = 186$ μm
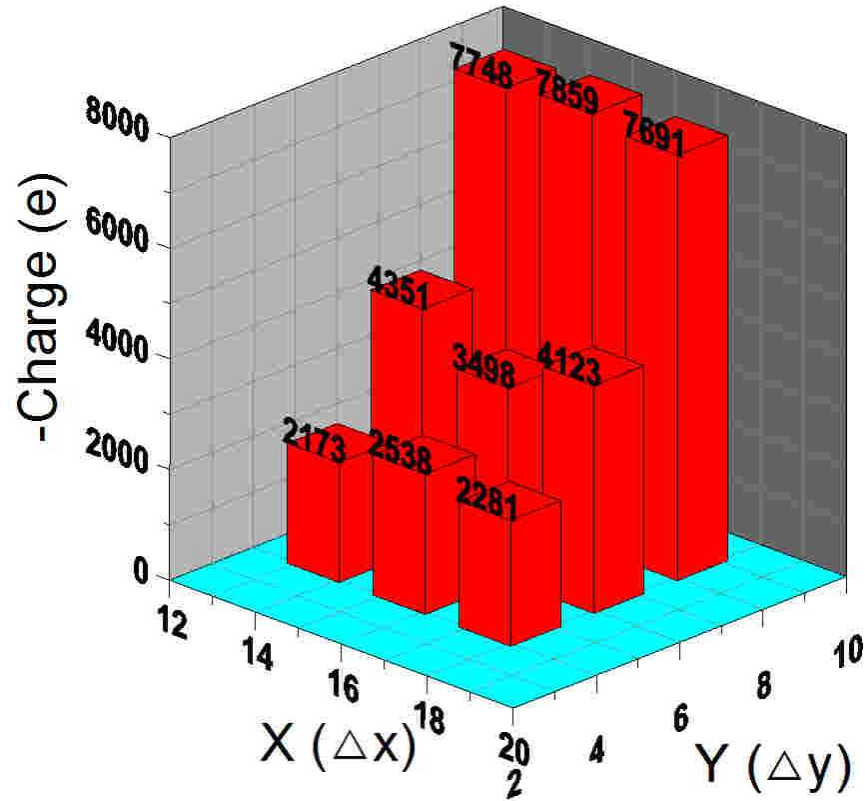
Figure 7.15: Computed dust charges for nine dust particles located in the sheath for a dust separation of $b = 372$ μm

The dust separation of 186 μm is smaller than the typical dust separation distances in the Yukawa balls [28], which is around 300 μm. Hence, we have studied the charging dynamics of multiple particles for the dust separation of 372 μm. The results for this case is shown in Fig. 7.15. The computed charge values follow the same trends as in the case of dust separation of 186 μm, i.e., the dust charge on the dust particles in the uppermost Y-layer is slightly larger than the single particle case value and the charge reduces drastically for the layers towards the electrodes. This charge reduction can be explained as follows: Figure 7.16 shows the computed ion and electron density profiles for the cases of single dust particle and multiple dust particles in the sheath. It can be seen that the electron density in both the cases is the same, but the ion density is different. The ion density between the electrode and the uppermost Y-layer of the dust particles is higher than that of the single dust particle case. Also, the ion density increases from the uppermost Y-layer towards the electrode. This enhancement in the ion density is due to the focusing of ions close to dust particles in each Y-layer. The ion trajectories around the dust are deflected by the dust field and focussed below

the dust. Due to this ion focusing, the ion current to the dust particle in the middle and the lower Y-layers increases resulting in a smaller charge number on these dust particles, compared to the single particle case.
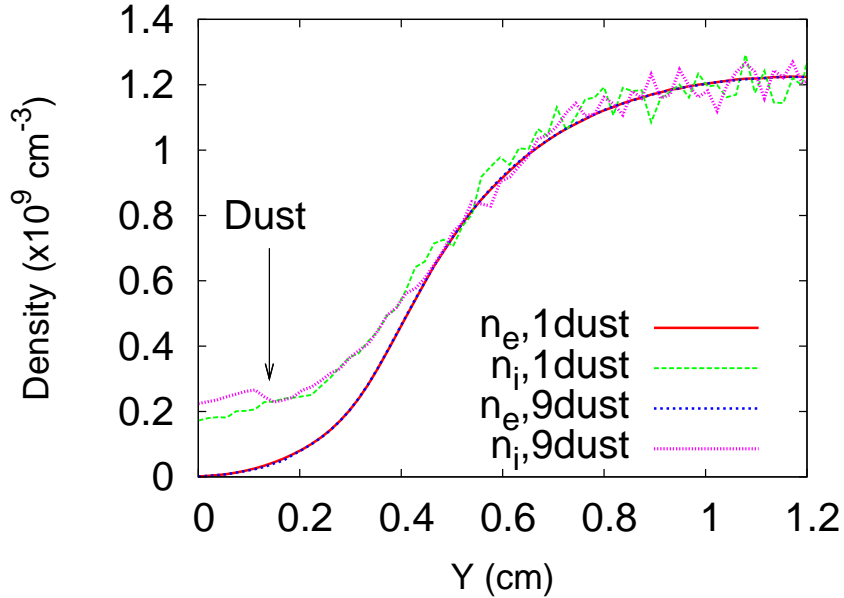
Figure 7.16: Computed electron and ion density profiles for single and multiple dust particle cases. Red/green lines indicate electron and ion densities in the single particle case and blue/pink lines indicate these densities for the nine dust particle case.

To Further support this, we have shown in Fig. 7.17, the ion density and velocity vectors in the XY-plane. It can be seen from the velocity vectors that the ions are deflected around the dust grains and are focussed below them. This results in enhancement of the ion density in a narrow stripe below the dust grains. This ion density increase can indeed be observed in the density colour plot. This focussing effect results in an increase of the ion flux to the lower grains, decreasing charge number on these grains. Such focussing effect is already seen in Fig. 6.7.

To compare this situation with the dust system in the presheath, similar analysis is done for the dust particle system in the presheath. Fig. 7.18 shows the ion density and velocity vectors in the XY-plane for the dust system in the presheath. Here, one can see that there is no strong focussing effect similar to the one observed in the sheath. This is because the ion velocity in the presheath is only about $0.12c_s$. Due to the lower kinetic energy of the ions in the presheath, the ion trajectories are strongly deflected in the dust field and the ions fall onto the dust grain getting absorbed. This is evident
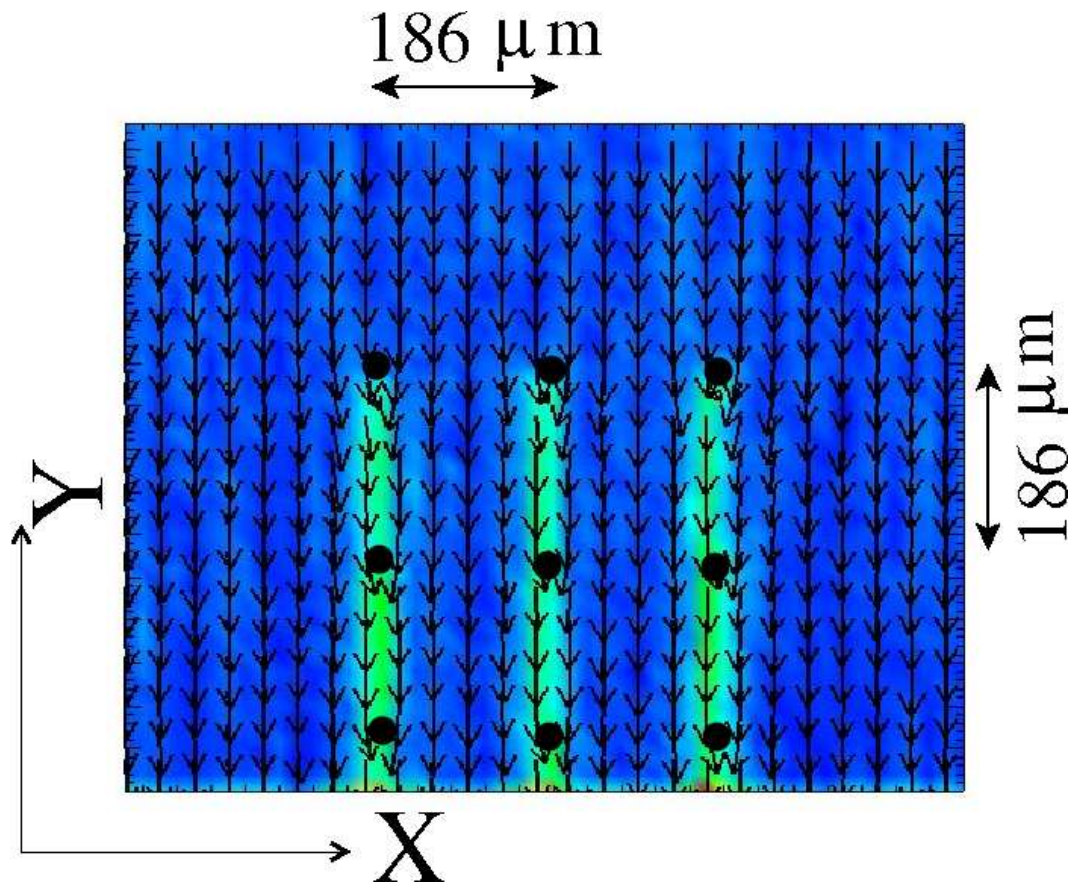
Figure 7.17: Ion density (color-coded) and velocities along xy-plane around the dust grains located in the sheath (b=186 μm & $\lambda_s = 320\mu$m)

from the fact that the ions very far from the dust particles are also being attracted towards the dust particles. This results in equal charge numbers on all the nine dust particles placed in the presheath.

7.5   Summary

Dust charge, potential and ion drag force on two dust particles are computed and compared with the single dust particle values. These dust parameters are computed for various interparticle separation distances and for dust particles placed at different locations in the rf discharge. It is found that for dust separations larger than the shielding lengths dust parameters for the two dust particles match with the single dust particle values. As the dust separation is equal to or less than the shielding length, the ion drag forces increase due to buildup of parallel drag force component. But,
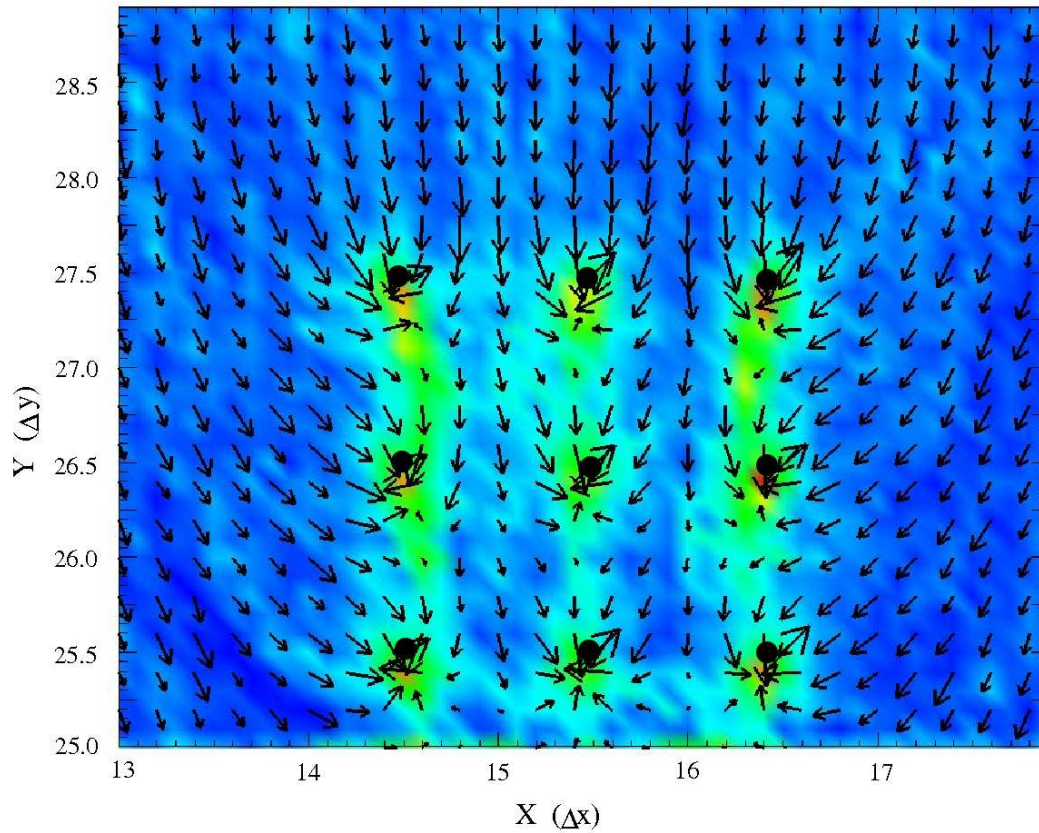
Figure 7.18: Ion density (color-coded) and velocities along xy-plane around the dust grains located in the presheath (b=186 μm & $\lambda_s = 320\mu$m)

other dust parameters are not found to be affected considerably. Dust charge and potential on multiple dust particles located at different positions in the discharge and arranged along the discharge direction are also computed. It is found that the dust charge and potential do not differ much from the single particle values for the bulk and the presheath. But the dust charges of multiple dust particles located in the sheath differ from the single dust parameter values. Due to ion focusing of dust particles in the upper layers, the ion current increases towards the dusts in lower layers resulting in smaller charge values.

Chapter 8

Summary and Outlook

Knowledge of dust charge, floating potential, shielding and ion drag force is very crucial for explaining complex laboratory dusty plasma phenomena, such as void formation in microgravity experiments and wakefield formation in the sheaths. Existing theoretical models assume standard distribution functions for plasma species and are applicable over a limited range of flow velocities and collisionality for quantifying dust parameters. Kinetic simulations are suitable tools for studying dust charging, drag force computation and the mechanism of interaction of different dust grains. The main aim of this thesis is to address the following issues, by three dimensional simulations using P^3M code:

- What is the effect of collisions among plasma species on discharge characteristics and thereby on charging dynamics and ion drag force?

- How do parameters like charge, floating potential, shielding length, and the ion drag force on dust vary for different positions of dust in rf discharges?

- How do values from various analytical models of dust charge and ion drag force compare with computational results for realistic discharge conditions?

- How do the dust charge, floating potential and ion drag force on the dust evolve in the presence of neighboring dust particles?

At first, rf discharges in argon have been modelled using the three-dimensional PIC-MCC code for the discharge conditions relevant to the dusty plasma experiments. All necessary elastic and inelastic collisions have been considered. The plasma background is found collisional, charge-exchange collisions between ions and neutrals being dominant. Electron and ion distributions are non-Maxwellian: electrons behave

Druyvesteyn-like and ions are subsonic even in the sheath due to CX collisions. The dominant heating mechanism for electrons is Ohmic heating.

Then, simulations have been done to address the first three issues above. Dust particles of different sizes are placed in the rf discharge simulation and the relevant dust parameters (dust charge, floating potential, ion drag force, shielding lengths) have been computed, for the first time, accounting for the plasma background realistic to experimental conditions. Dust charge and floating potential in the presheath are slightly larger than the values in the bulk due to the higher electron flux to the dust particle in the presheath. From presheath to the sheath the charge and floating potential values decrease due to the decrease of the electron current to the dust. A linear dependence of the dust potential on dust size has been found, which results in a nonlinear dependence of the dust charge with the dust size when the particle is assumed to be a spherical capacitor. This has been verified by independently counting the charges collected by the dust, where indeed it has been noted that the dust charge scales nonlinearly with the dust size. Simulated dust floating potentials are comparable to values obtained from ABR and Khrapak models, but much smaller than the values obtained from OML model. Simulated floating potentials are comparable to values obtained from Zobnin's model but slightly smaller, due to the depletion of high energy electrons in Druyvesteyn-like distributions compared to Maxwell's distribution. The dust potential distribution behaves Debye-Hückel-like. The shielding lengths are in between ion and electron Debye lengths, indicating shielding by both ions and electrons.

Further collection and orbital drag forces have been computed for various sizes of dust located in rf discharges for different discharge pressures. For the collisionless case, the computed drag force agrees with the drag values obtained from Hutchinson's work. The orbital drag force is typically larger than the collection drag force. The total drag force for the collisional case is larger than for the collisionless case and it scales nonlinearly with the dust size. The collection drag values and size-scaling agrees with the Zobnin's model. With an increase in pressure from 50 Pa to 100 Pa, the drag force does not vary considerably, the variation being within the numerical error bar.

The charging and drag force computation is then extended to two and multiple static dust particles in the rf discharge to address the last issue above. The dust parameters on the two dust particles are computed for various interparticle separation distances and for dust particles placed at different locations in the rf discharge. It is observed that for dust separations larger than the shielding lengths the dust parameters for the two dust particles match with the single dust particle values. As the dust separation is

equal to or less than the shielding length at that location the ion drag force increases due to the buildup of a parallel drag force component. However, the main dust properties like charge, potential, vertical component of ion drag are not affected considerably. This is because the collection impact parameter values in the sheath and the presheath are smaller than the smallest dust separation and in case of the dust in the bulk, the collection impact parameter is comparable with the dust separation.

The dust charges on multiple dust particles located at different positions in the discharge and arranged along the discharge axis are also computed. We believe these computations are first of their kind, where charging of multiple dust particles is studied for realistic plasma background conditions. It is found that the charges on the multiple dust particles in the bulk or presheath do not differ much from the single particle values at that location. But the dust charges of dust particles located in the sheath drastically differ from the single dust parameter values. Due to ion focusing from dust particles in the upper layers, the ion current increases to dust particles in the lower layers resulting in smaller charge values. This is as well the case where dust particles are vertically aligned as in the standard experiments of dusty plasmas.

Kinetic simulations are powerful tools for studying many basic phenomena which can be complementary to analytical models or experiments. In future P^3M/PIC models can be used to address other phenomena in dusty plasmas. Some of the possible studies are the following.

One obvious extension is to do the dynamic simulation without fixing the positions of the dust particles. The study can also be extended to understand the dust charging and drag force of the dust in magnetic/electromagnetic fields. Dust charging or decharging under UV radiation can be studied. Wake-field formation and interaction of other dust particles with the wake fields can be studied. Furthermore dust charging due to secondary emission by electrodes can also be studied. Multiscale simulations involving combined simulations with P^3M and fluid codes can be performed to study real experiments like microgravity experiments. Moreover, transport coefficients from P^3M code can serve as input to fluid codes which can be used to study these experiments on macroscales.

Appendix A

IEDs in Ar-CH$_4$ discharges

A.1   Introduction

Capacitively coupled radio-frequency (rf) discharges are frequently used for deposition and etching of thin films on a substrate attached to one of the electrodes [32]. The commonly used frequency in such experiments is 13.56 MHz and voltages are up to a few kV with typical electrode separations of 1-10 cm. These discharges are usually operated at pressures in the range between 2 and 150 Pa. Low pressures are used for etching, higher pressures for deposition [164]. For etching purposes, the substrate is mostly attached to the powered electrode; for deposition to the grounded or powered electrode. Discharges in an Argon-Methane gas mixture are especially used for hydrocarbon film or diamond-like carbon (DLC) film deposition [165]. In such processing plasmas, the ion energy distributions (IEDs) at the target substrate are crucial in determining the quality of the film, e.g., in terms of its anisotropy [166–168]. For that reason, measurement and design of IEDs receives great attention. A lot of techniques have been used to measure IEDs [169–175]. Meichsner, et.al. [176] performed experiments in which IEDs of various ion species in Ar/CH$_4$ gas mixture have been measured at the electrodes using an ion extractor unit [177]. This extracts the ions electrostatically and transfers them with an ion optics system to an energy analyzer. Usually, just the bias-voltage applied across the extractor system is subtracted from observed IEDs to derive IEDs at electrode. But, the effect of such ion extractor system on the IEDs obtained at an electrode has not yet been studied in detail. Depending on the magnitude of bias-voltage and size of extractor system, it might even entirely modify the structure of IED profiles at the electrode. Also, the system's effect might

vary with mass of ion species. Hence, it is necessary to study the effect of the ion extractor system on IEDs obtained at an electrode. A self-consistent one-dimensional Particle-in-Cell (PIC) code has been used to give better insight into the principle of operation of such an ion extractor unit to measure IEDs at the powered electrode. The effects of the ion transfer optics and the modulation effects of the potential within the ion extractor unit has been studied. In addition, the role of the ion optics behind the powered electrode is studied, especially with respect to the influence of the ion extraction voltages in the ion optics on the measured ion distributions. The analysis will be performed for different ion species to identify the role of molecule mass.

In section 2 the experiments are presented. The PIC code used in the simulations is described in section 3 and a basic characterization of the discharges is given in section 4. The simulation results are presented in section 5, discussing the different effects affecting the ion extractor diagnostics. Section 6 summarizes the results.

A.2   Brief review of the experiment

The experiment that will be modeled here, has been performed in a discharge arrangement [177], which consists of a circular stainless steel electrode with 9 cm in diameter and the grounded wall of the chamber. The electrode was powered by the rf-generator at 13.56 MHz and a fully tuneable π-type matching network. Due to the capacitive coupling and the larger effective surface of the grounded electrode an asymmetric rf discharge was created in an Ar/CH$_4$ mixture. At total pressure of 3 Pa and 5 Pa as well as a total gas flow rate of 4 sccm and 8 sccm a mixture of Argon (Ar) and Methane (CH$_4$) with a ratio of 1:3 was used by varying fluxes of the individual gases. The power input between 10 and 20 W in the applied pressure range is connected with the formation of negative self-bias voltages from 400 V up to about 500 V at the powered discharge electrode. The electron and ion dynamics in the sheath of asymmetric, capacitively coupled rf discharges determines strongly the ion energy distribution at the electrode surface [177, 178].

The ion analysis of the incident positive ions on the rf electrode is carried out using a differentially pumped mass spectrometer system, sampling through a 100 μm aperture in the rf powered electrode (see Fig. A.1). Using this spectrometer, mass and energy resolved measurements of positive ions from Ar-Methane plasma were obtained. This experiment provides one of the very few examples where the IED is measured at
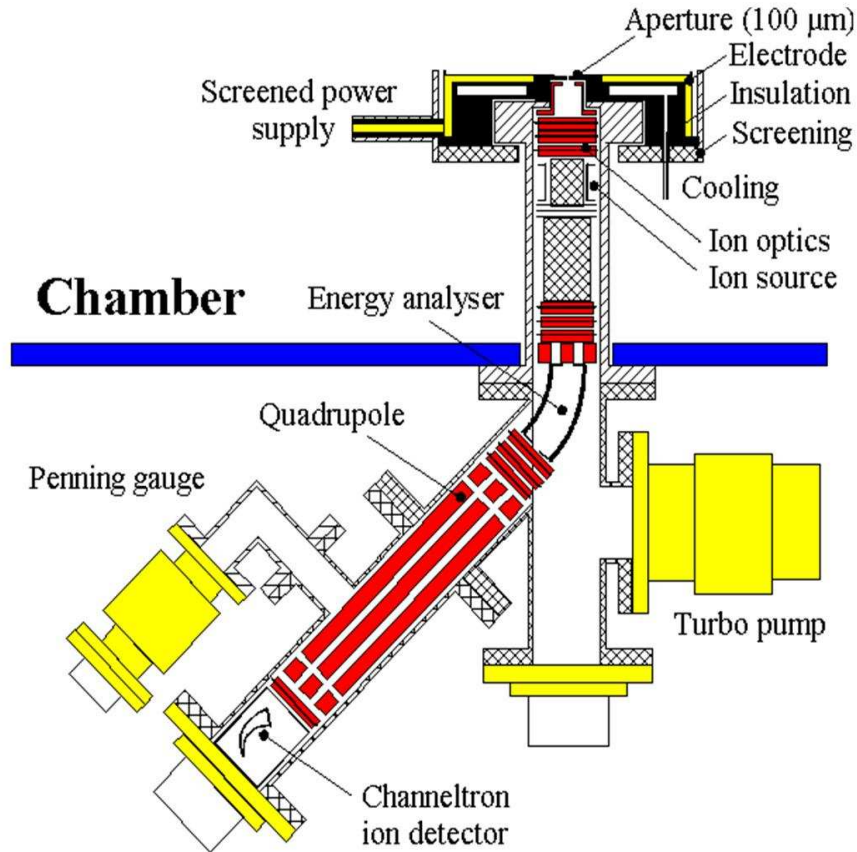
Figure A.1: Experimental setup for ion analysis. The upper electrode and the discharge vessel are not shown.

the powered electrode. The mass spectrometer system consists of ion optical elements, an electron impact source for post ionization of neutrals, an electrostatic sector field analyzer (1000 eV, $\Delta E = 0.7$ eV), a triple quadrupole mass filter (300 amu) and a gated channeltron electron multiplier. An energy scan is done at a constant pass energy through the energy analyzer by shifting the reference potential of the spectrometer, so that stable ions are accelerated or decelerated to equal pass energy [177]. In this way, energy dependent transmissions only affect the front region of the system. The aperture plate of the mass spectrometer is at the same voltage as the powered electrode. Consequently, an electric field is acting between the aperture plate and the first ion optical element (extractor), which modulates the energy distribution. Therefore, one does not measure the IEDs at the rf electrode surface due to the plasma boundary sheath, but the IED modified by this modulation. Here the question arises in how far

the IED is affected by the residence time of the ion in the rf field in the gap between
the aperture and the extractor.

Table A.1: List of collisions included

No.	Collision	Reference
	Coulomb Collisions:	
01	e-e Coulomb	[156]
02	e-i coulomb for 9 ion species	[156]
03	i-i coulomb for 9 ion species	[156]
	Electron-Neutral Elastic Collisions:	
04	e-Ar	[157]
05	e-CH$_4$	[157]
06	e-H$_2$	[157]
07	e-H	[157]
	Ion-Neutral Elastic Collisions:	
08	Ar$^+$ - Ar	[157]
09	Ar$^+$ - CH$_4$	[157]
10	CH$_4{}^+$ - Ar	[157]
11	CH$_4{}^+$ - CH$_4$	[157]
12	CH$_3{}^+$ - Ar	[157]
13	CH$_3{}^+$ - CH$_4$	[157]
14	ArH$^+$ - CH$_4$	[157]
15	ArH$^+$ - CH$_3$	[157]
16	ArH$^+$ - Ar	[157]
17	H$^+$ - CH$_4$	[157]
18	H$^+$ - Ar	[157]
19	H$_2{}^+$ - CH$_4$	[157]
20	H$_2{}^+$ - Ar	[157]

table continued...

No.	Collision	Reference
Inelastic Collisions:		
Ionization Collisions:		
21	$e + Ar \rightarrow Ar^+ + 2e$	[157]
22	$e + CH_4 \rightarrow CH_4^+ + 2e$	[179]
23	$e + CH_3 \rightarrow CH_3^+ + 2e$	[179]
24	$e + CH_2 \rightarrow CH_2^+ + 2e$	[179]
25	$e + CH \rightarrow CH^+ + 2e$	[179]
26	$e + C \rightarrow C^+ + 2e$	[179]
27	$e + H_2 \rightarrow H_2^+ + 2e$	[180]
28	$e + H \rightarrow H^+ + 2e$	[180]
Dissociation Collisions:		
29	$e + CH_4 \rightarrow CH_3 + H + e$	[179]
30	$e + CH_3 \rightarrow CH_2 + H + e$	[179]
31	$e + CH_2 \rightarrow CH + H + e$	[179]
32	$e + CH \rightarrow C + H + e$	[179]
33	$e + H_2 \rightarrow H + H + e$	[180]
34	$e + CH_4^+ \rightarrow CH_3 + H^+ + e$	[179]
35	$e + CH_4^+ \rightarrow CH_3^+ + H + e$	[179]
36	$e + CH_3^+ \rightarrow CH_2 + H^+ + e$	[179]
37	$e + CH_3^+ \rightarrow CH_2^+ + H + e$	[179]
38	$e + CH_2^+ \rightarrow CH + H^+ + e$	[179]
39	$e + CH_2^+ \rightarrow CH^+ + H + e$	[179]
40	$e + CH^+ \rightarrow C + H^+ + e$	[179]
41	$e + CH^+ \rightarrow C^+ + H + e$	[179]
Dissociation with Ionization collisions.:		
42	$e + CH_4 \rightarrow CH_3^+ + H + 2e$	[179]
43	$e + CH_4 \rightarrow CH_2^+ + 2H + 2e$	[179]

table continued...

No.	Collision	Reference
44	e + CH$_4$ → CH$^+$ + 3H + 2e	[179]
45	e + CH$_3$ → CH$_2^+$ + H + 2e	[179]
46	e + CH$_2$ → CH$^+$ + H + 2e	[179]
47	e + CH → C$^+$ + H + 2e	[179]
48	e + CH → C + H$^+$ + 2e	[179]

Dissociation with

electron-recombination collisions:

No.	Collision	Reference
49	e + CH$_4^+$ → CH$_3$ + H	[179]
50	e + CH$_4^+$ → CH$_2$ + 2H	[179]
51	e + CH$_3^+$ → CH$_2$ + H	[179]
52	e + CH$_2^+$ → CH + H	[179]
53	e + CH$^+$ → C + H	[179]

Charge-exchange collisions:

No.	Collision	Reference
54	H$^+$ + CH$_4$ → H + CH$_4^+$	[179]
55	H$^+$ + CH$_3$ → H + CH$_3^+$	[179]
56	H$^+$ + CH$_2$ → H + CH$_2^+$	[179]
57	H$^+$ + CH → H + CH$^+$	[179]
58	H$^+$ + C → H + C$^+$	[179]
59	H$^+$ + H → H + H$^+$	[179]
60	H$^+$ + H$_2$ → H + H$_2^+$	[179]
61	H$^+$ + Ar → H + Ar$^+$	[157]
62	H$_2^+$ + CH$_4$ → H$_2$ + CH$_4^+$	[179]
63	H$_2^+$ + Ar → H$_2$ + Ar$^+$	[157]
64	H$_2^+$ + H$_2$ → H$_2$ + H$_2^+$	[181]
65	CH4$^+$ + CH$_4$ → CH$_4$ + CH$_4^+$	[157]
66	CH3$^+$ + CH$_3$ → CH$_3$ + CH$_3^+$	[157]

table continued...

No.	Collision	Reference
	Excitation collisions:	
67	$e + Ar \rightarrow Ar^* + e$	[157]
68	$e + H_2(\nu{=}0) \rightarrow e + H_2(\nu{=}1)$	[180]
69	$e + H_2(J{=}0) \rightarrow e + H_2(J{=}2)$	[180]
70	$e + H_2(J{=}1) \rightarrow e + H_2(J{=}3)$	[180]
71	$e + H_2(X^1\Sigma_g^+) \rightarrow e + H_2(b^3\Sigma_u^+)$	[180]
72	$e + H_2(X^1\Sigma_g^+) \rightarrow e + H_2(B^1\Sigma_u^+)$	[180]
	Others:	
73	$Ar^+ + H_2 \rightarrow ArH^+ + H$	[182]

A.3   Method of computation

To simulate the experimental conditions, we have used a one-dimensional particle-in-cell (1D PIC-MCC) code, which is described in detail in [145, 146]. Here, kinetics of 'super particles', which represent many real particles, moving in self-consistent fields discretized on a grid are followed. The collisions between particles are modeled using a binary Coulomb collision model described in [146, 156]. The PIC code allows to self-consistently resolve the whole plasma including the electrostatic sheath in front of the material wall, which governs the ion acceleration and thereby governing the IEDs of species. The code delivers spatial and temporal variation of plasma parameters and velocity distributions of various species which can be used to calculate IEDs. The collisions implemented for Ar/CH_4 gas mixture include all relevant processes and are listed in the Table A.1. The standard PIC-MCC code [146] has been modified to incorporate additional collisional processes. Also, it has been modified to include an additional computational grid to simulate the ion extractor system.

This PIC code was used to simulate rf discharges in Ar/CH_4 gas with the parameters listed in Table A.2. The parameters were chosen to match the experimentally observed bias voltages. The electrode separation is taken as 4 cm. The background gas temperature is taken as 300 K. The neutral densities were taken as constant as

Table A.2: Discharge parameters used in experiments and simulations

Case	Total Pressure (Pa)	Ar Flux (sccm)	CH$_4$ flux (sccm)	rf power (W)	Self bias (Volt)	Voltage in simulation (Volt)
a	3	1	3	10	428	856
b	5	2	6	10	415	830
c	5	2	6	20	533	1066

measured in the experiments. 18 species are included in the model: e$^-$, H$^+$, H$_2^+$, C$^+$, CH$^+$, CH$_2^+$, CH$_3^+$, CH$_4^+$, Ar$^+$, ArH$^+$, H, H$_2$, C, CH, CH$_2$, CH$_3$, CH$_4$ and Ar. The PIC cell size has been taken as half of a Debye length. The time-step is calculated based on the electron plasma frequency [147].

Properties of the discharges

In this section we present the computational results obtained for the experimental cases listed in Table A.2. The global discharge properties, such as various species densities and distributions, govern the reactions and thereby the flux to electrodes or substrates. The simulations allow us to get a better insight into the basic physics in such discharges.

Figure A.2 shows the computed time-averaged electron and ion densities in the Ar/CH$_4$ discharges. The total ion density, as it should, satisfies quasi-neutrality in bulk and exceeds electron density in sheaths. The CH$_4^+$ density is dominating all other ion densities due to its higher neutral gas density. A second dominating species is unexpectedly ArH$^+$. The formation of ArH$^+$ is via collisions of Ar$^+$ ions with H$_2$ molecules, the reaction (see Table A.1, channel 73) which has no threshold.

Figure A.3 shows the time-averaged electron energy probability function (EEPF) computed for cases a and b. The distribution function deviates from a Maxwellian, but can be represented as a sum of two Maxwellian distributions, which reveals the existence of two groups of electrons: cold electrons in the middle of the system, and the tail of high-energy electrons oscillating between the electrodes due to stochastic heating [146]. Similar bi-Maxwellian electron distributions were experimentally found in low-pressure capacitive rf discharges [45]. The effect of the increase in pressure on EEPF is relaxation and transition into an ohmic heating regime. The high energy

population decreases and the low energy population increases [146, 183]. This is well reflected in our simulated EEPFs.
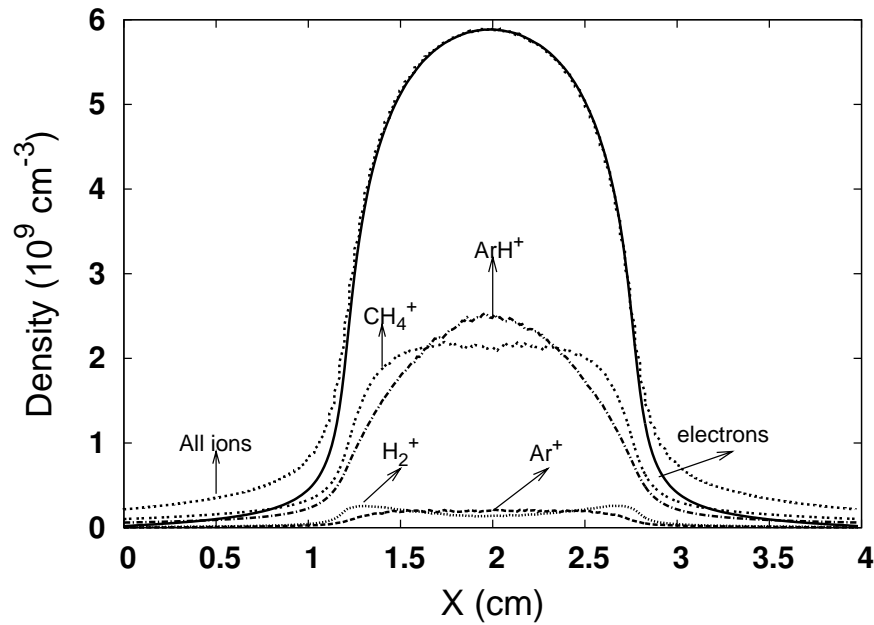
Figure A.2: Density of various plasma species in the CH_4-Ar discharge for the 5 Pa case as a function of position. X=0 cm corresponds to the grounded electrode and X=4 cm to the powered electrode.
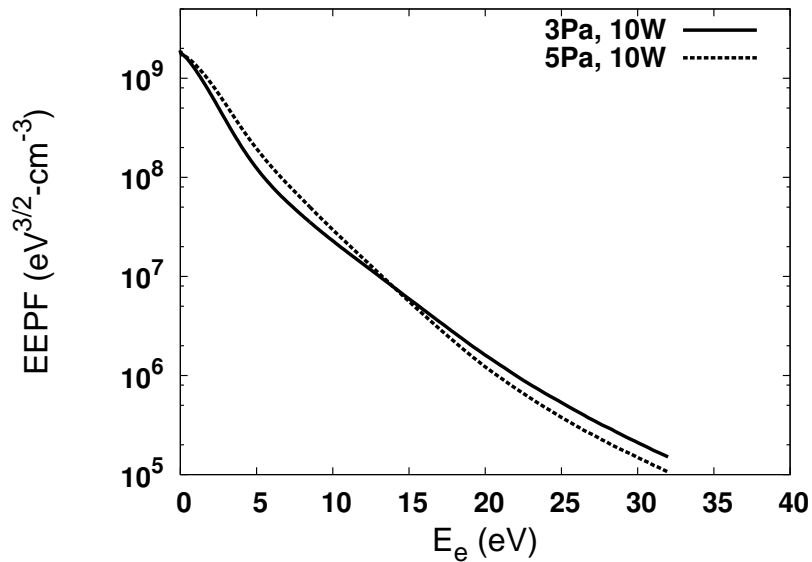
Figure A.3: Electron energy probability functions for cases a and b in Table A.2.

Ion transit times

The ion transit time (t_{ion}) through the sheath is an important parameter which governs the energetic structure of IEDs. The number of the secondary branches in IEDs corresponds to the number of rf periods that an ion takes to cross the sheath [155]. This number is equal to t_{ion}/t_{rf}. The ion transit time through a sheath of mean width s and mean potential drop V can be calculated [155] as $t_{ion} = 3s\,(M_{ion}/2eV)^{1/2}$, where M_{ion} is the mass of ion species.
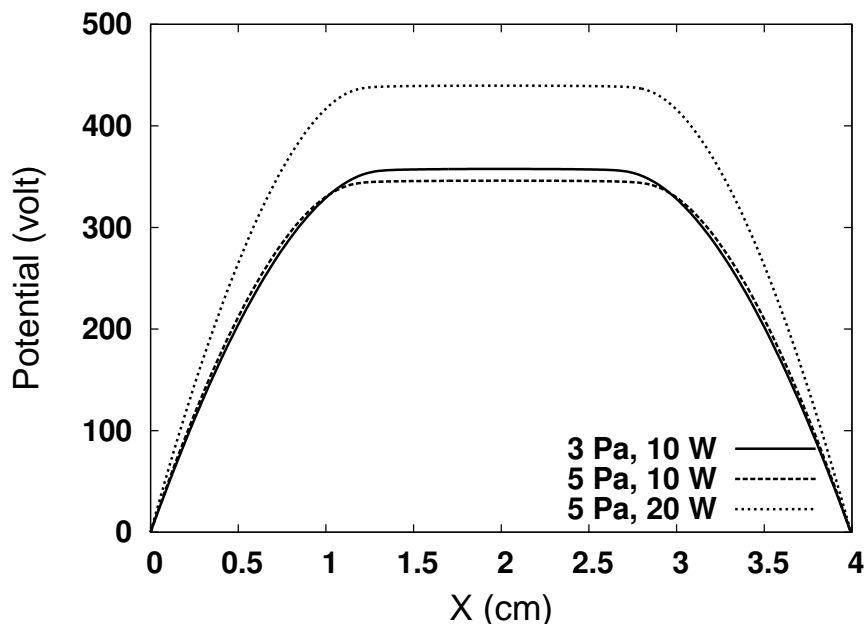
Figure A.4: Computed time-averaged potential in the system for three cases in Table A.2.

Figure A.4 shows the single rf-cycle averaged potential in the system for the three cases. The average potential drop in the sheath region and sheath width in these cases are listed in Table A.3.

For the computation of t_{ion} for all the cases, we take the single sheath width and potential drop which are equal to 7.5 mm and 400 V. Computed ion transit times 't_{ion}' for various ions are listed in Table A.4 .

These computed t_{ion}/t_{rf} values provide information about the number of secondary branches that can be expected in IEDs of each species. Light ions (H$^+$, H$_2^+$) take less than two rf cycles to traverse the sheath and hence only one or two secondary branches can be expected. Hydrocarbon species (CH$_3^+$, CH$_4^+$) take about 4.5 rf cycles to traverse the sheath and so 4 to 5 secondary branches can be anticipated. Similarly, for heavy

Table A.3: Computed average sheath potential drops and sheath widths.

case	Average sheath Potential drop (volt)	sheath width (mm)
a	370	7.98
b	360	6.52
c	450	7.99

species (Ar^+), 6 to 7 number of secondary branches are expected. For ArH^+ also this transit time analysis predicts 6 to 7 secondary branches, if reaction channels that form new ArH^+ ions such as charge-exchange reactions are relevant. In our model, charge-exchange collisions involving ArH^+ are not included (see Table A.1), as the reaction cross sections are not available. As the cross section of formation reaction of ArH^+ (Reaction #73) decreases exponentially with energy, this reaction channel also does not provide new ions in the sheath. Hence, the IED of ArH^+ will contain only the high energy saddle structure, in agreement with the experiments as shown in the next section.

A.4 Results

We now will compare the simulated ion fluxes with the measured IEDs for the different plasma conditions considered in the experiment. In the comparison of the experimental and simulated IEDs, the main quantities to be compared are the number of peaks in the distribution and the maximum ion energy. The absolute and the relative intensity of the peaks in the distribution function cannot be considered vigorously as the apparatus function, i.e. the energy dependence of the sensitivity for ion detection, is not known for this experimental setup. This consequently leads to differences in the simulated and measured peak heights.

Table A.4: Computed ion transit times through the sheath for various ions.

Ion	t_{ion}	t_{ion}/t_{rf}
	(nsec)	
H$^+$	81.2	1.1
H$_2^+$	114.9	1.56
CH$_3^+$	314.9	4.27
CH$_4^+$	325.4	4.41
Ar$^+$	487.9	6.62
ArH$^+$	495.0	6.71

Ion distributions at the powered electrode
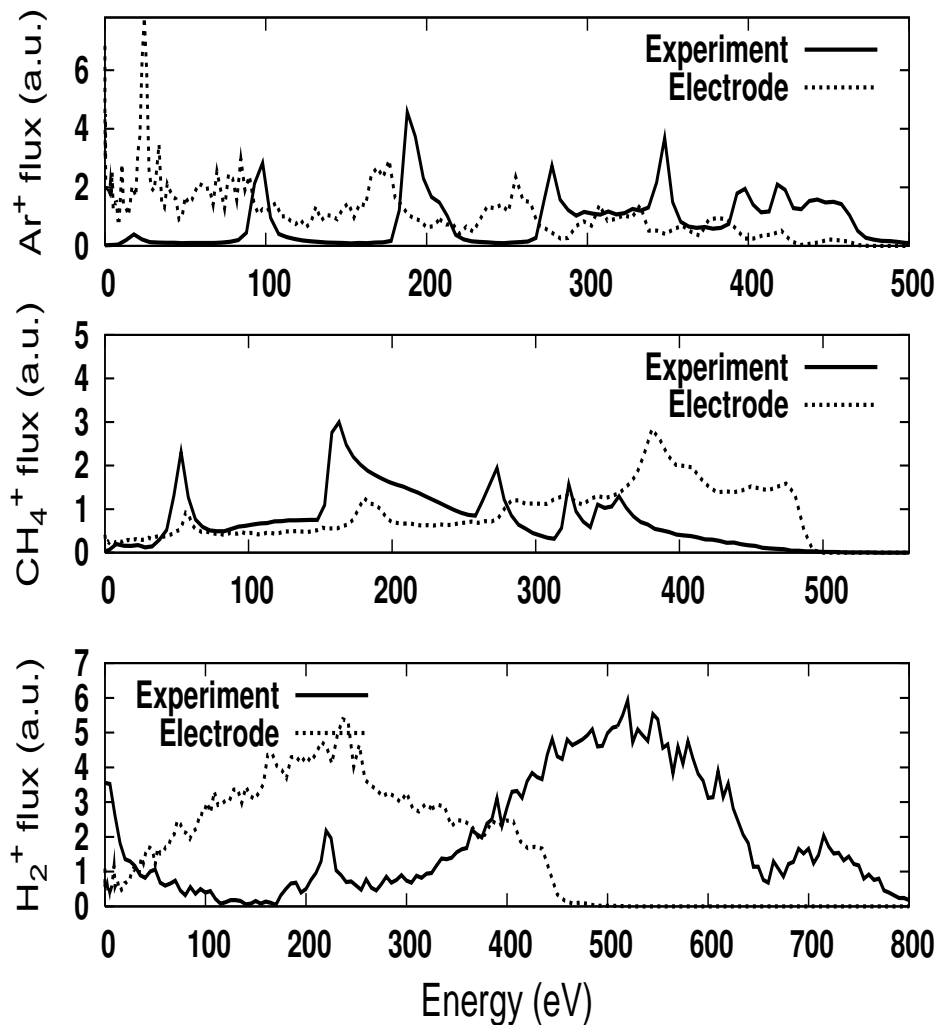
Figure A.5: Comparison of experimental and computed IED profiles for Ar$^+$, CH$_4^+$, H$_2^+$. In the simulation the IEDs are taken from the ion fluxes to the powered electrode.

The time averaged IEDs of various species at the powered electrode have been computed from the ion flux toward the powered electrode. These simulated ion distributions are then compared to the experimental observations. Figure A.5 shows comparisons between simulated and experimental IEDs of Ar^+ and CH_4^+ corresponding to the case c in Table A.2 and of H_2^+ corresponding to the case b. Elastic collisions influence the continuous part of the IED and charge-exchange collisions between ions and neutrals result in secondary branches in the calculated IEDs. It can be observed that the simulation and experimental results agree qualitatively in the number of secondary branches. However, the location of these secondary branches deviate from each other. In case of ArH^+ ions, the computed IED (as can be seen in Fig. A.7) consists of only high-energy saddle structure without any secondary branches, which matches with the experimental IED profile. It means that the elastic collisions included have week effect and reaction channels for formation of secondary branches (charge-exchange and formation of ArH^+ ions in the sheath) are not dominant. There is also a large discrepancy in the maximum ion energies between simulations and experiments, especially for H_2^+. To understand these discrepancies, the modulation effect within the ion-optics on the IEDs measured at powered electrode is considered in the following studies.

Effect of the ion optics on IEDs

The aperture plate (the entrance orifice of the ion energy analyzer) of the mass spectrometer is driven by the voltage of the powered electrode. Also, the extractor is biased at -31 V with reference to ground. Consequently, an rf electric field is existing between the aperture plate and the extractor, which further modulates the energy distribution originally created at the rf electrode surface due to the plasma boundary sheath. Ions emerging from the aperture experience this rf field and the ion energy gets modulated depending on the rf phase at which it enters the aperture similarly as the ions entering the sheath from the plasma. This modulation depends on the residence time of the ion in the rf field between the aperture and the extractor. To simulate the effect of the ion optics on the IEDs, a three-dimensional model would be necessary for the complete diagnostics system, which is far beyond the scope of this study. Approximating this effect in 1D, a characteristic drift length of the ion-optics system is introduced. It is this length (and also the ion mass) which determines the ion residence time in the rf field. Hence, it works like a characteristic collisionless drift length of the ion. Within this length, the ions hitting the powered electrode are followed further according to the

electric field determined by the rf sheath modulation and the applied bias voltage at the extractor. This distance is varied in the model until the best qualitative agreement between computed and experimental IEDs is found. We further made the assumption that all different ion species experience the same characteristic drift length.
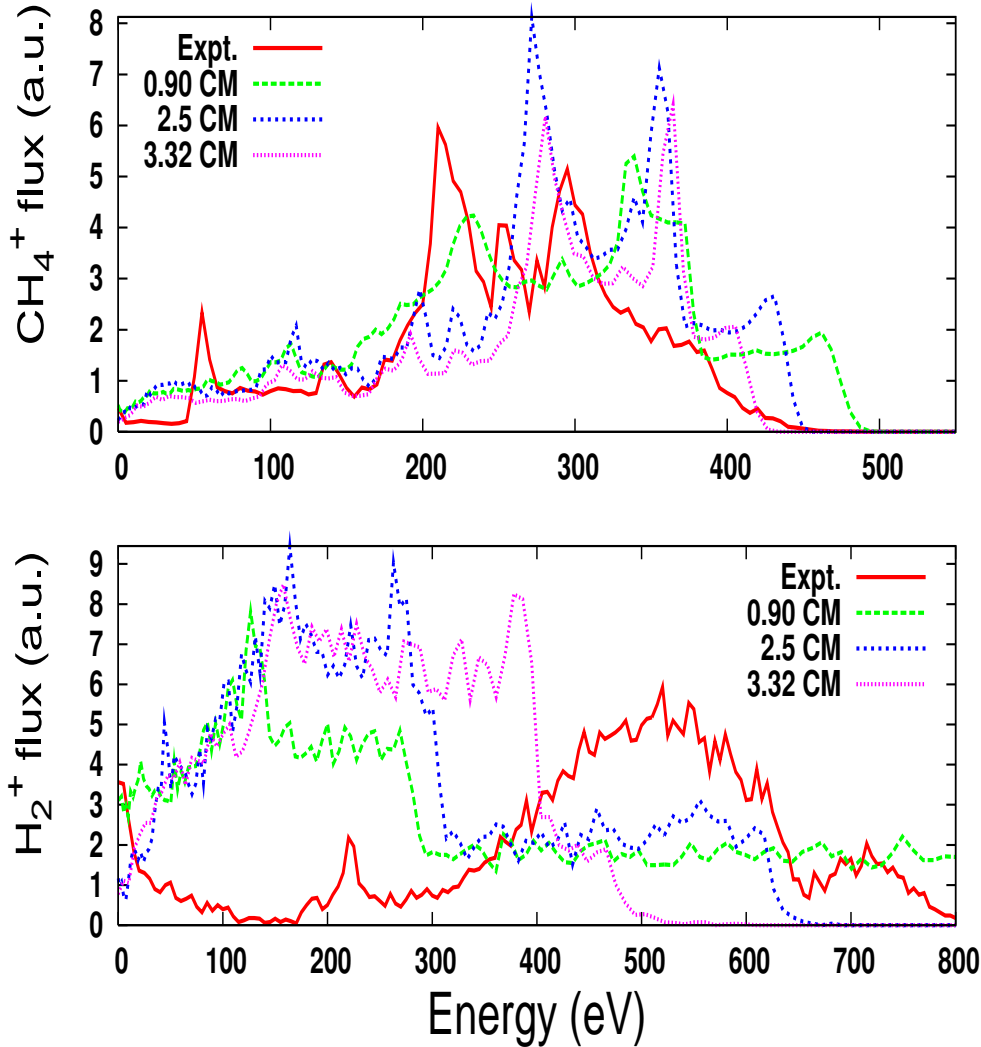
Figure A.6: Simulated IED profiles for CH$_4^+$, H$_2^+$ at the extractor for different extractor drift lengths.

In order to include the extractor system into the simulations, the PIC domain has been extended to the extractor. The length of this additional zone has been varied between 0.25 cm to 10.0 cm and modulated IEDs have been obtained at the extractor. Figure A.6 shows the modulated IEDs for CH$_4^+$ and H$_2^+$ ions for extractor lengths 0.90 cm, 2.5 cm and 3.32 cm. For extractor lengths less than 2.5 cm the observed additional

modification is very pronounced and not in agreement with the experimental profiles. For extractor lengths greater than 2.5 cm, there is a decent modification in computed IEDs at the electrode and we observe a better qualitative agreement than before. From that, we have chosen as the best fit a single characteristic drift length of 2.5 cm for all ions for further comparisons.
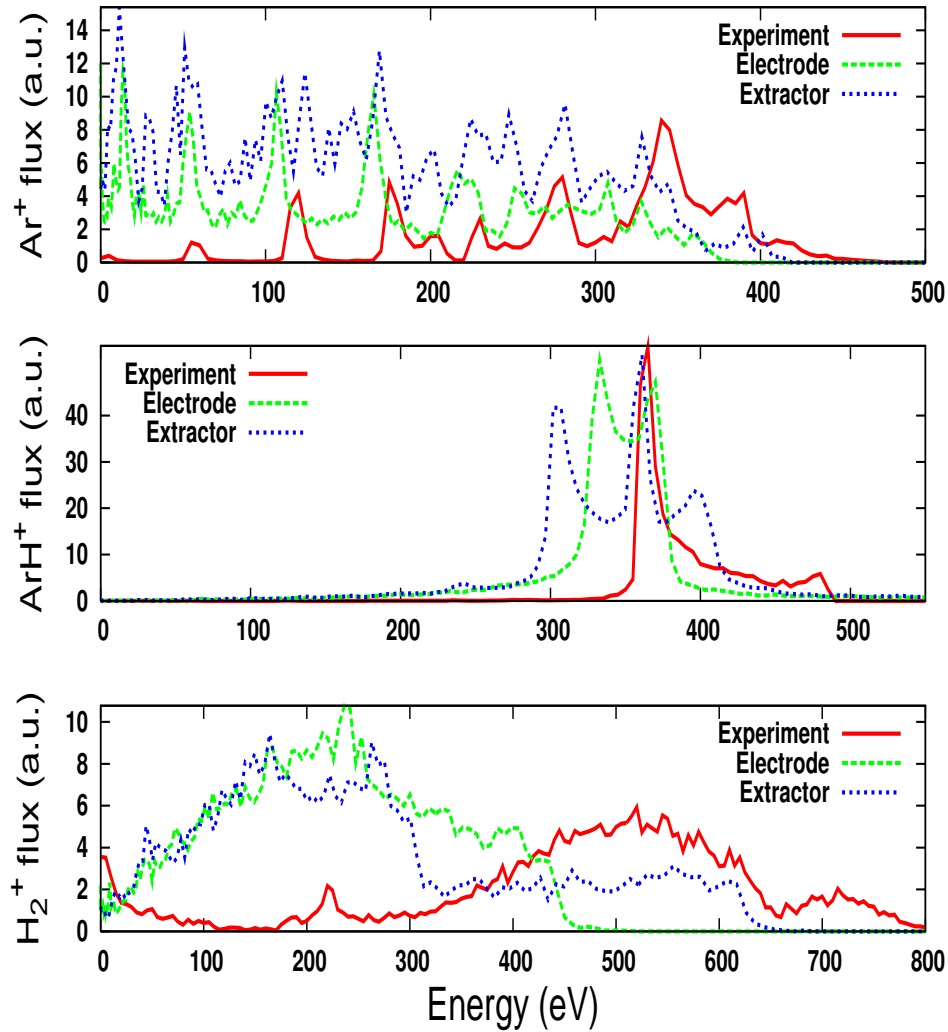
Figure A.7: Comparison of computed IEDs at electrode and extractor with experimental profile for Ar^+, ArH^+, H_2^+ ions.

Figures A.7 and A.8 show the computed IEDs at the electrode and the extractor with an extractor length of 2.5 cm for Ar^+, ArH^+, H_2^+ and CH_4^+, CH_3^+ ions for the cases a or b in Table A.2. In case of Ar^+ IED, the modification or modulation effect by the extractor is small. But, the location of secondary branches reasonably agree with those
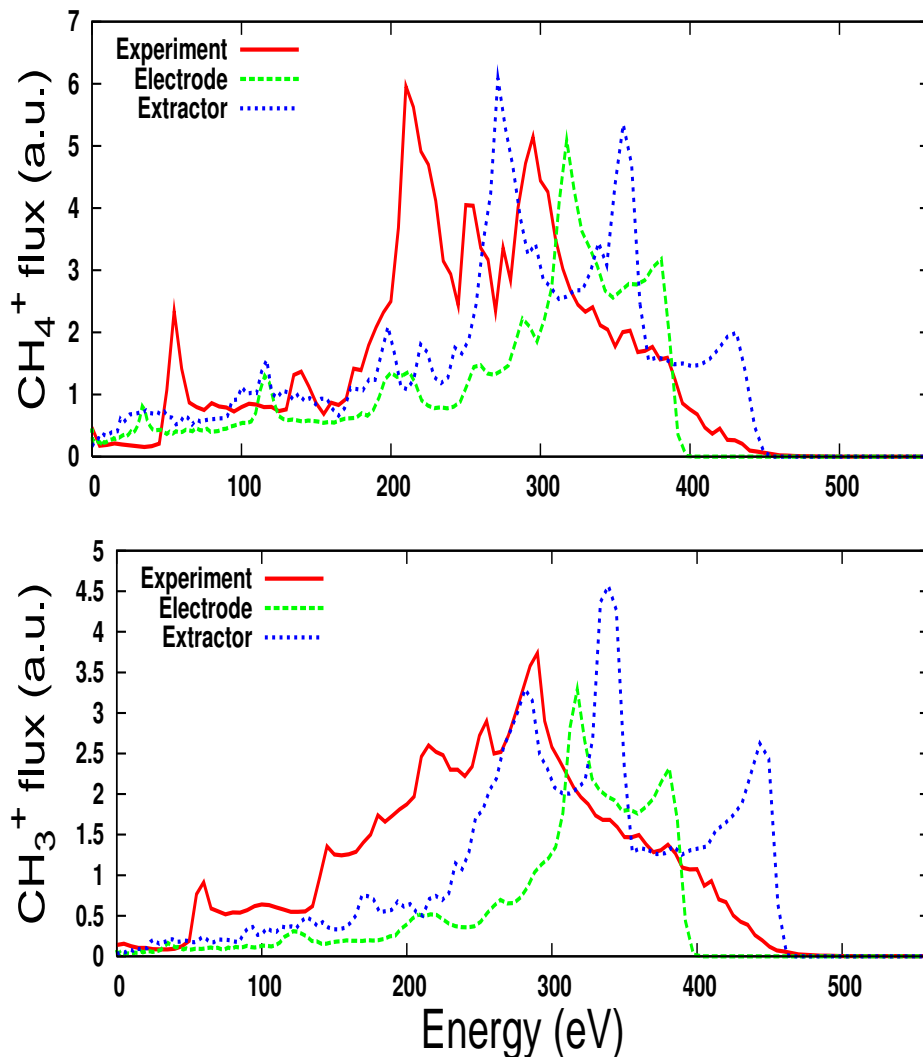
Figure A.8: Comparison of computed IEDs at electrode and extractor with experimental profile for CH$_4^+$, CH$_3^+$ ions.

in experimental IED profile. The modulation effect can clearly be seen in ArH$^+$ IED, as it consists of only saddle-structure. This saddle has been broadened and the width of modulated profile nearly matches with the width of experimental IED profile. The modulation effect is pronounced for H$_2^+$ ions, where the IED gets broadened by 200 eV. For hydrocarbon species, the modulation in IEDs is also considerable and the simulated high-energy peak structure resembles the experimental profile. The modulated IEDs at the extractor show a better match with experimental observations introducing this drift length effect. The mechanism of the rf modulation in the extractor can be explained as follows. It is similar to the modulation in sheaths of rf discharges, but for collisionless

transits in the extractor region. As the ion species are heavy, they experience only the average rf field and should form a single peak in the IEDs. This peak should appear at the average sheath potential drop. But, depending on the phase of the rf-modulated sheath field relative to the ion entrance into the sheath, the energy gets modulated and saddle shape occurs in IEDs around the average sheath potential drop as in collisionless sheaths. Similarly, the modulation in the extractor region results in a splitting or broadening of each peak from the IEDs at the electrode. This broadening effect can be observed in all IEDs at the extractor shown in Figs. A.7 and A.8, most pronounced in the case of ArH^+. The extent of broadening of a single peak of the IED at the electrode into the IED at the extractor depends on the residence time (t_{res}) of each ion species within the rf field existing in the extractor. The broadening is proportional to the ratio t_{rf}/t_{res}. As t_{res} is proportional to the square root of the ion mass, for a given t_{rf} the broadening is inversely proportional to the square root of the ion mass. That means that for lighter ions the broadening effect is larger and for heavier ions it decreases as can be seen in the calculated IEDs at the extractor: for the used extractor drift length of 2.5 cm the modulation effect is very pronounced for light ions (H_2^+), moderate for hydrocarbon ions and small for heavy ions (Ar^+, ArH^+) in agreement with the simple estimate.

The maximum energy obtained for all ions agree with the experimental values. Hydrocarbon species are reactive species and we suspect further reaction processes taking place within the ion diagnostics, which are clearly not included in our simplified description. Further support of this is given by the experimental IEDs for hydrocarbons, which do not show a sharp energy cut-off at high energies but a very long wing (Fig. A.9). Therefore, measurements of reactive species with such a diagnostics require additional parameter optimization in the experimental set-up to minimize such effects. Nevertheless, the interpretation of IEDs measured with an ion optics system is never a direct measurement of the IED at the electrode surface, but needs interpretation and back-mapping procedures for such a purpose.

A.5   Summary

The electrostatic extraction of ions through an aperture and extractor lens into the energy resolved mass spectrometer allows to measure the ion energy distribution functions at the discharge electrodes of capacitive rf plasma. A one-dimensional Particle-in-Cell
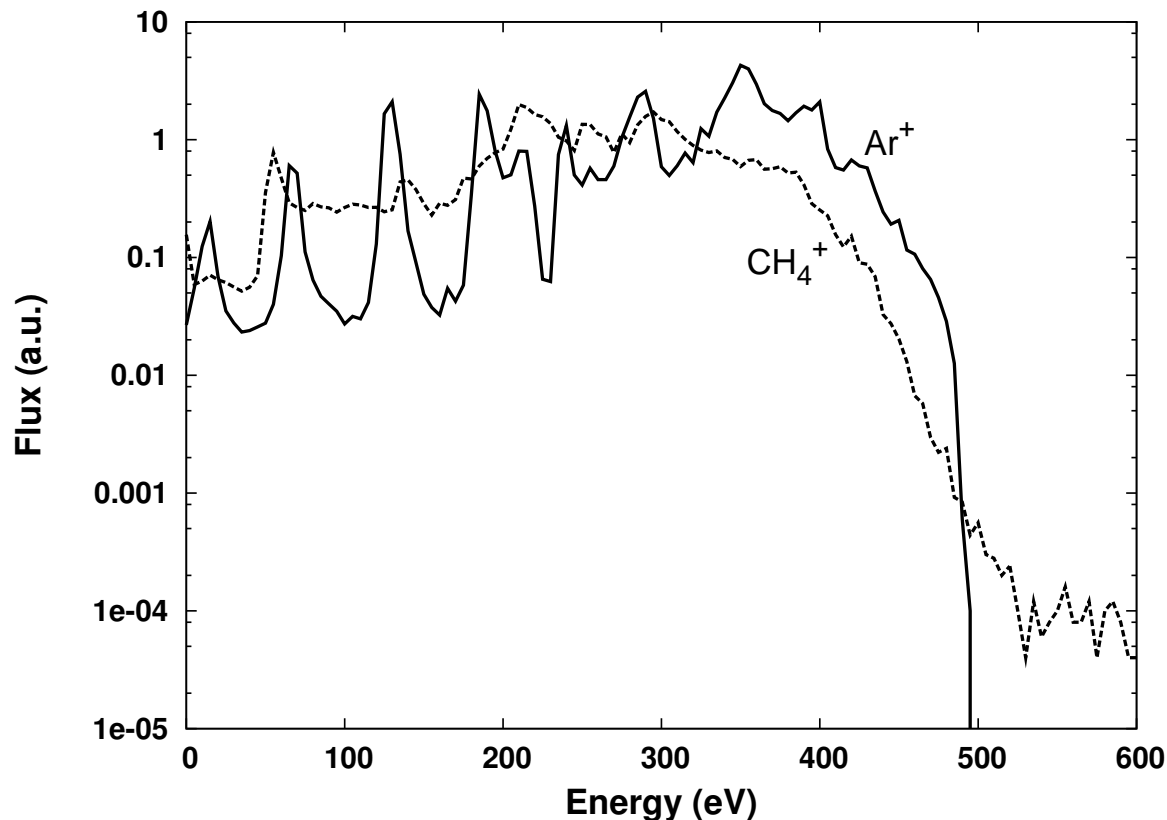
Figure A.9: Experimental IED profiles for Ar$^+$ and CH$_4^+$ Ions. Hydrocarbons do not show energy cut-off.

(PIC) code has been used to give better insight into the principle of operation of an ion extractor unit to measure IEDs at the powered electrode. The effects of the ion transfer optics and the modulation effects of the potential within the ion extractor has been studied. A better match between simulation and experiment is achieved by introducing an effective drift length for the ion optics. However, problems remain for reactive species like hydrocarbons indicating more complex plasma reactions within the device. Interpretation of IEDs measured with such an ion optics system is never a direct measurement of the IED at the electrode surface, but needs interpretation and back-mapping procedures for such purpose.

Bibliography

[1] J. E. Allen, R. L. F. Boyd, and P. Reynolds. The collection of positive ions by a probe immersed in a plasma. *Proc. Phys. Soc. B.*, 70:297–304, 1957.

[2] S. A. Khrapak, S. V. Ratynskaia, A. V. Zobnin, A. D. Usachev, V. V. Yaroshenko, M. H. Thoma, M. Kretschmer, H. Höfner, G. E. Morfill, O. F. Petrov, and V. E. Fortov. Particle charge in the bulk of gas discharges. *Phys. Rev. E*, 72:016406, 2005.

[3] J. E. Allen. Probe theory: The orbital motion approach. *Physica Scripta*, 45:497–503, 1992.

[4] A. V. Zobnin, A. D. Usachev, O. F. Petrov, and V. E. Fortov. Ion current on a small spherical attractive probe in a weakly ionized plasma with ion-neutral collisions (kinetic approach). *Phys. Plasmas*, 15:043705, 2008.

[5] A. Garscadden. Particles in plasmas. *Proceedings of the $20^t h$ International Conference on Phenomena in Ionized Gases, Pisa, Italy*, pages 147–154, 2005.

[6] P. K. Shukla and A. A. Mamun. Introduction to dusty plasma physics. *Institute of Physics, Bristol, UK, ISBN 075030653X*, 2002.

[7] A. Piel and A. Melzer. Dynamical processes in complex plasmas (review article). *Plasma Phys. Control. Fusion*, 44:R1–R26, 2002.

[8] J. A. M. McDonnel ed. Cosmic dust. *Wiley Interscience, New York*, 1978.

[9] U. deAngelis. The physics of dusty plasmas. *Physica Scripta*, 45:465–474, 1992.

[10] C. K. Goertz. Dusty plasmas in the solar system. *Reviews of Geophysics*, 27:271–292, 1989.

[11] G. E. Morfill, E. Grün, and T. B. Johnson. Dust in jupiter's magnetosphere: Physical processes. *Planetary and Space Science*, 28:1087–1100, 1980.

[12] S. J. Piet, A. Costley, G. Federici, F. Heckendorn, and R. Little. Iter tokamak dust - limits, production, removal, surveying. *27th IEEE/NPSS Symposium on Fusion Engineering*, 1997.

[13] F. Y. Huang, H. H. Hwang, and M. J. Kuschner. A model for transport and agglomeration of particles in reactive ion etching plasma reactors. *Journal of Vacuum Science and Technology A: Vacuum, Surfaces, and Films*, 14:562–566, 1996.

[14] G. S. Selwyn. Particulate contamination control in plasma processing: Building-in reliability for semiconductor fabrication. *International Integrated Reliability Workshop Final Report, Lake Tahoe, California, USA*, pages 122–129, 1996.

[15] E. Bertran, S. N. Sharma, G. Viera, J. Costa, P. St'ahel, and P. Roca i Cabarrocas. Effect of the nanoparticles on the structure and crystallization of amorphous silicon thin films produced by rf glow discharge. *Journal of Materials Research*, 13(9):2476–2479, 1998.

[16] E. Stoffels, W. W. Stoffels, G. M. W. Kroesen, and F. J. de Hoog. Dust in plasmas - fiend or friend. *Electron Technology*, 31(2):255–274, 1998.

[17] G. W. Kroesen. Synthesis report: Micropowder processing using low-pressure plasma technology. *Eindhoven (Netherlands) Technical University Report No. BE7328*, 1998.

[18] H. Kersten, G. M. W. Kroesen, and R. Hippler. On the energy influx to the substrate during sputter deposition of thin aluminium films. *Thin Solid Films*, 332(1-2):282–289, 1998.

[19] H. Kersten, P. Schmetz, and G. M. W. Kroesen. Surface modification of powder particles by plasma deposition of thin metallic films. *Surface and Coatings Technology*, 109(1-3):507–512, 1998.

[20] G. H. P. M. Swinkels, E. Stoffels, W. W. Stoffels, N. Simons, G. M. W. Kroesen, and F. J. de Hoog. Treatment of dust particles in an rf plasma monitored by

mie scattering rotating compensator ellipsometry. *Pure and Applied Chemistry*, 70(6):1151–1156, 1998.

[21] W. W. Stoffels, E. Stoffels, G. H. P. M. Swinkels, M. Boufnichel, and G. M. W. Kroesen. Etching a single micrometer-size particle in a plasma. *Phys. Rev. E*, 59(2B):2302–2304, 1999.

[22] V. E. Fortov, A. V. Ivlev, S. A. Khrapak, A. G. Khrapak, and G. E. Morfill. Complex *dusty* plasmas: Current status, open issues, perspectives. *Physics Reports*, 421:1–103, 2005.

[23] J. H. Chu and L. I. Direct observation of coulomb crystals and liquids in strongly coupled r.f. dusty plasmas. *Phys. Rev. Lett.*, 72:4009–4012, 1994.

[24] H. Thomas, G. E. Morfill, V. Demmel, J. Goree, B. Feuerbacher, and D. Mohlmann. Plasma crystal: Coulomb crystallization in a dusty plasma. *Phys. Rev. Lett.*, 73:652–655, 1994.

[25] Y. Hayashi and S. Tachibana. Observation of coulombâĂŞcrystal formation from carbon particles grown in a methane plasma. *Jpn. J. Appl. Phys.*, 33:L804–L806, 1994.

[26] A. Melzer, T. Trottenberg, and A. Piel. Experimental determination of the charge on dust particles forming coulomb lattices. *Phys. Lett. A*, 191:301–308, 1994.

[27] A. Melzer, V. A. Schweigert, and A. Piel. Transition from attractive to repulsive forces between dust molecules in a plasma sheath. *Phys. Rev. Lett.*, 83:3194–3197, 1999.

[28] A. Melzer, V. A. Schweigert, and A. Piel. Measurement of the wakefield attraction for 'dust plasma molecules'. *Physica Scripta*, 61:494–501, 2000.

[29] G. E. Morfill, H. M. Thomas, U. Konopka, and M. Zuzic. The plasma condensation: Liquid and crystalline plasmas. *Physics of Plasmas*, 6(5):1769–1780, 1999.

[30] J. Goree, G. E. Morfill, V. N. Tsytovich, and S. V. Vladimirov. Theory of dust voids in plasmas. *Phys. Rev. E*, 59:7055–7067, 1999.

[31] M. Wolter, A. Melzer, O. Arp, M. Klindworth, M. Kroll, and A. Piel. Laser manipulation of the void edge in dusty plasmas under microgravity. *IEEE Trans. on Plasma Science*, 35(2):266–270, 2007.

[32] M.A. Lieberman and A.J. Lichtenberg. Principles of plasma discharges and materials processing. *New York: Wiley*, 1994.

[33] H. Mott-Smith and I. Langmuir. The theory of collectors in gaseous discharges. *Phys. Rev.*, 28:727–763, 1926.

[34] I. B. Bernstein and I. Rabinowitz. Theory of electrostatic probes in a low-density plasma. *Phys. Fluids*, 2:112–121, 1959.

[35] J. G. Laframboise. Theory of spherical and cylindrical langmuir probes in a collisionless maxwellian plasma at rest. *U.T.I.A.S. Report No. 100*, 1996.

[36] R. V. Kennedy and J. E. Allen. The floating potential of spherical probes and dust grains. part i. radial motion theory. *J. Plasma Physics*, 67:243–250, 2002.

[37] M. Lampe, V. Gavrishchaka, G. Ganguli, and G. Joyce. Effect of trapped ions on shielding of a charged spherical object in a plasma. *Phys. Rev. Lett.*, 86(23):5278–5281, 2001.

[38] M. Lampe, R. Goswami, Z. Sternovsky, S. Robertson, V. Gavrishchaka, G. Ganguli, and G. Joyce. Trapped ion effect on shielding, current flow, and charging of a small object in a plasma. *Physics of Plasmas*, 10(5):1500–1513, 2003.

[39] A. V. Zobnin, A. P. Nefedov, V. A. Sinel'shchikov, and V. E. Fortov. On the charge of dust particles in a low-pressure gas discharge plasma. *JETP*, 91 (3):483–487, 2000.

[40] I.H.Hutchinson. Ion collection by a sphere in a flowing plasma: 1. quasineutral. *Plasma Phys. Control. Fusion*, 44:1953–1977, 2002.

[41] I.H.Hutchinson. Ion collection by a sphere in a flowing plasma: 2. non-zero debye length. *Plasma Phys. Control. Fusion*, 45:1477–1500, 2003.

[42] I.H.Hutchinson. Ion collection by a sphere in a flowing plasma: 3. floating potential and drag force. *Plasma Phys. Control. Fusion*, 47:71–87, 2005.

[43] I.H.Hutchinson. Collisionless ion drag force on a spherical grain. *Plasma Phys. Control. Fusion*, 48:185–202, 2006.

[44] I.H.Hutchinson and L.Patacchini. Computation of the effect of neutral collisions on ion current to a floating sphere in a stationary plasma. *Phys. of Plasmas*, 14:013505, 2007.

[45] V.A. Godyak and R.B.Piejak. Abnormally low electron energy and heating-mode transition in a low-pressure argon rf discharge at 13.56 mhz. *Phys. Rev. Lett.*, 65:996–999, 1990.

[46] K. Matyash and R. Schneider. Pic-mcc modeling of a capacitive rf discharge. *Contributions to Plasma Physics*, 44(7-8):589–593, 2004.

[47] M.S. Barnes, J. H. Keller, J. C. Forster, J. A. O'Neill, and D. K. Coultas. Transport of dust particles in glow-discharge plasmas. *Phys. Rev. Lett.*, 68(3):313–316, 1992.

[48] S.A. Khrapak, A. V. Ivlev, G. E. Morfill, and H. M. Thomas. Ion drag force in complex plasmas. *Phys. Rev. E*, 66:046414, 2002.

[49] S.A. Khrapak, A. V. Ivlev, G. E. Morfill, and S. K. Zhdanov. Scattering in the attractive yukawa potential in the limit of strong interaction. *Phys. Rev. Lett.*, 90:225002, 2003.

[50] S.A. Khrapak, B. A. Klumov, and G. E. Morfill. Electric potential around an absorbing body in plasmas: Effect of ion-neutral collisions. *Phys. Rev. Lett.*, 100:225003, 2008.

[51] F. F. Chen. Introduction to plasma physics and controlled fusion, volume 1: Plasma physics. *Plenum Press, New York*, 1984.

[52] W. Schottky. Diffusionstheorie der positiven säule. *Physikalische Zeitschrift*, 25:635–640, 1924.

[53] C. D. Child. Discharges from hot cao. *Phys. Rev.*, 32:492–511, 1911.

[54] I. Langmuir. The effect of space charge and residual gases on thermionic currents in high vacuum. *Phys. Rev.*, 2(6):450–486, 1913.

[55] I. Langmuir. The effect of space charge and initial velocities on the potential distribution and thermionic current between parallel plane electrodes. *Phys. Rev.*, 21:419–435, 1923.

[56] I. Langmuir and H. Mott-Smith. Studies of electrical discharges in gases at low pressures. *General Electrical Review*, 27(12):810–820, 1924.

[57] I. Langmuir. The interaction of electron and positive ion space charges in cathode sheaths. *Phys. Rev.*, 33:954–989, 1929.

[58] D. Bohm. The characteristics of electrical discharges in magnetic fields. *ed. A. Guthrie and R.K. Wakerling, New York: McGraw-Hill*, 1949.

[59] R. N. Franklin and J. Snell. The transition from collisionless to collisional active plasma and the relevance of the bohm criterion to sheath formation. *Physics of Plasmas*, 7:3077–3083, 2000.

[60] K.-U. Riemann. The influence of collisions on the plasma sheath transition. *Physics of Plasmas*, 4(11):4158–4166, 1997.

[61] K.-U. Riemann. The bohm criterion and sheath formation. *Journal of Physics D: Applied Physics*, 24:493–518, 1991.

[62] K.-U. Riemann. The validity of bohm's sheath criterion in rf discharges. *Physics of Fluids*, 4(9):2693–2695, 1992.

[63] R. N. Franklin and J. R. Ockendon. Asymptotic matching of plasma and sheath in an active low pressure discharge. *Journal of Plasma Physics*, 4(2):371–385, 1970.

[64] R. N. Franklin and J. Snell. Joining a collisional sheath to an active plasma. *Journal of Physics D: Applied Physics*, 30:L45–L47, 1997.

[65] Y. P. Raizer, M. N. Schneider, and N. A. Yatsenko. Radio frequency capacitive discharges. *CRC Press Inc.*, 1995.

[66] T. G. Northrop. Dusty plasmas. *Physica Scripta*, 45:475–490, 1992.

[67] E. C. Whipple. Potentials of surfaces in space. *Rep. Prog. Phys.*, 44:1197–1250, 1981.

[68] P. A. Robinson and P. Coakley. Spacecraft charging-progress in the study of dielectrics and plasmas. *IEEE Trans. Electr. Insul.*, 27:944–960, 1992.

[69] J. Winter and G. Gebauer. Dust in magnetic confinement fusion devices and its impact on plasma operation. *J. Nucl. Mater.*, 266:228–233, 1999.

[70] J. Winter. Dust: A new challenge in nuclear fusion research? *Physics of Plasmas*, 7:3862–3866, 2000.

[71] A. Bouchoule. Dusty plasmas. *John Wiley & Sons, Chichester*, 1999.

[72] H. Kersten, R. Wiese, G. Thieme, M. Fröhlich, A. Kopitov, D. Bojic, F. Scholze, H. Neumann, M. Quaas, H. Wulff, and R. Hippler. Examples for application and diagnostics in plasma-powder interaction. *New J. Phys.*, 5:93.1–93.15, 2003.

[73] P. Roca i Cabarrocas and S. Hamma. Microcrystalline silicon growth on a- si:h : effects of hydrogen. *Thin Solid Films*, 337:23–26, 1999.

[74] J. Goree. Charging of particles in a plasma. *Plasma Sources Science and Technology*, 3:400–406, 1994.

[75] T. Trottenberg, A. Melzer, and A. Piel. Measurement of the electric charge on particulates forming coulomb crystals in the sheath of a radiofrequency plasma. *Plasma Sources Sciences and Technology*, 4:450–458, 1995.

[76] J. E. Allen, B. M. Annaratone, and U. de Angelis. On the orbital motion limited theory for a small body at floating potential in maxwellian plasmas. *J. Plasma Phys.*, 63:299–310, 2000.

[77] B. M. Annaratone, M. W. Allen, and J. E. Allen. Ion currents to cylindrical langmuir probes in rf plasmas. *J. Physics D: Applied Phys.*, 25:417–424, 1992.

[78] R. V. Kennedy and J. E. Allen. The floating potential of spherical probes and dust grains. part ii. orbital motion theory. *J. Plasma Physics*, 69:485–506, 2003.

[79] J. D. Swift and M. J. R. Schwar. Electrical probes for plasma diagnostics. *London: Iliffe Books*, 1970.

[80] S. V. Ratynskaia, S. A. Khrapak, A. V. Zobnin, M. H. Thoma, M. Kretschmer, A. D. Usachev, V. V. Yaroshenko, R. A. Quinn, G. E. Morfill, O. F. Petrov, and

V. E. Fortov. Experimental determination of dust-particle charge in a discharge plasma at elevated pressures. *Phys. Rev. Lett.*, 93(8):085001, 2004.

[81] Y. L. Alpert, A. V. Gurevich, and L. P. Pitaevskii. Space physics with artificial satellites. *New York: Plenum Press*, 1965.

[82] F.F. Chen. Numerical computations for ion probe characteristics in a collisionless plasma. *J. Nucl. Energy C: Plasma Phys.*, 7:47–67, 1965.

[83] R. N. Nowlin and R.N. Carlile. The electrostatic nature of contaminative particles in a semiconductor processing plasma. *J. Vacuum Sci. Technol. A*, 9(5):2825–2833, 1991.

[84] J. E. Daugherty, R. K. Porteous, M. D. Kilgore, and D. B. Graves. Sheath structure around particles in low-pressure discharges. *J. Appl. Phys.*, 72(9):3934–3942, 1992.

[85] U. Kortshagen and G. Mümken. The electrical charging of micron-sized dust particles in a capacitively coupled rf plasma. *Physics Letters, A*, 217:126–132, 1996.

[86] A. Homann, A. Melzer, and A. Piel. Measuring the charge on single particles by laser-excited resonances in plasma crystals. *Phys. Rev. E*, 59(4):R3835–R3838, 1999.

[87] E. B. Tomme, B. M. Annaratone, and J E Allen. Damped dust oscillations as a plasma sheath diagnostic. *Plasma Sources Sci. Technol.*, 9:87–96, 2000.

[88] E. B. Tomme, D. A. Law, B. M. Annaratone, and J E Allen. Parabolic plasma sheath potentials and their implications for the charge on levitated dust particles. *Phys. Rev. Lett.*, 85(12):2518–2521, 2000.

[89] U. Konopka, L. Ratke, and H. M. Thomas. Central collisions of charged dust particles in a plasma. *Phys. Rev. Lett.*, 79(7):1269–1272, 1997.

[90] U. Konopka, G. E. Morfill, and L. Ratke. Measurement of the interaction potential of microspheres in the sheath of a rf discharge. *Phys. Rev. Lett.*, 84(5):891–894, 2000.

[91] S. Nunomura, T. Misawa, N. Ohno, and S. Takamura. Instability of dust particles in a coulomb crystal due to delayed charging. *Phys. Rev. Lett.*, 83(10):1970–1973, 1999.

[92] B. Liu, K. Avinash, and J. Goree. Characterization of interparticle potential from lattice structure. *Phys. Rev. E*, 69:036410, 2004.

[93] A. Homann, A. Melzer, S. Peters, and A. Piel. Determination of the dust screening length by laser-excited lattice waves. *Phys. Rev. E*, 56:7138–7141, 1997.

[94] B. Walch, M. Horanyi, and S. Robertson. Measurement of the charge on individual dust grains in a plasma. *IEEE Trans. Plasma Sci.*, 22(2):97–102, 1994.

[95] Z. Sternovsky, M. Horanyi, and S. Robertson. Charging of dust particles on surfaces. *J. Vacuum Sci. Technol. A*, 19:2533–2541, 2001.

[96] C. Cui and J. Goree. Fluctuations of the charge on a dust grain in a plasma. *IEEE Trans. on Plasma Science*, 22:151–158, 1994.

[97] F. Verheest. Waves in dusty space plasmas. *Kluver Academic Publishers, Dordrecht*, 2000.

[98] O. Havnes, C. K. Goertz, G. E. Morfill, E. Grün, and W. Ip. Dust charges, cloud potential, and instabilities in a dust cloud embedded in a plasms. *J. Geophys. Res.*, 92(A3):2281–2293, 1987.

[99] M.D. Kilgore, J. E. Daugherty, R. K. Porteous, and D. B. Graves. Ion drag on an isolated particulate in a low pressure discharge. *J. Appl. Phys.*, 73:7195–7202, 1993.

[100] J. Perrin, P. Molinas-Mata, and P. Belenguer. Ion drag and plasma-induced thermophoresis on particles in radiofrequency glow discharges. *J. Phys. D: Appl. Phys.*, 27:2499–2507, 1994.

[101] G. M. Jellum, J. E. Daugherty, and D. B. Graves. Particle thermophoresis in low pressure glow discharges. *J. Appl. Phys.*, 69:6923–6934, 1991.

[102] J. E. Daugherty and D. B. Graves. Sheath structure around particles in low-pressure discharges. *J. Appl. Phys.*, 78:2279–2287, 1995.

[103] H. Vestner and J. Halbritter. Torque on a small particle in a nonhomogeneous monatomic gas. *Z. Naturforsch.*, 36a (6):559–567, 1981.

[104] J. E. Daugherty, R. K. Porteous, and D. B. Graves. Sheath structure around particles in low-pressure discharges. *J. Appl. Phys.*, 73:1617–1620, 1993.

[105] S. Hamaguchi and R. T. Farouki. Polarization force on a charged particulate in a nonuniform plasma. *Phys. Rev. E*, 49:4430–4441, 1994.

[106] S. Hamaguchi and R. T. Farouki. Plasma-particulate interaction in nonuniform plasmas with finite flows. *Phys. Plasmas*, 1:2110–2118, 1994.

[107] P. Epstein. On the resistance experienced by spheres in their motion through gases. *Phys. Rev.*, 23:710–733, 1924.

[108] O. Arp, D. Block, A. Piel, and A. Melzer. Dust coulomb balls: three-dimensional plasma crystals. *Phys. Rev. Lett.*, 93:165004, 2004.

[109] O. Arp, D. Block, M. Klindworth, and A. Piel. Confinement of coulomb balls. *Phys. Plasmas*, 12:122102, 2005.

[110] A. Melzer, S. Nunomura, D. Samsonov, and J. Goree. Laser-excited mach cones in a dusty plasma crystal. *Phys. Rev. E*, 62:4162–4176, 2000.

[111] V. Nosenko, J. Goree, Z. W. Ma, and A. Piel. Observation of shear-wave mach cones in a 2d dusty-plasma crystal. *Phys. Rev. Lett.*, 88:135001, 2002.

[112] V. Nosenko, J. Goree, Z. W. Ma, D. H. E. Dubin, and A. Piel. Compressional and shear wakes in a two-dimensional dusty plasma crystal. *Phys. Rev. E*, 68:056409, 2003.

[113] W.-T. Juan, Z.-H. Huang, J.-W. Hsu, Y.-J. Lai, and L. I. Observation of dust coulomb clusters in a plasma trap. *Phys. Rev. E*, 58:R6947–R6950, 1998.

[114] R. A. Quinn, C. Cui, J. Goree, J. B. Pieper, H. Thomas, and G. E. Morfill. Structural analysis of a coulomb lattice in a dusty plasma. *Phys. Rev. E*, 53:2049–2052, 1996.

[115] D. Samsonov, J. Goree, H. M. Thomas, and G. E. Morfill. Mach cone shocks in a twoâĂŞdimensional yukawa solid using a complex plasma. *Phys. Rev. E*, 61:5557–5572, 2000.

[116] M. Klindworth, A. Melzer, A. Piel, and V. A. Schweigert. Laser-excited intershell rotation of finite coulomb clusters in a dusty plasma. *Phys. Rev. B*, 61:8404–8410, 2000.

[117] B. Liu, J. Goree, V. Nosenko, and L. Boufendi. Radiation pressure and gas drag forces on a melamine-formaldehyde microsphere in a dusty plasma. *Phys. Plasmas*, 10:9–20, 2003.

[118] J. R. Burke and D. J. Hollenbach. The gas-grain interaction in the interstellar medium: Thermal accommodation and trapping. *The Astrophysical Journal*, 265:223–234, 1983.

[119] T. Nitter. Levitation of dust in rf and dc glow discharges. *Plasma Sources Sciences and Technology*, 5:93–111, 1996.

[120] T. E. Sheridan. Center-of-mass and breathing oscillations in small complex plasma disks. *Phys. Rev. E*, 72:026405, 2005.

[121] L. Talbot, R. K. Cheng, R. W. Schefer, and D. R. Willis. Thermophoresis of particles in a heated boundary layer. *J. Fluid Mech.*, 101:737–758, 1980.

[122] C. Zafiu, A. Melzer, and A. Piel. Ion drag and thermophoretic forces acting on free falling charged particles in an rf-driven complex plasma. *Phys. Plasmas*, 9:4794–4803, 2002.

[123] C. Zafiu, A. Melzer, and A. Piel. Measurement of the ion drag force on falling dust particles and its relation to the void formation in complex (dusty) plasmas. *Phys. Plasmas*, 10(5):1278–1282, 2003.

[124] V. V. Yaroshenko, S. Ratynskaia, S. A. Khrapak, M. H. Thoma, M. Kretschmer, and G. E. Morfill. Measurements of the dust-ion momentum transfer frequency and ion drag force in complex plasmas. *Contrib. Plasma Phys.*, 45(3-4):223–228, 2007.

[125] V. V. Yaroshenko, S. Ratynskaia, S. A. Khrapak, M. H. Thoma, M. Kretschmer, H. Hofner, G. E. Morfill, A. Zobnin, A. Usachev, O. Petrov, and V. Fortov. Determination of the ion-drag force in a complex plasma. *Phys. Plasmas*, 12:093503, 2005.

[126] S.A. Khrapak, S. K. Zhdanov, A. V. Ivlev, and G. E. Morfill. Drag force on an absorbing body in highly collisional plasmas. *J. Appl. Phys.*, 101:033307, 2007.

[127] L. Patacchini and I. H. Hutchinson. Fully self-consistent ion-drag-force calculations for dust in collisional plasmas with an external electric field. *Phys. Rev. Lett.*, 101:025001, 2008.

[128] S. Chandrasekhar. Dynamical friction, i. general considerations: the coefficient of dynamical friction. *Astrophys. Journal*, 97:255–262, 1943.

[129] M. Hirt, D. Block, and A. Piel. Measurements of the ion drag force on micrometer sized particles in the double plasma device dodo. *IEEE Trans. on Plasma Science*, 32 (2):582 – 585, 2004.

[130] H. Rothermel, T. Hagl, G. E. Morfill, M. H. Thoma, and H.M. Thomas. Gravity compensation in complex plasmas by application of a temperature gradient. *Phys. Rev. Lett.*, 89(17):175001, 2002.

[131] V. Nosenko, R. Fisher, R. Merlino, S. Khrapak, G. E. Morfill, and K. Avinash. Measurement of the ion drag force in a collisionless plasma with strong ion-grain coupling. *Phys. Plasmas*, 14:103702, 2007.

[132] M. Kretschmer, S. A. Khrapak, S. K. Zhdanov, H. M. Thomas, , G. E. Morfill, V. E. Fortov, A. M. Lipaev, V. I. Molotkov, A. I. Ivanov, and M. V. Turin. Force field inside the void in complex plasmas under microgravity conditions. *Phys. Rev. E*, 71:056401, 2005.

[133] A. V. Ivlev, S.A. Khrapak, S. K. Zhdanov, G. E. Morfill, and G. Joyce. Force on a charged test particle in a collisional flowing plasma. *Phys. Rev. Let.*, 92:205007, 2004.

[134] A. V. Ivlev, S. K. Zhdanov, S.A. Khrapak, and G. E. Morfill. Kinetic approach for the ion drag force in a collisional plasma. *Phys. Rev. E*, 71:016405, 2005.

[135] S.A. Khrapak, B. A. Klumov, and G. E. Morfill. Ion collection by a sphere in a flowing highly collisional plasma. *Phys. of Plasmas*, 14:034502, 2007.

[136] S.A. Khrapak, G. E. Morfill, V. E. Fortov, L. G. D'yachkov, A. G. Khrapak, and O. F. Petrov. Attraction of positively charged particles in highly collisional plasmas. *Phys. Rev. Lett.*, 99:055003, 2007.

[137] M. Chaudhuri, S. A. Khrapak, and G. E. Morfill. Ion drag force on a small grain in highly collisional weakly anisotropic plasma: Effect of plasma production and loss mechanisms. *Phys. of Plasmas*, 15:053703, 2005.

[138] V. E. Fortov, A. P. Nefedov, V. M. Torchinskii, V. I. Molotkov, A. G. Khrapak, O. F. Petrov, and K. F. Volykhin. Crystallization of a dusty plasma in the positive column of a glow discharge. *JETP Lett.*, 64:92–98, 1996.

[139] V. E. Fortov, A. P. Nefedov, V. I. Vladimirov, L. V. Deputatova, V. I. Molotkov, V. A. Rykov, and A. V. Khudyakov. Dust particles in a nuclear-induced plasma. *Phys. Lett. A*, 258:305–311, 1999.

[140] A. P. Nefedov, G. E. Morfill, V. E. Fortov, H. M. Thomas, H. Rotherme, T. Hag, A. V. Ivlev, M. Zuzic, B. A. Klumov, A. M. Lipaev, V. I. Molotkov, O. F. Petrov, Y. P. Gidzenko, S. K. Krikalev, W. Shepherd, A. I. Ivanov, M. Roth, H. Binnenbruck, J. A. Goree, and Y. P. Semenov. Pke-nefedov: Plasma crystal experiments on the international space station. *New J. Phys.*, 5:33.1–33.10, 2003.

[141] M. Wolter, A. Melzer, O. Arp, M. Klindworth, and A. Piel. Force measurements in dusty plasmas under microgravity by means of laser manipulation. *Phys. Plasmas*, 14:123707, 2007.

[142] S. I. Braginskii. Transport processes in a plasma. in reviews of plasma physics, volume 1, m. a. leontovich, editor. *Consultants Bureau, New York*, 1965.

[143] R. Chodura. Particle simulation of the plasma-wall transition. *Proceedings of the $8^t h$ Europhysics Conference on Computational Physics, Computing in Plasma Physics, Garmisch*, 1986.

[144] C. K. Birdsall and A. B. Langdon. Plasma physics via computer simulation. *McGraw-Hill, New York*, 1985.

[145] R. Hockney and J. Eastwood. Computer simulation using particles. *McGraw-Hill, New York*, 1981.

[146] K. Matyash, R. Schneider, F. Taccogna, A. Hatayama, S. Longo, M. Capitelli, D. Tskhakaya, and F. X. Bronold. Particle in cell simulation of low temperature laboratory plasmas. *Contrib. Plasma Phys.*, 47(8-9):595–634, 2007.

[147] D. Tskhakaya, K. Matyash, R. Schneider, and F. Taccogna. The particle in cell method. *Contrib. Plasma Phys.*, 47(8-9):563–594, 2007.

[148] K. Matyash. Kinetic modeling of multi-component edge plasmas. *Ph.D. submitted to Ernst-Moritz-Arndt-Universität Greifswald. Available at: http://www.ipp.mpg.de/k̃nm/*, 2003.

[149] W.H. Press, B. P. Flannery, S. A. Teukolsky, and W. T. Vetterling. Numerical recipes in c: The art of scientific computing. *Cambridge University Press*, 2002.

[150] J.W. Demmel, J. R. Gilbert, and X. S. Li. Superlu usersâĂŹ guide, technical report lbnl-44289. *Lawrence Berkley National Laboratory, September 1999. Software is available at: http://www.nersc.gov/x̃iaoye/SuperLU*, 1999.

[151] V. Vahedi and M. Surendra. A monte carlo collision model for the particle-in-cell method: applications to argon and oxygen discharges. *Computer Physics Communications*, 87(1-2):179–198, 1995.

[152] K. Matyash and R. Schneider. Finite size effects on charging in dusty plasmas. *J. Plasma Phys.*, 72(6):809–812, 2006.

[153] R. Smirnov, Y. Tomita, T. Takizuka, A. Takayama, and Yu. Chutov. Particle simulation study of dust particle dynamics in sheaths. *Contrib. Plasma Phys.*, 44(1-3):150–156, 2004.

[154] R. Smirnov, Y. Tomita, D. Tskhakaya, and T. Takizuka. Two-dimensional simulation study on charging of dust particle on plasma-facing wall. *Contrib. Plasma Phys.*, 46(7-9):623–627, 2006.

[155] E. Kawamura, V. Vahedi, M. A. Lieberman, and C. K. Birdsall. Ion energy distributions in rf sheaths: review, analysis and simulation. *Plasma Sources Sci. Technol.*, 8:R45–R64, 1999.

[156] T. Takizuka and H. Abe. A binary collision model for plasma simulation with a particle code. *J. Comp. Phys.*, 25:205–219, 1977.

[157] A. V. Phelps. Jila data base. *(unpublished), Available at: ftp://jila.colorado.edu/collision_ data/*, 2008.

[158] M. M. Turner, R. A. Doyle, and M. B. Hopkins. Measured and simulated electron energy distribution functions in a low-pressure radio frequency discharge in argon. *Appl. Phys. Lett.*, 62:3247–3249, 1993.

[159] C. M. O. Mahony, J. McFarland, P. G. Steen, and W. G. Graham. Structure observed in measured electron energy distribution functions in capacitively coupled radio frequency hydrogen plasmas. *Appl. Phys. Lett.*, 75(3):331–333, 1999.

[160] K. Matyash, R. Schneider, F. Taccogna, and D. Tskhakaya. Finite size effect of dust charging in the magnetized edge plasma. *J. Nuclear Materials*, 363-365:458–461, 2007.

[161] M. Lampe, G. Joyce, and G. Ganguli. Interactions between dust grains in a dusty plasma. *Phys. Plasmas*, 7(10):3851–3861, 2000.

[162] A. Melzer, A. Homann, and A. Piel. Experimental investigation of the melting transition of the plasma crystal. *Phys. Rev. E*, 53:2757–2766, 1996.

[163] V. R. Ikkurthi, K. Matyash, A. Melzer, and R. Schneider. Computation fo dust charge and potential on a static spherical dust grain immersed in rf discharges. *Phys. of Plasmas*, 15:123704, 2008.

[164] W. J. Goedheer. Lecture notes on radio-frequency discharges, dc potentials, ion and electron energy distributions. *Plasma Sources Sci. Tech.*, 9:507–516, 2000.

[165] J. Zhou, I. T. Martin, R. Ayers, E. Adams, D. Liu, and E. R. Fisher. Investigation of inductively coupled ar and ch_4/ar plasmas and the effect of ion energy on dlc film properties. *Plasma Sources Sci. Tech.*, 15:714–726, 2006.

[166] C. Wild, J. Wagner, and P. Koidl. Process monitoring of a-c:h plasma deposition. *J. Vac. Sci. Technol. A*, 5:2227–2230, 1987.

[167] C. W. Jurgensen. Sheath collision processes controlling the energy and directionality of surface bombardment in o2 reactive ion etching. *J. Appl. Phys.*, 64:590–597, 1988.

[168] C. W. Jurgensen and A. Rammelsberg. Oxygen reactive ion etching mechanisms of organic and organosilicon polymers. *J. Vac. Sci. Technol. A*, 7(6):3317–3324, 1989.

[169] A. D. Kuypers and H. J. Hopman. Measurement of ion energy distributions at the powered rf electrode in a variable magnetic field. *J. Appl. Phys.*, 67:1229–1240, 1990.

[170] M. Zeuner, J. Meichsner, and J. A. Rees. High energy negative ions in a radio-frequency discharge. *J. Appl. Phys.*, 79:9379–9381, 1996.

[171] M. Zeuner, J. Meichsner, H. Neumann, F. Scholze, and F. Bigl. Design of ion energy distributions by a broad beam ion source. *J. Appl. Phys.*, 80:611–622, 1996.

[172] Sz. Katai, Z. Tass Gy. Hars, and P. Deak. Measurement of ion energy distributions in the bias enhanced nucleation of chemical vapor deposited diamond. *J. Appl. Phys.*, 86(10):5549–5555, 1999.

[173] J. R. Woodworth, I. C. Abraham, M. E. Riley, P. A. Miller, T. W. Hamilton, B. P. Aragon, R. J. Shul, and C. G. Willison. Ion energy distributions at rf-biased wafer surfaces. *J. Vac. Sci. Technol. A*, 20:873–886, 2002.

[174] J. Bohlmark, M. Lattemanna, J.T. Gudmundsson, A.P. Ehiasarian, Y. Aranda Gonzalvo, N. Brenning, and U. Helmersson. The ion energy distributions and ion flux composition from a high power impulse magnetron sputtering discharge. *Thin Solid Films*, 515(4):1522–1526, 2006.

[175] S. G. Walton, R. F. Fernsler, and D. Leonhardt. Measurement of ion energy distributions using a combined energy and mass analyzer. *Rev. Sci. Instrum.*, 78(8):083503, 2007.

[176] J. Meichsner, M. Polak, and O. Gabriel. Schichtbildung und ionenanalyse einer kapazitiv gekoppelten rf-entladung in einem methan-argon-gemisch. *(unpublished)*, 2005.

[177] M. Zeuner, H. Neumann, and J. Meichsner. Ion energy distributions in a dc biased rf discharge. *J. Appl. Phys.*, 81:2985–2994, 1997.

[178] C. Wild and P. Koidl. Ion and electron dynamics in the sheath of radio-frequency glow discharges. *J. Appl. Phys.*, 69(5):2909–2922, 1991.

[179] A. B. Ehrhardt and W. D. Langer. Collisional processes of hydrocarbons in hydrogen plasmas. *Report PPL-2477, Plasma Physics Laboratory, Princeton University, USA*, 1988.

[180] R. K. Janev, W. D. Langer, D. E. Post, and K. Evans. Elementary processes in hydrogen-helium plasmas: : Cross sections and reaction rate coefficients. *Springer-Verlag, New York*, 1987.

[181] T. Tabata and T. Shirai. Analytic cross sections for collisions of h^+, h_2+, h_3+, h, h_2 and h^- with hydrogen molecules. *Atomic Data and Nuclear Data Tables*, 76:1–25, 2000.

[182] K. M. Ervin and P. B. Armentrout. Translational energy dependence of ar^+ + xy $\rightarrow$ arx^+ + y (xy=h_2, d_2, hd) from thermal to 30 ev c.m. *J. Chem. Phys.*, 83(1):166–189, 1985.

[183] F. X. Bronold, K. Matyash, D. Tskhakaya, R. Schneider, and H. Fehske. Radio-frequency discharges in oxygen: I. particle-based modelling. *J. Phys. D: Appl. Phys.*, 40:6583–6592, 2007.

Acknowledgments

In addition to my own efforts, encouragement and help of many other people lead to successful completion of this thesis. I would like to thank them.

First and foremost I offer my sincerest gratitude to my supervisors, Prof. André Melzer and Dr. Ralf Schneider, who have invited me to Greifswald and given the golden chance of working with them. They have supported me throughout my thesis with their knowledge whilst allowing me to work in my own way. One simply could not wish for a better or friendlier supervisors. I convey special gratitude to Dr. Konstantin Matyash for providing the computational tool and helping in many ways during my thesis work. Especially, his comments/suggestions/reviews for my work are invaluable. I attribute the level of my Doctoral degree to these three peoples' encouragement.

The thesis work has been financially supported by SFB-TR24 under Project-A4 and COMAS. I gratefully acknowledge these funding bodies.

I am indebted to many people at my parent working institute: Institute for Plasmas Research, Gandhinagar, India. Many special thanks to our group leader Dr. Shashank Chaturvedi for encouraging and supporting me to apply abroad for Ph.d. I am also thankful to academic committee chairman Dr. Vasu and our director Prof. P.K. Kaw for granting study leave for three years. My special gratitude to Dr. Manoj Warrior for recommending me to thesis supervisors. I am very much indebted to Aaditya for being a good friend all the time and any words are not sufficient to thank for his help in administrative matters all these years. Many thanks to Rambabu and Lakshmikanthrao for providing space for our furniture for such a long time of three years.

During my thesis work, I had opportunity to do collaborative work with other groups and I am very much thankful for the support I received, especially from Prof. J. Meichsner and Prof. R. Hippler. It is a pleasure to collaborate with their groups.

In my daily work I have been blessed with a friendly and cheerful group of fellow students. I thank all previous and present group members of Kollaidale Plasmen group and Computational Material Science group. Special thanks to Yuriy, Sabastian, Birger

and Tobias for help with Deutsch language and subject discussions. Lunchtimes with Abha are memorable. Many thanks to Lars for reading the thesis and providing suggestions. I also thank secretaries for necessary support and understanding my butler Deutsch.

I would also like to thank Henry Leyh and Dr. Matthias Borchardt at IPP for providing support with linux cluster and for their quick responses and solutions.

Many thanks to graduate students in the IMPRS and its organizers for providing such a good atmosphere of learning. Talks, seminars, workshops and feedback from IMPRS are very valuable.

I am thankful to all "Indogreifs" (Indians at Greifswald) for making our stay at Greifswald very pleasant. All the festivals we celebrated, meetings we had, trips to nearby places are unforgettable. Special mention and thanks should go to Sudarshan and Kumar for engaging kids when I am away for conferences. Many special thanks to Amit and Swathi for providing company and showing around when we arrived in Greifswald. I am grateful to Frau.Stolz for making our stay at IBZ very comfortable.

Where would I be without my family? My parents deserve special mention for their inseparable support and prayers. My Father, Veeranjaneyulu, in the first place is the person from whom I learnt to be confident and strong under any circumstances. My Mother, Parvathi, is the one who sincerely raised me with her caring and gentle love. My appreciation to my brother, Venkateswarlu, for taking the responsibility of our parents all these three years. My deepest dedication to my uncle, Chandrasekhar rao, for his encouragement in educational and other matters since my childhood.

Words fail me to express my appreciation to my wife Deepu whose love and confidence in me, has taken the family load off my shoulder. Inspite of pregnancy and health issues, she has been tough and supported me to achieve my goal of completing thesis work. Both Lillu and Chikki are very lovely and adjusting kids, whose cute smiles helped me recharging myself. I would also thank my inlaws for their support and encouragement. Particularly, many special thanks to Suresh for his help and support.

Finally, I would like to thank everybody who was important to the successful realization of the thesis, as well as express my apology that I could not mention personally one by one.

Publications

Parts of this thesis were already published or were presented at conferences:

Peer-reviewed journals:

(i) V. R. Ikkurthi, K. Matyash, A. Melzer and R. Schneider, "Charge and ion drag on multi static spherical dust grains immersed in rf discharges", to be submitted to Phys. Plasmas. (2009)

(ii) V. R. Ikkurthi, K. Matyash, A. Melzer and R. Schneider, "Computation of ion drag force on a static spherical dust grain immersed in rf discharges", Phys. Plasmas **16**, 043703 (2009)

(iii) V. R. Ikkurthi, K. Matyash, J. Meichsner, A. Melzer and R. Schneider, "Simulation of ion energy distributions in Ar/CH4 rf discharges with ion extraction", Plasma Sources Sci. Technol. **18**, 035003 (2009)

(iv) V. R. Ikkurthi, K. Matyash, A. Melzer and R. Schneider, "Computation of dust charge and potential on a static spherical dust grain immersed in rf discharges", Phys. Plasmas **15**, 123704 (2008)

(v) K. Matyash, R. Schneider, V. R. Ikkurthi and A. Melzer, "Ion drag force on dust grains in the magnetized edge plasma", Journal of Nuclear Materials **390-391**, 103-105 (2009)

(vi) R. Wiese, V. Sushkov, H. Kersten, V. R. Ikkurthi, R. Schneider and R. Hippler, "Behavior of powder particles in a radiofrequency plasma under pulsed argon ion beam bombardment", submitted to Phys. Rev. E (2009)

Contributions to international conferences:

(i) V.R. Ikkurthi, K. Matyash, A. Melzer and R. Schneider, "Charge and ion drag on two static spherical dust grains immersed in rf discharges", Second workshop on Diagnostics and Simulation of Dusty Plasmas, Kiel (Germany) 2-4 September 2009.

(ii) V. R. Ikkurthi, K. Matyash, A. Melzer and R. Schneider, "Study of effect of grain size on dust charging in an RF plasma using three-dimensional PIC-MCC simulations", International Conference on Research and Applications of Plasmas, Greifswald, Germany, 16 - 19 October 2007. AIP Conf. Proc. Vol. 993, pp. 83-86 (2008), ISBN: 978-0-7354-0512-7.

(iii) V.R. Ikkurthi, K. Matyash, A. Melzer and R. Schneider, "Computation of Ion Drag Force and Charge on a Static Spherical Dust Grain in RF Plasma", Fifth International Conference on the Physics of Dusty Plasmas, Ponta Degada (Azores, Portugal) 18-23 May 2008. AIP Conf. Proc. Vol. 1041, (October 2008). ISBN: 978-0-7354-0569-1.

(iv) V. R. Ikkurthi, K. Matyash, A. Melzer and R. Schneider, "Computation of ion drag force on a static spherical dust grain in an RF plasma", DPG Fruhjahrstagung (Spring Meeting), Darmstadt, 10-14 Marz 2008. Verhandl. DPG (VI) 43 3/P 8.6 (2008)

(v) V. R. Ikkurthi, K. Matyash, J. Meichsner, A. Melzer and R. Schneider, "Particle-in-Cell Simulation of RF discharges in Ar/CH4 Gas Mixture", DPG Fruhjahrstagung, Darmstadt, 10-14 Marz 2008. Verhandl. DPG (VI) 43 3/P IV.20 (2008)

(vi) K. Matyash, V. R. Ikkurthi, A. Melzer and R. Schneider, "Effect of grain size on dust charging in an RF plasma", Proc. 34th EPS Conference on Plasma Phys., Warsaw, 2 - 6 July 2007 ECA Vol.31F, P-5.042 (2007)

Eidesstattliche Erklärung

Hiermit erkläre ich, dass diese Arbeit bisher von mir weder an der Mathematisch-Naturwissenschaftlichen Fakultät der Ernst-Moritz-Arndt-Universität Greifswald noch einer anderen wissenschaftlichen Einrichtung zum Zwecke der Promotion eingereicht wurde.

Ferner erkläre ich, daß ich diese Arbeit selbständig verfasst und keine anderen als die darin angegebenen Hilfsmittel benutzt habe.

Greifswald, 26.10.2009

Venkata Ramana Ikkurthi

Curriculum Vitae

Venkata Ramana Ikkurthi

Nationality	:	Indian (Indisch)
Date of Birth	:	1st August, 1976
Place of Birth	:	Chilakaluripet, Andhra Pradesh, India
Marital status	:	Married
Address	:	Bahnhofstr. 2/3, 17489 Greifswald, Germany
Email	:	ramana@physik.uni-greifswald.de, ramana468@gmail.com

Education:

1986-1991 Secondary education at R.V.S.C.V.S. High School, Chilakaluripet, India

1991-1993 Intermediate (12th) at S.C.V.S. Junior College, Chilakaluripet, India

1993-1996 B.Sc. at C.R. College (Nagarjuna University), Ganapavaram, India

1996-1998 M.Sc. (Physics) at University of Hyderabad, India

Work Profile:

1998-1999 Technical Trainee, Institute for Plasma Research, Gandhinagar, India

1999-2006 Scientist, Institute for Plasma Research, Gandhinagar, India

2007-2009 Ph.D., Institut für Physik, Ernst-Moritz-Arndt Universität Greifswald, Greifswald, Germany